Innovative Coexistence: Design and Analysis of Underlay Signaling in 5G New Radio

Kumar Sai Bondada

Thesis submitted to the Faculty of the

Virginia Polytechnic Institute and State University

in partial fulfillment of the requirements for the degree of

Masters of Science

in

Electrical Engineering

Jeffrey Reed, Co-chair

Daniel Jakubisin, Co-chair

Nishith Tripathi

Harpreet Dhillon

September 11, 2023

Blacksburg, Virginia

Keywords: Underlay Signalling, Orthogonal Frequency Division Multiplexing (OFDM), 5G New Radio, Spreading, srsRAN Project

Innovative Coexistence: Design and Analysis of Underlay Signaling in 5G New Radio

Kumar Sai Bondada

(ABSTRACT)

Underlay signaling is a robust physical layer technique, allowing for transmitting a very low power signal in conjunction with the primary signals across the entire frequency band of the primary signals. The secondary users of the secondary network (i.e., a wireless network consisting of primary and secondary networks) primarily utilize the underlay, which increases spectral efficiency and improves the network capacity. This thesis focuses on underlay signaling in the context of the cellular (primary) network, where the underlay is an auxiliary channel made available to the primary users and the network, that is, the base stations and users of the cellular network. The current fifth-generation (5G) cellular networks are constructed using Orthogonal Frequency Division Multiplexing (OFDM) modulation. Hence, this thesis delves into the study of underlay coexistence with OFDM, specifically 5G, by performing extensive simulations and analytical analysis and investigating the impact of underlay signaling on the throughput performance of 5G networks. We develop the underlay signaling based on the frequency-domain spread spectrum and add the underlay signal prior to the Inverse Fast Fourier Transform (IFFT) operation of OFDM. Furthermore, we present a real 5G setup built on the srsRAN project, where we showcase a proof-of-concept demonstration of underlay coexistence with the 5G over the air, where the 5G base station transmits both 5G NR and underlay signal simultaneously. Through our research, we conclusively demonstrate that a low-data rate underlay signal can be successfully transmitted alongside the existing 5G signal. Our study concludes by carefully selecting the appropriate design

parameters, such as the signal-to-interference power level (5G power in relation to underlay), spreading factor, and coding gain at which we can reliably detect and decode underlay signals having no impact on the 5G performance. The integration of underlay in 5G brings forth a multitude of benefits using underlay for military and tactical applications, massive Machine Type Communications (mMTC) alongside Ultra-Reliable Low Latency Communications (URLLC), and the offloading of crucial control information of 5G to the underlay channel. Thus, this underlay operates as a low-data rate error-free conduit, with the potential to provide Low Probability of Interception (LPI) and Low Probability of Detection (LPD) attributes and heightened reliability while concurrently transmitting with the 5G NR, bolstering the overall effectiveness of the communication.

Innovative Coexistence: Design and Analysis of Underlay Signaling in 5G New Radio

Kumar Sai Bondada

(GENERAL AUDIENCE ABSTRACT)

Underlay signaling is a technique that allows for transmitting a low-power signal alongside the primary signals, occupying the entire frequency band of the primary signals. The secondary users of the secondary network (i.e., a wireless network consisting of primary and secondary networks) primarily utilize the underlay, which increases spectral efficiency and improves the network capacity. This thesis focuses on underlay signaling in the context of cellular (primary) networks where the underlay is an auxiliary channel made available to the primary users and network, that is, the base stations and users of the cellular network. The current fifth-generation (5G) cellular networks are constructed using Orthogonal Frequency Division Multiplexing (OFDM) modulation. OFDM is a multicarrier modulation scheme that divides the available frequency band into multiple narrow subcarriers, each carrying a portion of the data. The key advantage of OFDM is its ability to combat frequency-selective fading, where different frequencies experience different levels of fading and interference. By using many closely spaced sub-carriers, OFDM can effectively mitigate the impact of fading, allowing for robust and reliable communication even in challenging channel conditions. Thus, this thesis investigates the co-existence of underlay signaling and OFDM in 5G. We develop the underlay signaling based on the frequency-domain spread spectrum. Extensive simulations and analytical analysis are performed to understand the impact of underlay signaling on OFDM performance in terms of bit error rates and throughput. Additionally, a real 5G setup is presented, demonstrating a proof-of-concept of underlay co-existence with 5G

NR, where the 5G base station transmits both 5G NR and underlay signal simultaneously. Through the research, it is conclusively demonstrated that a low-data rate error-free underlay signal can be successfully transmitted alongside the existing 5G signal. The integration of underlay in 5G brings forth a multitude of benefits using underlay for military and tactical applications, massive Machine Type Communications (mMTC) alongside Ultra-Reliable Low Latency Communications (URLLC), and the offloading of crucial control information of 5G to the underlay channel. Thus, this underlay operates as a low-data rate error-free conduit, characterized by its low interception and low detection attributes, enhancing reliability while concurrently transmitting with 5G NR, bolstering the overall effectiveness of the communication.

Dedication

To my family and friends.

Acknowledgments

I want to express my sincere gratitude to all those who have contributed to the completion of this thesis. Their support, guidance, and encouragement have been invaluable throughout this journey. First and foremost, I am deeply thankful to my advisors, Dr. Jeffrey Reed, Dr. Daniel Jakubisin, and Dr. Nishith Tripathi, for their unwavering guidance and expertise. Their insightful feedback, patience, and dedication played a pivotal role in shaping this research and improving its quality. I am truly grateful for their mentorship and the valuable lessons I have learned under their guidance. I also extend my appreciation to the members of my thesis committee for their valuable insights and constructive suggestions, which significantly contributed to the refinement of this thesis. A special note of gratitude goes to our project sponsor, LMCO (Lockheed Martin Corporation), whose generous funding made this research possible. Their belief in the importance of this work and their financial support were fundamental to its success. Additionally, I would like to acknowledge Dr. Raghunandan Rao for his initial help in understanding the project even before its formal commencement. His early guidance and insights laid a strong foundation for this research. Furthermore, I acknowledge the support and assistance provided by the staff and faculty of Virginia Tech. Their willingness to provide resources, access to research materials, and technical support was instrumental in the successful completion of this work. My family and friends deserve my deep gratitude for their unwavering encouragement and understanding throughout this demanding process, serving as a source of motivation during challenging times. Finally, I express heartfelt appreciation to all the participants who generously dedicated their time and contributed their insights to this study, instrumental in generating meaningful results. In conclusion, I acknowledge all those who have directly or indirectly contributed to this

thesis. Your support and encouragement have been invaluable, and I am truly grateful for your assistance on this academic journey.

Contents

List of Figures

List of Tables

Chapter 1

Introduction

Underlay signaling is a robust physical layer technique that involves transmitting a secondary signal simultaneously with the primary signal of interest, with minimal or no impact on the primary signal's quality. The underlay signal is generally transmitted at a very low power level, well below the noise floor, and occupies the entire frequency band of the primary signal. This allows the primary signal to interpret the underlay signal as random noise with very low power. Conversely, the underlay signal perceives the primary signal as high-power interference. Underlay signaling has been significantly explored in the realm of spectrum sharing to improve the spectrum efficiency of wireless networks. Secondary users (of the secondary network) [1, 2, 3, 4] and device-to-device (D2D) communications [5, 6, 7, 8, 9, 10] employed underlay to transmit data concurrently by sharing the frequency bands with primary users without causing interference.

However, our research takes a distinctive path from prior underlay studies, which primarily revolve around secondary users deploying underlay within the network. In our innovative approach, primary users, especially 5G base stations and users themselves serve as the carriers of the underlay signal, transmitting it alongside its actual primary signal.

In this thesis, we explore the use of underlay signaling as a secure auxiliary channel for the 5G New Radio interface, targeting primary users of the primary network. The proposed auxiliary channel facilitates the concurrent transmission of data using the 5G infrastructure without disrupting its functionality and transmits alongside the 5G transmission. The

auxiliary channel, built on underlay signaling, allows us to transmit low-data-rate error-free information simultaneously with the 5G signal, occupying the entire 5G band. The design of the underlay signal is based on the frequency domain spread spectrum, which provides the necessary Signal-to-Interference-plus-Noise Ratio (SINR) gain to mitigate the full-band interference emanating from 5G. Notably, this approach also bestows potential Low Probability of Intercept/Low Probability of Detection (LPI/LPD) characteristics and anti-jamming capabilities due to the spreading operation involved, thereby increasing the network's resiliency. Furthermore, our underlay incorporates features of a non-preemptive nature, i.e., it won't preempt the ongoing 5G transmission, providing low-latency communication.

In essence, our research pioneers the integration of underlay signaling as an indispensable component of the 5G ecosystem, empowering primary users with a secure and efficient means of concurrent data transmission while preserving the integrity of the primary network's operation.

1.1 Background and Context

5G, the fifth-generation technology standard, represents the next evolutionary step from 4G. It is currently experiencing remarkable growth and is positioned to surpass 4G connections by 2029, as indicated by its status as the fastest-growing mobile network [11]. By 2028, it is projected to achieve an impressive 85% coverage. This advanced network technology brings forth a multitude of benefits, including faster speeds, reduced latency, expanded capacity, and heightened reliability. Consequently, it unlocks countless possibilities for diverse applications and opens doors to new use cases. Ultimately, 5G is set to become an integral part of our lives, seamlessly connecting us to everything around us.

The 5G system comprises the radio access network (RAN) and the core network (CN).

The RAN connects the user equipment (UE) to the core network. It is responsible for transmitting and receiving radio signals between UEs and the Base station (BS). The core network connects the RAN to the rest of the internet. Within the 5G RAN, New Radio (NR) is the next generation (5th) wireless radio access technology (RAT), standardized by the 3rd Generation Partnership Project (3GPP), which enables a wide range of applications with three main use cases, i.e., Enhanced Mobile Broadband (eMBB), Massive Machine-Type Communication (mMTC) and Ultra-Reliable Low-Latency Communication (URLLC). It is the key component of the 5G system and provides enhanced performance, capacity and flexibility compared to previous generations. The 5G RAN stack consists of several layers that work together to enable wireless communication between user devices and the core network. Here are the key components of the 5G RAN stack:

- Physical Layer (PHY): The PHY layer is responsible for transmitting and receiving radio signals over air. It handles tasks such as modulation, coding, and channel estimation.

- Medium Access Control (MAC) Layer: The MAC layer controls access to the radio resources and manages data transmission scheduling. It ensures efficient utilization of the available radio spectrum.

- Radio Link Control (RLC) Layer: The RLC layer provides reliable and error-free data transmission between the UE and the BS. It handles the segmentation and reassembly of data packets and provides mechanisms for error detection and recovery.

- Packet Data Convergence Protocol (PDCP) Layer: The PDCP layer is responsible for the compression and decompression of IP packets. It provides header compression and encryption functions to optimize the transmission of IP-based data.

- Radio Resource Control (RRC) Layer: The RRC layer manages the control signaling between the UE and the base station. It handles functions such as connection establishment, handover, and power control.

From the 5G physical layer perspective, the users' data is meticulously scheduled over time-frequency resources that are orthogonal, employing slot-level scheduling. The slot is defined as a block of time-frequency resources, where each individual time-frequency resource is called the Resource element (RE). Beyond user data, there exist control data that plays a crucial role in revealing the allocation of user data on these REs, along with critical information like HARQ (Hybrid Automatic Repeat Request), Channel State Information feedback, redundancy versions of users' data, and more. The 5G standards have developed channels such as control channels for control information exchange and data channels for users' information exchange, listed in Table. 1.1. Apart from this, there are reference signals in 5G in assisting the physical layer in synchronization aspects, channel estimation, tracking and beam identification for beamforming. The main purpose of control channels and reference signals is to improve the 5G radio interface's robustness by carrying vital information that facilitates and establishes user data exchange. Not only at the physical layer, the control signaling information exchange exists at each layer of the 5G RAN stack increasing the control overhead of the 5G system. Further, since the 5G opens up new use cases, the control messaging exchange differs depending upon use case requirements.

1.2 Motivation

The spectrum remains a limited resource in the current cellular bands. Also, there is a need for efficient data scheduling with low latency. Thus, developing a parallel channel in conjunction with the 5G transmission operating in the same band, through which the

Table 1.1: 5G Control Channels and Data Channels

Control Channels	Data Channels
Physical Downlink Control Channel (PDCCH): Carries downlink control information (DCI) from gNodeB to UEs. DCI provides resource allocation and scheduling instructions such as modulation and coding scheme (MCS) and hybrid-ARQ information.	**Physical Downlink Shared Channel (PDSCH)**: Delivers downlink user data, UE-specific higher-layer control messages, system information blocks, and paging.
Physical Uplink Control Channel (PUCCH): Transmits uplink control information (UCI) from UEs to gNodeB. Carries feedback, acknowledgments, and channel quality reports.	**Physical Uplink Shared Channel (PUSCH)**: Carries uplink user data and higher-layer control messages.
Physical Broadcast Channel (PBCH): It is a part of the Secondary synchronization block, broadcasting master information block (MIB) to all UEs in the cell.	
Physical Random Access Channel (PRACH): Used by UEs for channel initial access and uplink synchronization.	

control data and other vital information can be offloaded from existing 5G primary channels to this parallel alternative, can be helpful. This approach optimizes utilizing scarce spectrum resources concurrently transmitting with 5G while maintaining low latency, which is critical in delivering a seamless and robust user experience.

Further, the control channels of both 4G and 5G networks are more susceptible to jamming attacks and are also vulnerable to spoofing and sniffing compared to the data channels, as highlighted in research papers [12, 13]. These studies delve into the weaknesses of the data channels, control channels, and reference signals in the presence of adversarial activities such as jamming, spoofing, and sniffing. The findings underscore that the PSS/SSS and PBCH channels are particularly susceptible and likely to be targeted first among these channels. It becomes increasingly effective and easier for an adversary to spoof fake PSS/SSS signals and manipulate MIB/SIB contents through PBCH by broadcasting an SS block. Given that

this is the first message the UE decodes prior association with the cell, and considering the lack of prior authentication to differentiate between genuine and counterfeit SS blocks, the risk is substantial. Addressing these vulnerabilities is of paramount importance. In light of these challenges, the underlay signaling will be a compelling avenue for enhancing the security landscape. By amalgamating the traits of Low Probability of Intercept/Low Probability of Detection (LPI/LPD) and anti-jamming capabilities, underlay signaling holds great promise as a solution for transmitting crucial control information within 5G cellular networks, ultimately bolstering the network's overall resiliency.

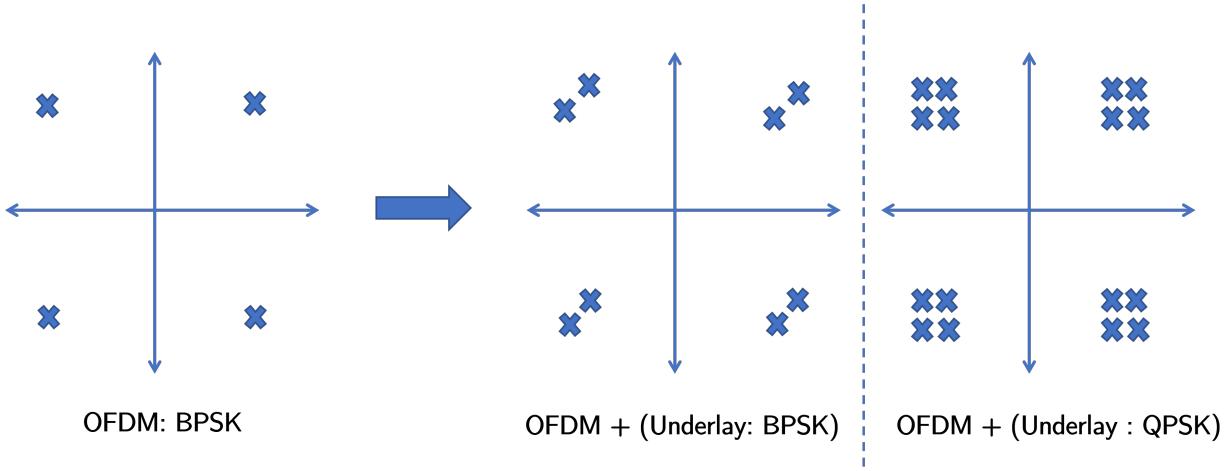

Figure 1.1: Constellation Plots of 5G OFDM with QPSK modulation scheme with Underlay added using different modulation schemes at the Transmitter

Notably, the advent of 5G has also attracted significant attention in the realm of defense and military communications. The United States Department of Defense (DoD) has even outlined a comprehensive 5G strategy [14], underlining the strategic importance of this technology in those domains. While 5G holds immense potential for enhancing various applications within the DoD, it is not immune to disruption. Augmentation to 5G can improve its resilience or covertness in key ways. One such avenue can be the integration of underlay with the 5G, bolstering its resilience and covert capabilities. Fig. 1.1 illustrates the constellation plots of two scenarios: 5G superimposed without and with an underlay within

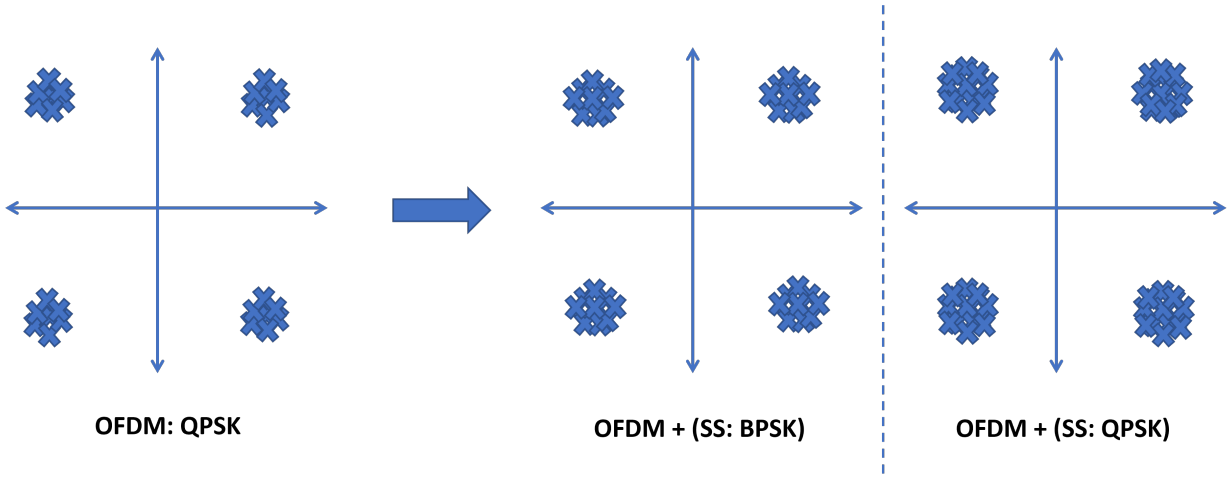

Figure 1.2: Constellation Plots of 5G OFDM with QPSK modulation scheme with Underlay added using different modulation schemes at the Receiver

it. In the case of 5G, QPSK modulation is assumed, while the underlay adopts various modulation schemes such as BPSK and QPSK. By introducing an underlay symbol with extremely low power, the 5G modulation symbol incorporates the underlay and exhibits different translations in distinct directions, influenced by the underlay's phases. The degree of translation directly corresponds to the power of the underlay signal. Conversely, Fig. 1.2 portrays the constellation of the received equalized symbols. However, due to the presence of noise (AWGN), the underlay embedded within the 5G signal becomes indiscernible. This situation can also be examined from the perspective of the frequency domain. Fig. 1.3 shows the Power Spectral Density (PSD) comparison of three signals: 5G OFDM with power 0 dBW/Hz, Underlay signal with power -20 dBW/Hz, and AWGN with power -15 dBW/Hz. The underlay operates at 5 dBW/Hz below that of the AWGN channel, which makes it difficult to detect. Thus, the proposed approach can be useful in both commercial and military communications domains (e.g., industrial and tactical IoT) and can enable seamless integration of tactical communications within 5G network architectures.

The proposed approach will benefit 5G Ultra-Reliable Low-Latency Communications (URLLC),

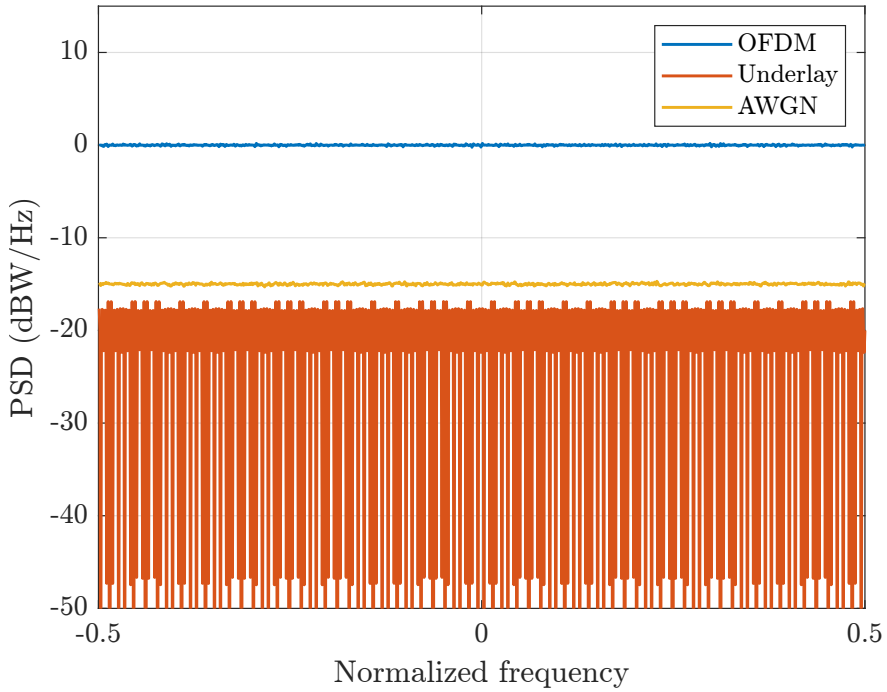

Figure 1.3: Power Spectral Density (PSD) comparison of three signals: OFDM with power 0 dBW/Hz, Underlay signal with power -20 dBW/Hz, and Additive White Gaussian Noise (AWGN) with -15 dBW/Hz.

catering to the requirements of time-sensitive applications. The 3GPP Technical Specification (TS) 38.912 [15] describes two types of scheduling, i.e., pre-emptive and non-pre-emptive scheduling for URLLC. In pre-emptive scheduling, the eMBB traffic scheduled over available radio resources within a TTI is punctured by URLLC data, meeting the delay criteria but leading to performance degradation of eMBB traffic, resulting in re-scheduling and multiple HARQ re-transmissions. In non-preemptive scheduling, the URLLC data is scheduled along with eMBB data after the completion of ongoing traffic, which may fail to meet the strict delay constraints for URLLC traffic. Our approach seeks to evade these issues by transmitting the URLLC data using the proposed frequency-domain spreading underlay signal transmitting concurrently to ongoing eMBB traffic without preemption and avoiding delays seen in non-preemptive scheduling. The proposed approach is an enhancement over URLLC for low latency-critical data-rate applications. In addition to the latency benefits, the un-

derlay signal provides increased resiliency and potential LPI/LPD characteristics due to the utilization of frequency-domain spreading.

1.3 Literature Review

Underlay signaling has been extensively studied in various domains, including cognitive radio technology, Device-to-Device (D2D) communications, and uplink scheduling requests in 5G networks. In the context of LTE-advanced and 5G networks, underlay D2D communications [5, 6, 7, 8, 9, 10] were proposed to operate in licensed bands, aiming to improve spectrum efficiency and increase the overall throughput of the network. Research in this area has explored mechanisms for interference management, session setup and management, feasibility analysis, and functional blocks to enable D2D communications using underlay signaling. Significant attention has been given to energy-efficient resource allocations for D2D users, with these problems formulated as optimization tasks [16, 17, 18, 19, 20] such as mixed integer nonlinear programming (MINIP), gradient-aided dual decomposition, and Combinatorial approaches [21, 22]. Underlay signaling has also been studied in the context of National Security and Public Safety communications [23] and Disaster relief communications [24].

Underlay is one of the techniques used by cognitive radios for its transmission concurrent to non-cognitive users. The study also included the use of relay networks through which underlay transmission is done, and its power level is kept low, meeting the interference constraint. The information-theoretic perspective of cognitive radio with underlay mode is studied by Goldsmith *et al.* [1]. Furthermore, researchers have analyzed the outage probability of cognitive radio networks incorporating underlay and relay selection criteria [2, 3]. In addition, a proposal for combining Non-Orthogonal Multiple Access (NOMA) with underlay in cognitive radio relay networks has been investigated, with particular attention

given to open challenges and outage probability [4].

Underlay signaling in recent years was explored in transmitting uplink scheduling requests for 5G networks [25, 26]. Aminjavaheri *et al.* [26] proposed using underlay for users to send their scheduling requests to the Base station (BS) to reduce the signaling overhead for URLLC. The underlay was developed using Zadoff-Chu sequences.

Overall, extensive research on underlay signaling across various domains highlights its potential to enhance spectrum efficiency and network throughput by targeting secondary users in secondary networks. Our research focus is on designing an auxiliary channel for 5G based on underlay signaling, targeting the primary users of the primary network and increasing its resiliency. Furthermore, research on underlay signaling has been focused on power allocation and resource sharing, formulating the research problem as an optimization problem. Our focus is on waveform design and analyzing performance in terms of error rates and throughput.

1.4 Methodology

Our method of adding the underlay signal to 5G is based on superposition coding, and we add the underlay prior to the 5G OFDM IFFT (Inverse Fast Fourier Transform) block. This addition seems to align with the Power Domain Non-Orthogonal Multiple Access (PD-NOMA); however, the underlay in 5G-underlay coexistence is always allocated to minimal power to have zero to minimal impact on 5G traffic. In contrast, in the PD-NOMA, the user with worse channel conditions is allocated higher power, and the user with good channel conditions is allocated lower power. Thus, the underlay transmission power is limited by the interference caused to the 5G signal. A trade-off exists between the transmitted power level of underlay and de-spreading gain. The de-spreading at the underlay receiver should

account for substantial full-band interference from the 5G signal and loss of power due to the communication channel. We explore these trade-offs in our research and provide a potential solution to design the Underlay 5G-OFDM waveform.

1.5 Contribution

Our contribution encompasses the development and validation of an underlay-5G OFDM waveform. In this innovative approach, the underlay is constructed using the frequency domain spread spectrum technique, strategically occupying the entire bandwidth of the 5G OFDM signal. This underlay serves as a pivotal auxiliary channel within the 5G NR signal, and it can be flexibly transmitted by either base stations or users within the 5G network. To substantiate the viability of our underlay-5G OFDM waveform, we executed extensive simulations aimed at demonstrating the seamless coexistence of the underlay and OFDM signals. Complementing these simulations, we conducted comprehensive analytical analyses, yielding Bit Error Rate (BER) expressions that encapsulate the performance characteristics of the combined underlay-OFDM system. Furthermore, we delved into evaluating the underlay signal's impact on the 5G Physical Downlink Shared Channel (PDSCH) throughput performance, shedding light on its potential benefits for real-world applications. Lastly, to provide tangible proof of concept, we employed the 5G srsRAN software, showcasing the successful coexistence between our underlay signal and the standard 5G waveform, where the underlay is transmitted along with the 5G NR signal.

The outcome of this thesis has resulted in the publishing of three research papers titled

1. Enhanced Non-preemptive Support of URLLC using Spread Spectrum Underlay Signalling. The paper is accepted for Publication at IEEE MILCOM 2023.

2. Demonstration of 5G-Underlay Signal Co-existence. The demo paper is accepted for Publication at IEEE MILCOM Demonstration 2023.

3. Bit Error Rate Analysis for 5G NR Architecture Augmented by a Spread Spectrum Underlay. The paper is in drafting.

Underlay, as an auxiliary channel to the 5G NR signal, offers numerous potential benefits to 5G. The underlay, constructed on the basis of frequency-domain spread spectrum technology, provides it with Low Probability of Intercept (LPI) and Low Probability of Detection (LPD) characteristics. This means that the data transmitted on underlay is more difficult to detect and decode than ever, thereby enhancing the security and making it ideal for sensitive applications. The non-preemptive nature of the underlay ensures that critical information is always transmitted without interruption. Whether it's crucial control data or low-data rate Ultra-Reliable Low Latency Communication (URLLC), the underlay guarantees reliability. The underlay's low data rate capabilities make it perfect for secure Internet of Things (IoT) applications. It's not just about connecting devices, it's also about doing so with the utmost security and resiliency. The underlay isn't just confined to civilian use cases. Its features make it a perfect fit for tactical IoT and military communications. With minimal adjustments, it seamlessly integrates these critical functions onto the 5G network. Importantly, the underlay added on top of OFDM in 5G doesn't affect the Peak-to-Average Power Ratio (PAPR) of the transceiver, ensuring the stability and resiliency of 5G communications.

1.6 Organisation of Thesis

Chapter 2 deals with the architectural design of the underlay signal generation and its addition to the OFDM, as well as the underlay and OFDM signals recovery at the receiver.

The chapter also examines the bit error rate (BER) performance of OFDM modulation with digital modulation schemes employed in 5G standards when underlay is added. Furthermore, it also explores the BER performance of underlay with different codes based on their auto-correlation and cross-correlation properties. The channel considered here for the simulations is the Additive White Gaussian Noise (AWGN) channel. The evaluation of the Peak-to-Average Power Ratio (PAPR) analysis is also carried out for the proposed architecture.

Chapter 3 presents the analytical analysis of the proposed architecture. We derived the BER performance of OFDM added with underlay and compared it with the simulated and derived BER performance. Additionally, the BER performance of underlay is derived and compared with the simulated results.

Chapter 4 studies the impact of underlay on 5G signal, specifically the Physical Downlink Shared Channel (PDSCH). We analyzed the performance of 5G PDSCH in terms of throughput and block error rate (BLER). The underlay design is enhanced with Polar coding, and we investigated the performance improvement from the coding and spreading. The simulations are conducted using the clustered delay line (CDL) channel model [27], which represents a realistic channel model that simulates real-world radio channels.

Chapter 5 explains the implementation of underlay in the 5G srsRAN system, a real-time 5G setup implemented in software. An image is transmitted through the underlay signal concurrently transmitting with 5G data transmission. We used two links between gNodeB and UE, i.e., a zeroMQ link to test and evaluate the functionality of underlay in controlled channel environments and an over-the-air link using software-defined radios to demonstrate the underlay-5G coexistence.

Chapter 6 studies the cancellation of underlay to improve the performance of 5G-OFDM signal. The decoded underlay bits are encoded back into spread underlay symbols, and these

are subtracted from the underlay-5G signal to remove underlay.

Finally, the conclusion and future work are discussed in Chapter 7.

Chapter 2

Underlay Signalling Design and Addition to 5G OFDM System

The chapter examines the design of underlay signal generation and its superposition onto the OFDM chain at the transmitter, as well as underlay signal recovery at the receiver. Furthermore, we develop a link-level simulator for the proposed approach and analyze the bit error rate (BER) performance of underlay and OFDM in the AWGN channel. The underlay can be constructed using different spreading codes with different lengths, so we investigate its performance with various codes and different lengths. Given that the Peak-to-Average Power Ratio (PAPR) is a critical issue that drives the power amplifier into the non-linear region in the OFDM transceivers, we also study this problem in the context of underlay and OFDM coexistence.

2.1 Underlay Transmitter and Signal Construction

The block of underlay bits $K \times x$ (x is the number of bits per each underlay symbol) are digitally modulated and serial-to-parallel converted. Each modulated symbol U^k ($k \in 1, 2, ..., K$) is spread by spreading sequence c_l ($l \in 1, 2, ..., L$) of length L at the underlay transmitter as shown in Fig. 2.1. The generated spread underlay symbols of length $L \times K$

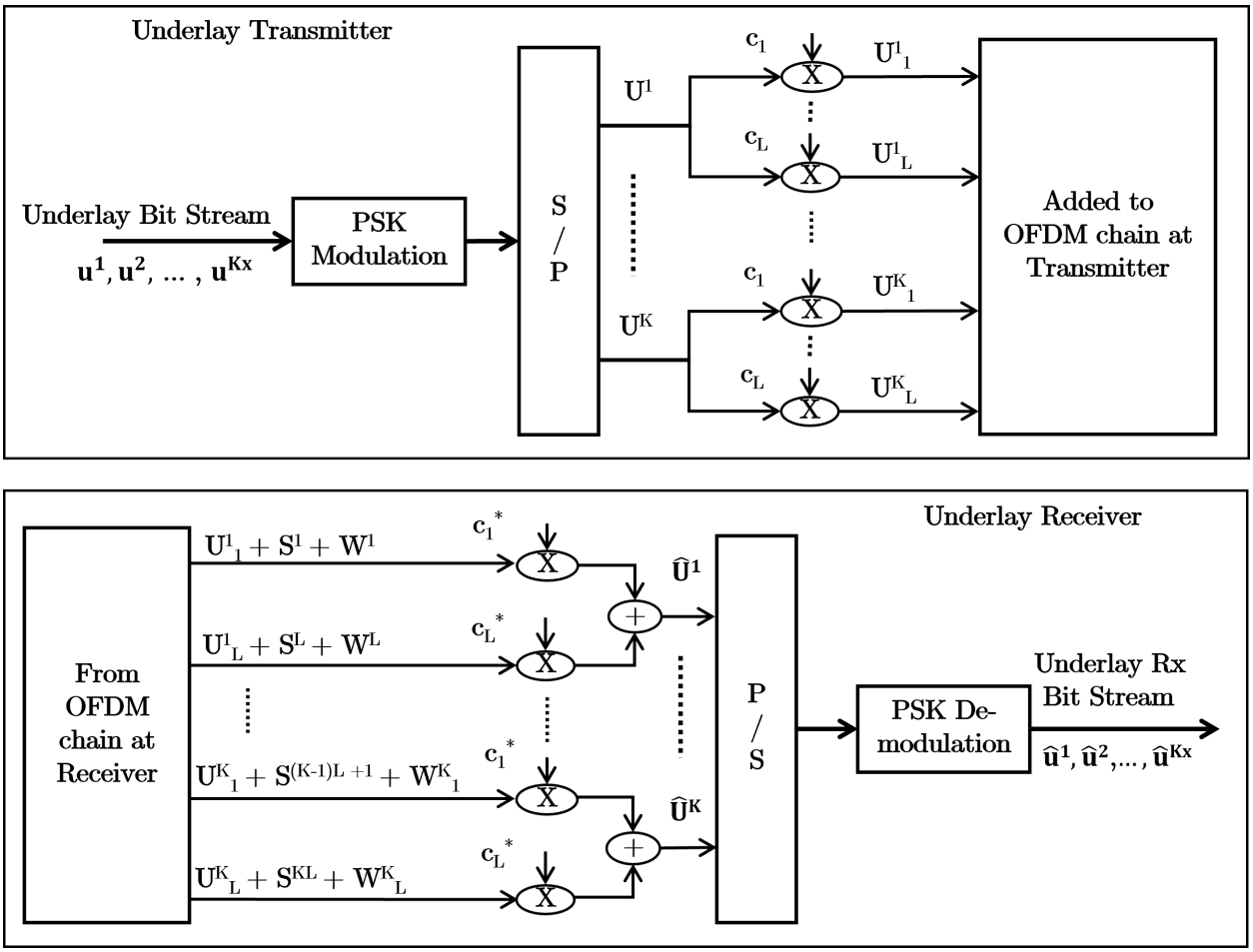

Figure 2.1: Underlay Transceiver Architecture: The Transmitter includes digital modulation, serial-to-parallel conversion, and spreading operation, while the Receiver includes de-spreading, parallel-to-serial conversion, and digital demodulation.

are

$$\rightarrow U_1^1, ..., U_L^1, U_1^2, ..., U_L^2, ..., U_1^K, ..., U_L^K \tag{2.1}$$

Then, the power of generated spread underlay symbols is reduced to the desired level, and symbols are added onto the subcarriers of the OFDM chain of length N. Thus transmitting K symbols (or $K \times x$ bits) of the underlay signal on each OFDM symbol. Adding underlay to any block of the OFDM chain at the transmitter is a linear operation, meaning that

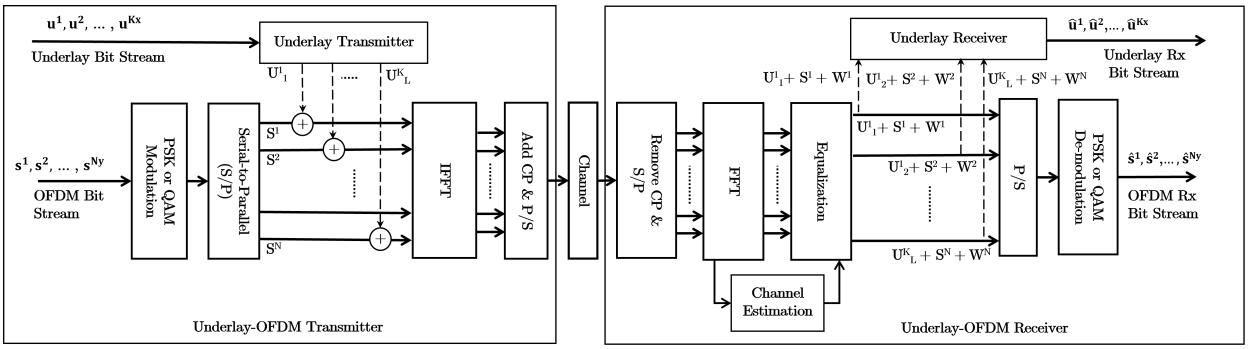

Figure 2.2: Underlay-OFDM Transceiver Architecture: The addition of underlay signal from the Underlay Transmitter to sub-carriers of the OFDM chain at the transmitter, and equalized received symbols containing underlay feeding into the Underlay Receiver at the receiver.

it can be added at any point in the OFDM transmitter chain. However, we chose to add the underlay just before the IFFT block. This enables the detection of the underlay by the underlay receiver after equalization and synchronization to the OFDM symbols (overlay). By doing so, we avoid the need to develop methods for the underlay symbol's synchronization, simplifying the underlay transceiver's design and implementation.

2.2 Underlay-OFDM Transmitter and Signal Construction

A block of $N \times y$ bits (y is the number of bits per each modulated symbol) undergoing OFDM modulation is digitally modulated and serial-to-parallel converted as shown in Fig. 2.2. The spread underlay symbols (2.1) are now added to modulated symbols of the OFDM chain. The transmitted underlay OFDM signal after IFFT (of size N) is given by

$$X^n = \Sigma_{i=1}^{N}(S^i + U_l^k)e^{j2\pi in/N} \tag{2.2}$$

where

$$i = (k-1)L + l, \tag{2.3}$$

S^i is the sequence of digitally modulated symbols in the OFDM chain, and U_l^k is the spread underlay symbol. The signal is then added with a cyclic prefix (CP) and transmitted to the receiver using a wireless communication channel. Here, we assume that the number of spread underlay symbols (2.1) is less than or equal to the number of sub-carriers N (i.e., $N >= K \times L$).

2.3 OFDM Signal Recovery at Underlay-OFDM Receiver

Assuming the AWGN channel, the received signal after removing the CP and performing the FFT operation can be expressed as:

$$Y^i = \Sigma_{n=1}^{N} X^n e^{-j2\pi ni/N} + W^i \tag{2.4}$$

By substituting (2.2) in Y^i, we obtain:

$$Y^i = S^i + U_l^k + W^i \tag{2.5}$$

Dropping the numbering notation from (2.5), we can see the received signal Y as the combination of transmitted spread underlay symbol U, OFDM modulated symbol S, and AWGN with Gaussian distribution, $W \sim \mathcal{CN}(0, \sigma_w^2)$. The variance σ_w^2 also equals the power of AWGN noise. We employ a maximum-likelihood (ML) decoder at the demodulator block of the OFDM chain. It is clear from (2.5) that the performance of the modulated symbols

for the OFDM chain is affected by the power of the spread underlay symbols. We assume P_s, P_u, and $P_w = \sigma_w^2$ to be defined as the power of the OFDM signal, underlay signal, and AWGN noise.

2.4 Underlay Signal Recovery at Underlay-OFDM Receiver

The received signal given by (2.5) is fed into the underlay receiver. The received spread underlay samples $Y_l^k = U_l^k + S^{(k-1)L+l} + W_l^k$ (according to (2.3)) corresponding to each transmitted underlay symbol U^k are despread using the same spreading code that was used at the transmitter. This despreading operation can be expressed as follows:

$$\hat{U}^k = \frac{1}{L}\Sigma_{l=1}^{L} Y_l^k c_l^* = \frac{1}{L}\Sigma_{l=1}^{L}(U_l^k + S^{(k-1)L+l} + W_l^k)c_l^* \tag{2.6}$$

Here, $\hat{U}^k$ represents the despread underlay symbol, Y_l^k is the l-th spread underlay sample of the received signal corresponding to the k-th underlay symbol, and c_l^* is the complex conjugate of the spreading code.

We assume that symbols S are drawn uniformly randomly from modulation symbol set $\mathcal{S}$ belonging to a modulation scheme with average unit energy ($P_s = 1$). According to the central limit theorem, the summation terms S and W in (3.2) result in a new Gaussian random variable $\mathcal{M}$. The variance of $\Sigma_{l=1}^{L} S^{(k-1)L+l} c_l^*$ is L and variance of $\Sigma_{l=1}^{L} W_l^k c_l^*$ is LP_w. The mean and variance of complex noise term plus interference term $\frac{\Sigma_{l=1}^{L} S^{(k-1)L+l} c_l^* + \Sigma_{i=1}^{L} W_l^k c_l^*}{L}$ to the underlay symbol are 0 and $\frac{1+P_w}{L}$ respectively, i.e., $\mathcal{M} \sim \mathcal{CN}(0, \frac{1+P_w}{L})$. The de-spread underlay symbols (3.2) are then decoded at the de-modulator block of the underlay chain to obtain the underlay bits.

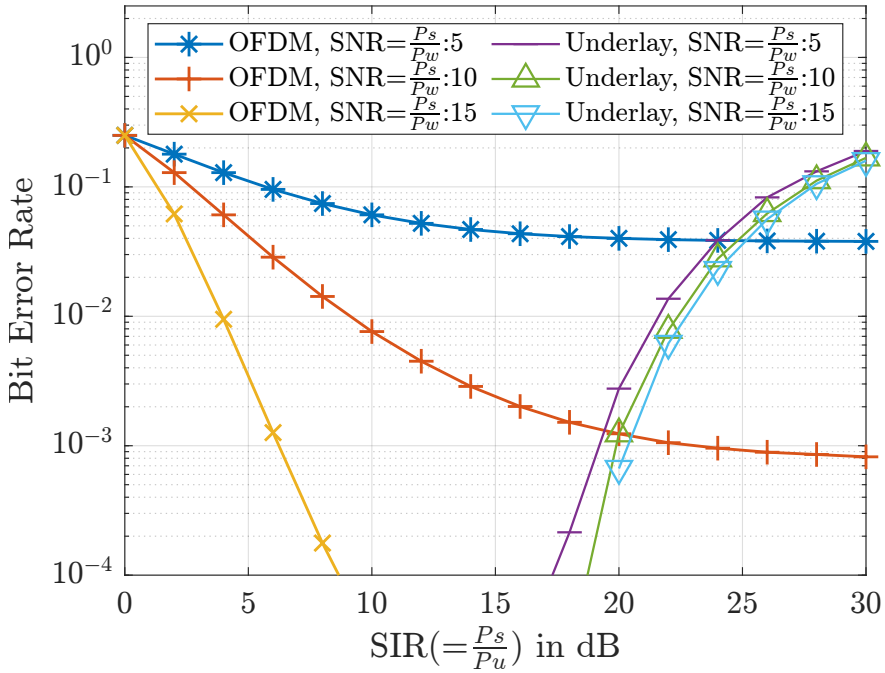

Figure 2.3: OFDM and Underlay Bit Error Rate (BER) performance against Signal-to-Interference Ratio (SIR) = $\frac{P_s}{P_u}$ with different Signal-to-Noise Ratio (SNR) = $\frac{P_s}{P_w}$ values (L = 1024)

2.5 Simulation Results

We consider a Single-Input Single-Output antenna setup and define Signal-to-Noise Ratio (SNR) as the ratio $\frac{P_s}{P_w}$, and Signal-to-Interference Ratio (SIR) as the ratio $\frac{P_s}{P_u}$, both measured in dB. The size of the Fast Fourier Transform (FFT) in the OFDM chain is set equal to the spreading length. Additionally, we assume the number of subcarriers to be equal to the FFT size, with all subcarriers being utilized for OFDM modulation.

In the first analysis, we investigate how the underlay power P_u affects the performance of OFDM and underlay in terms of BER. To visualize this impact, we plot the BER of OFDM and underlay on the Y-axis against the SIR on the X-axis, as shown in Fig. 2.3. Our simulations use the QPSK modulation scheme for OFDM and underlay with a spreading length $L = 1024$. Specifically, we transmit one QPSK underlay symbol ($K = 1$) on each

OFDM symbol (1024 subcarriers). Our results indicate that as the SIR increases (i.e., as P_u decreases), the BER of OFDM improves and eventually converges to the BER of OFDM in an AWGN channel without underlay when SIR is very high. This suggests that using very low underlay power is beneficial for OFDM. However, this also limits the underlay performance, as we observe the BER of underlay starting to increase at high SIR values from 16 dB onward. To achieve a BER of 10^{-4} for both OFDM and underlay, we identify a range of SIRs from 10 to 16 dB for a particular SNR that tends to achieve this performance. Thus, depending on our performance criterion, we can operate in different regions of SIRs.

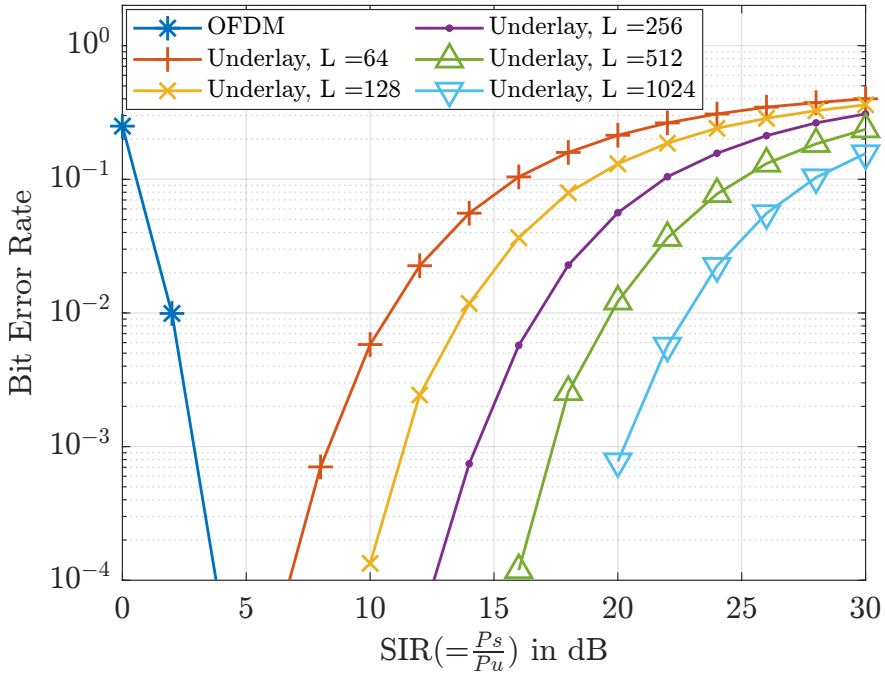

Figure 2.4: OFDM and Underlay BER performance against SIR=$\frac{P_s}{P_u}$ at different spreading lengths at SNR = 20 dB

We now investigate the impact of spreading length L on the valid region of SIR operation at a high SNR value of 20 dB. Fig. 2.4 illustrates the BER of underlay on the Y-axis for different spreading lengths against SIR on the X-axis. As expected, the underlay's performance improves with increasing spreading length. However, this comes at the expense of underlay

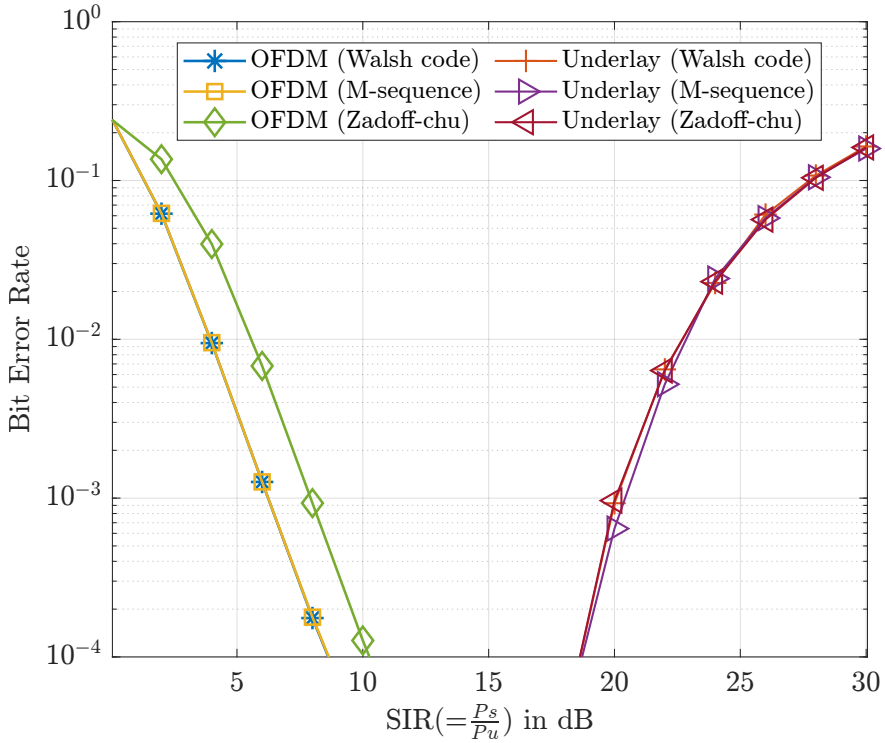

Figure 2.5: Bit Error Rate (BER) performance of OFDM and Underlay with respect to Signal-to-Interference Ratio (SIR) = $\frac{P_s}{P_u}$ at SNR = $\frac{P_s}{P_w}$ = 15 dB for various codes.

throughput. For instance, with $L = 64$, we transmit $K = 16$ underlay symbols, while with $L = 1024$, we transmit only $K = 1$ underlay symbol. This implies that we can use lower spreading lengths if we want to transmit more bits. However, reliable decoding at the receiver requires higher power P_u. It's worth noting that the plot shows that underlay with a low spreading length can be reliably decoded by transmitting at higher power P_u (low SIR regions).

Fig. 2.5 illustrates the BER performance of OFDM and underlay using three different spreading codes: Walsh, M-sequence, and Zadoff-Chu sequence for underlay. See Appendix C for more details on the codes. The spreading lengths used for these codes were 1024, 1023, and 1023, respectively, at a signal-to-noise ratio (SNR) of 15 dB. The underlay performance was observed to be similar across all codes, as each code provided the same spreading gain at the

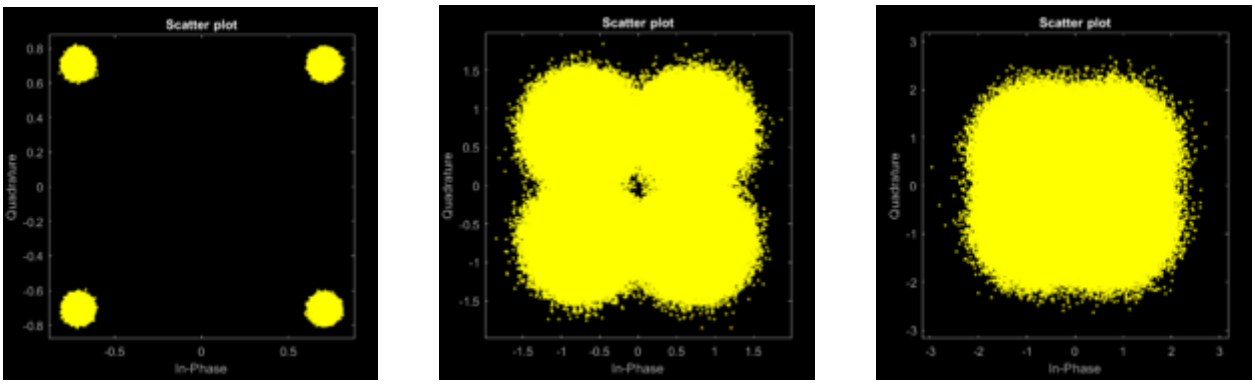

(a) SNR = 30 dB (b) SNR = 10 dB (c) SNR = 5 dB

Figure 2.6: Constellation plots of received QPSK modulation symbols undergone OFDM modulation without underlay at different SNRs and SIR = 15 dB

receiver, effectively combating the full-band OFDM interference. However, the performance of OFDM degraded slightly when using the Zadoff-Chu sequence, as compared to the Walsh and M-sequence, which were similar. The Walsh code and M-sequences have values of +1s and -1s, spreading the underlay symbols. The constellation of spread underlay symbols follows the constellation of underlay symbols, i.e., PSK modulation. The Zadoff-Chu sequences exhibit values around the unit magnitude circle, resulting in the spread underlay symbols aligning on the unit circle. When spread underlay symbols of low power are added to OFDM chain-modulated symbols, each modulated symbol gets translated to conform to the constellation of spread underlay symbols within its decision region. At low SIR scenarios, the interfering spread underlay symbols shift the OFDM modulation symbols into their adjacent decision regions, thus degrading the performance of the OFDM system. For the Zadoff-Chu sequence, the translation of OFDM modulation symbols occurs along the circle, whereas for the M-sequence and Walsh code, the translation is only in two directions. Importantly, the translation is not directly towards the symbol boundaries but at a 45° offset. Consequently, the Zadoff-Chu sequence has performance slightly degraded.

Fig. 2.6, Fig. 2.7, and Fig. 2.8 represent the constellation plots of received QPSK symbols

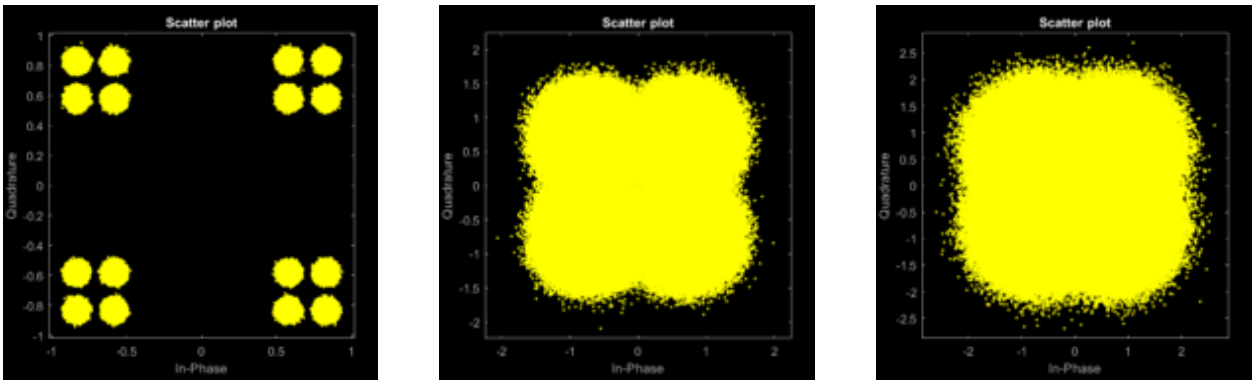

(a) SNR = 30 dB (b) SNR = 10 dB (c) SNR = 5 dB

Figure 2.7: Constellation plots of received QPSK modulation symbols undergone OFDM modulation with underlay using Walsch code at different SNRs and SIR = 15 dB

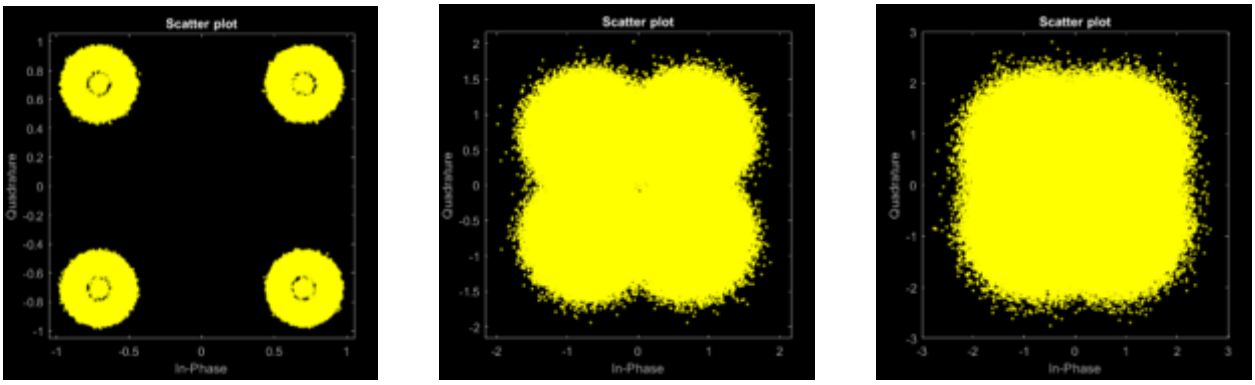

(a) SNR = 30 dB (b) SNR = 10 dB (c) SNR = 5 dB

Figure 2.8: Constellation plots of received QPSK modulation symbols undergone OFDM modulation with underlay using Zadoff-Chu sequence at different SNRs and SIR = 15 dB

undergone through OFDM modulation at different SNRs, with a fixed SIR of 15 dB. Specifically, the spreading codes used in Fig. 2.7 and Fig. 2.8 are the Walsh code and Zadoff-Chu sequence, respectively. Notably, at higher SNR values, such as 30 dB, the translation of QPSK symbols when embedded with QPSK underlay is clearly discernible. However, at lower SNR levels of 5 dB and 10 dB, the QPSK symbols with underlay closely resemble QPSK symbols without underlay.

Fig. 2.9 depicts the BER performance of OFDM with underlay added at various SIRs. The

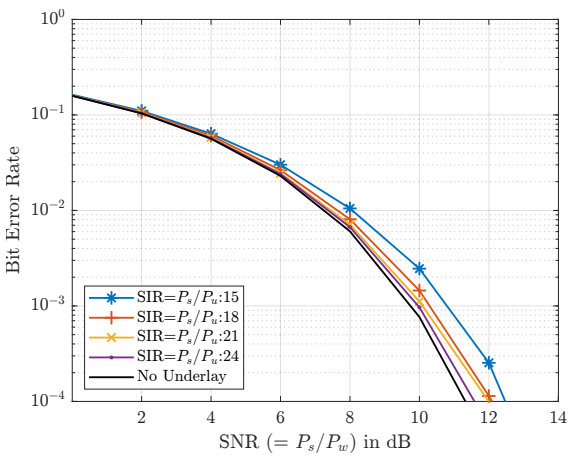

(a) QPSK modulation scheme

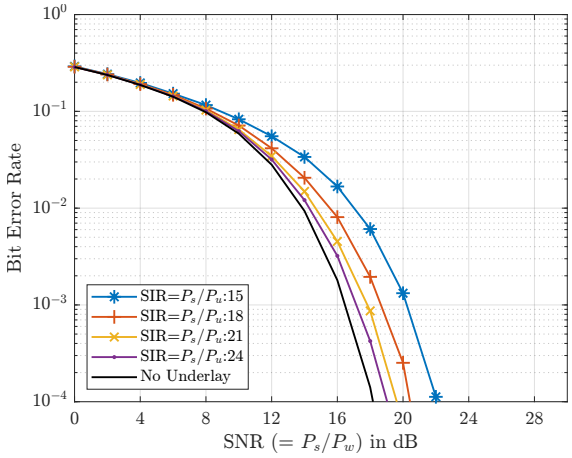

(b) 16-QAM modulation scheme

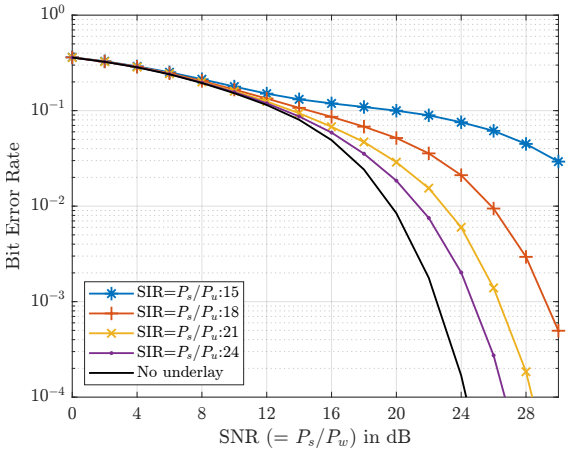

(c) 64-QAM modulation scheme

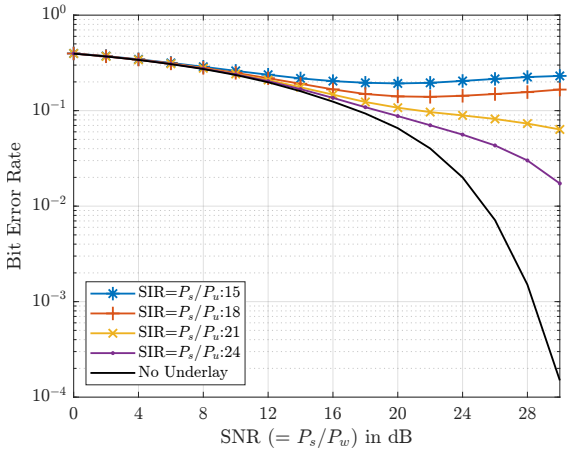

(d) 256-QAM modulation scheme

Figure 2.9: Bit Error Rate (BER) of OFDM with different modulation schemes and Underlay QPSK addition

selected modulation schemes correspond to those utilized by the 5G physical layer. Notably, a higher SIR has the most negligible impact on OFDM performance. That is because the underlay with higher SIR (i.e., lower power) won't displace the OFDM modulation symbols from their actual position on the constellation diagram. Adding underlay at a specific SIR significantly degrades the performance of OFDM, particularly for higher-order modulation schemes. From the plot, we can see for a particular SIR = 15 dB, the deviation of the BER curve when underlay is added from without addition is higher in the case of higher-order

modulation schemes. This degradation occurs because the addition of underlay symbols pushes the digital modulation symbols of OFDM toward their decision boundaries, causing deviation from their actual positions on the constellation diagram. Since, in higher modulation schemes where symbols are closer together in the constellation diagram, the area of decision region is less, the effect of underlay addition is higher on higher modulation schemes undergoing OFDM. For 256-QAM, the BER performance tends to rise as we increase the SNR after a certain threshold (18 dB) for particular SIRs, 15 and 18 dB, as shown in Fig. 2.9d. That is because when the SNR is low, the addition of noise pushes a few of the modulation symbols added with underlay back into their decision regions; however, once the SNR is high enough, the effect of underlay addition becomes significant, the addition pushes the modulation symbols out of their decision regions into adjacent symbol decision regions. We can also understand this effect from the perspective of the minimum distance, denoted as $d_{\min}$, between adjacent symbols in the constellation plot of modulation symbols undergoing OFDM modulation. If the underlay power P_u (or E_u, defined as the average energy of spread underlay symbols) exceeds $d_{\min}/2$, the underlay pushes the modulation symbols undergoing OFDM modulation into the decision region of their adjacent symbols. When the signal-to-noise ratio (SNR) is high, the noise addition does not significantly impact the modulation symbols' positions, and they remain in the region influenced by the underlay. However, in cases of low SNR, the noise addition may push some of the modulation symbols back into their original decision regions.

Clearly, there will be an optimal operating point for the underlay that minimizes its impact on 5G OFDM performance. To identify this operating point, one needs to analyze the relative underlay power compared to 5G OFDM power taking into account the modulation scheme used in the 5G OFDM chain, and the despreading gain that can be achieved from the spreading factor of codes.

2.5.1 Peak-to-Average Power Ratio Results

The Peak-to-Average Power Ratio (PAPR) is a significant issue encountered in transceivers using OFDM modulation. The PAPR problem can be understood from the perspective of the hardware's amplifier operation, which amplifies the received signal to enhance the performance of the transceiver system. The operation of any amplifier is characterized by two trends: linear operation and non-linear operation. As long as the signal received by the amplifier remains within the linear range, the amplifier operates linearly, amplifying the signal without any distortion. However, due to the IFFT operation involved in OFDM, there is a chance that the received signal peaks because of the summation operator. This deviation from the average power moves the amplifier into the non-linear operation, resulting in signal distortion. Consequently, this leads to the loss of orthogonality among the sub-carriers and causes inter-carrier interference, resulting in reduced OFDM performance.

The PAPR of the OFDM system is studied in terms of the complementary cumulative distribution function (CCDF). The CCDF of the random variable X is defined as the probability that X is greater than a specific value x and is typically expressed as

$$\bar{F_X}(x) = \Pr(X > x) = 1 - \Pr(X \leq x)$$

Thus, the PAPR of the signal being a random variable, the CCDF, shows that its probability exceeds a particular threshold. Since we add the underlay on the top of the OFDM signal and the same hardware transmits it, we would like to study the PAPR of underlay and 5G-OFDM co-existence.

Firstly, we examine the PAPR of the underlay signal without OFDM using Walsh codes. The spreading length considered here is 512. In Fig. 2.10, the PAPR in dB is plotted along

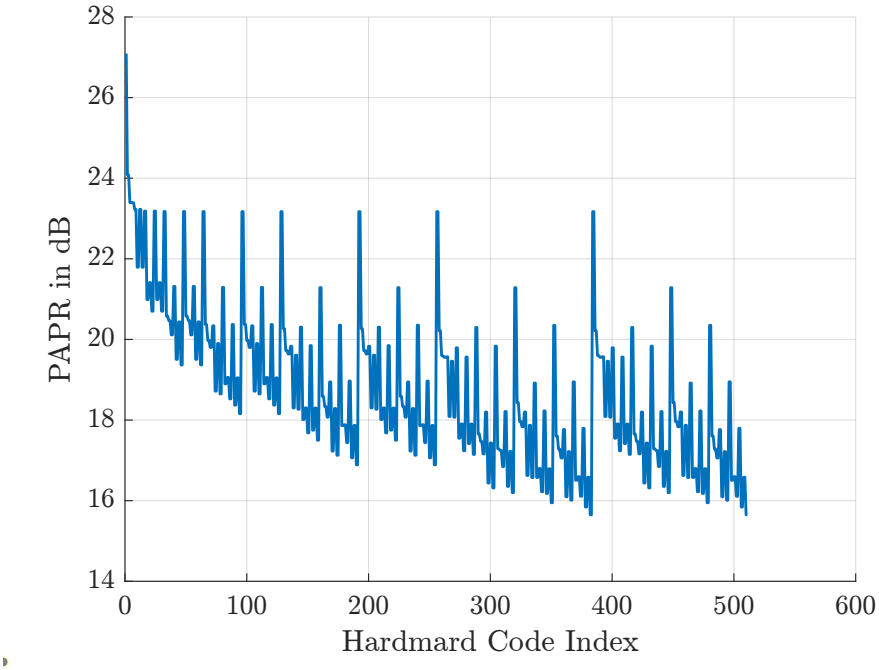

Figure 2.10: Peak-to-Average Power Ratio (PAPR) analysis of Underlay with different code indices from Walsh-Hadamard matrix

the Y-axis for each code of the Walsh-Hadamard matrix. The graph demonstrates that the PAPR decreases linearly; however, there are occasional spikes for certain codes. These higher PAPR values can be attributed to the periodicity inherent in the codes.

Notably, the code with an index of 1 exhibits the highest PAPR value of 26 dB. This code consists of consecutive 1's and -1's, contributing to its elevated PAPR. It is essential to consider that when spreading is performed in the frequency domain and followed by the IFFT operation, the presence of periodicity in the spreading code leads to higher values resembling impulses, shown in Fig. 2.11. Because of the periodicity involved in the code index 10, the output of IFFT resulted in spikes resembling impulses.

After combining the underlay signal with OFDM, the PAPR plot with different code indices of the Walsch-Hadamard matrix is shown in Fig. 2.12. For the code index of 300 and 500, the PAPR is almost the same as the PAPR of baseline OFDM, whereas the PAPR has deviated

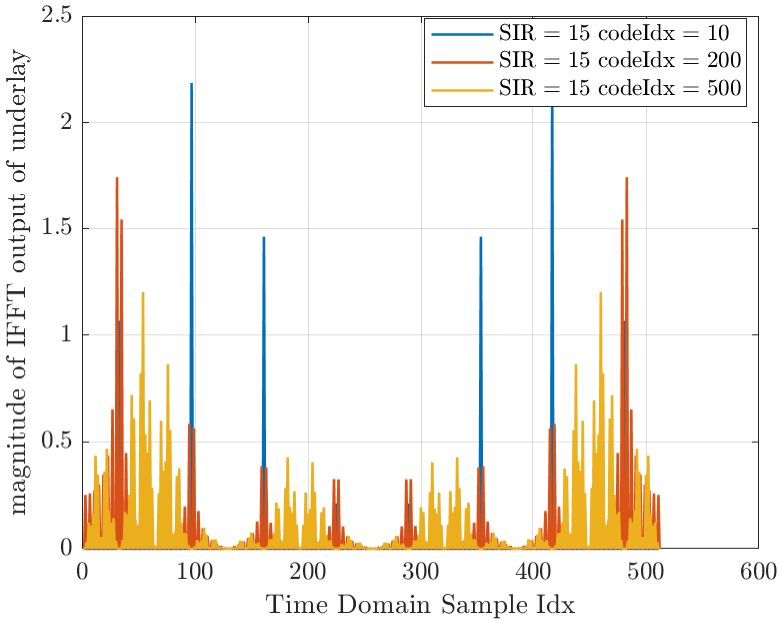

Figure 2.11: Magnitude of IFFT output of Underlay for different code indices from Walsh-Hadamard matrix

from baseline OFDM for the code index of 10.

Fig. 2.13 shows the PAPR plot when underlay is designed using different codes. The SIR of 15 dB and the randomness involved in the codes make the PAPR plot's performance similar to the baseline OFDM PAPR plot ((i.e., the case of "No Underlay").).

2.6 Conclusion

The simulations demonstrate the successful coexistence of the underlay and OFDM signals, enabling the transmission of a parallel channel alongside the OFDM signal. The results indicate that higher Signal-to-Interference Ratio (SIR) levels, achieved through reduced underlay power, have minimal impact on the performance of OFDM. Conversely, lower SIR levels adversely affect the underlay's performance. Thus to ensure reliable detection of the

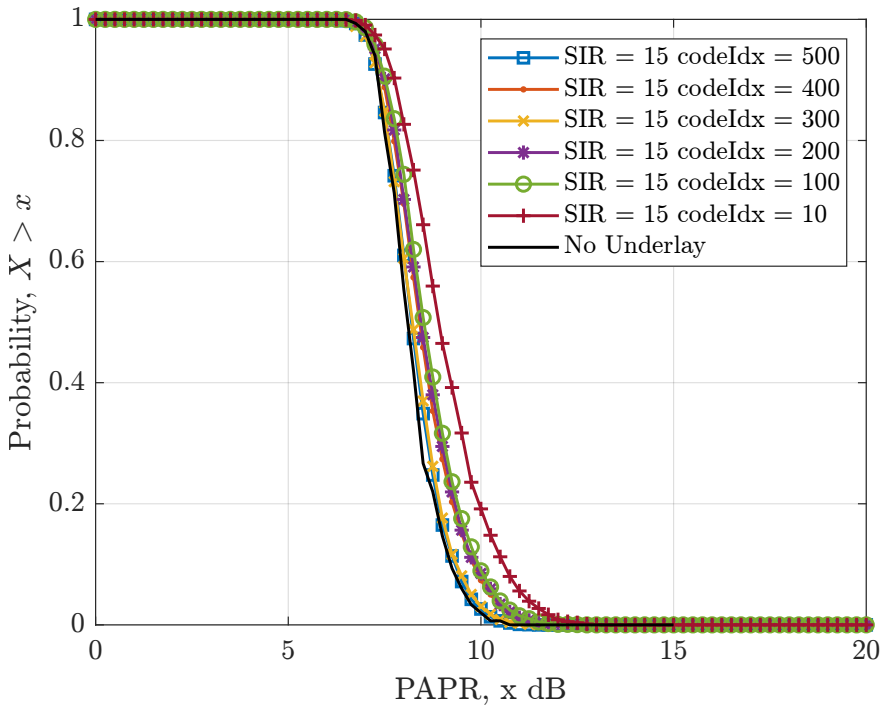

Figure 2.12: Peak-to-Average Power Ratio (PAPR) analysis of Underlay-OFDM Signal for different code indices from Walsh-Hadamard Matrix

underlay, it is advisable to employ a larger spreading factor. However, it is important to note that the underlay requires additional resources in terms of Resource Elements (REs) to transmit bits for larger spreading lengths, which in turn reduces the throughput of the underlay channel. The spreading gains from different codes are the same for codes having the same length. The PAPR analysis shows that it is advisable to choose the Hadamard code with less periodicity involved in it for spreading in the underlay channel.

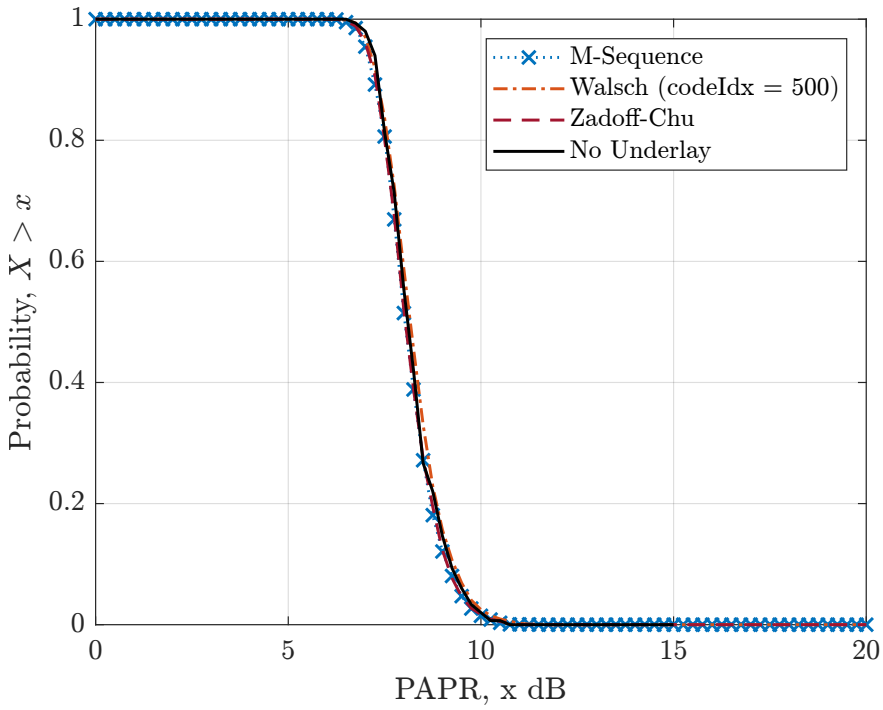

Figure 2.13: Peak-to-Average Power Ratio (PAPR) analysis of Underlay-OFDM Signal for different spreading codes

Chapter 3

Analytical Bit Error Rate Analysis of the Underlay - 5G OFDM Architecture

This chapter presents the analytical analysis of the proposed architecture in Chapter 2 by deriving the bit error rate (BER) expressions in the Additive White Gaussian noise (AWGN) channel and validating them with the link-level simulations in MATLAB. The expressions derived can be easily extended to the Rayleigh channel. We consider the modulation schemes used in 5G standards [28] for OFDM while employing BPSK/QPSK for the underlay.

There was previous research by Chakravarthy *et al.* [29] that investigated the BER expressions for primary and underlay signals within the context of cognitive radio technology, specifically targeting underlay for secondary users. The modulation scheme for primary signals was PSK. In contrast, in our work, the architecture proposed is different, employing underlay to primary users and studied in the context of a 5G-OFDM system. The simulation results confirm the accuracy and reliability of the derived BER expressions presented in this chapter. Additionally, the expression for BER of OFDM is generalized for M-QAM modulation. Our findings indicate that minimizing the impact on OFDM performance requires lower power for the underlay while achieving improved underlay decoding necessitates higher spreading factors while still operating at lower power.

The chapter is structured as follows. We begin by presenting the BER expressions of OFDM modulation without the underlay. Subsequently, we incorporate the underlay and derive the BER expressions of OFDM with underlay. Additionally, we derive the BER expressions of the underlay. Finally, we present a set of simulation results to illustrate the performance of both OFDM and underlay existing together.

3.1 Overview of System Architecture and Assumptions

At the Underlay 5G-OFDM receiver, the received samples after the removal of CP and FFT operation with an AWGN channel are expressed as

$$Y^i = S^i + U_l^k + W^i. \tag{3.1}$$

Without the numbering notation, we can view the received symbol Y as the combination of the transmitted spread underlay symbol U, the digital modulation symbols undergoing OFDM S, and the AWGN term denoted by $W \sim \mathcal{CN}(0, \sigma_w^2)$, which is given as

$$Y = S + U + W.$$

The received equalized symbols given by (2.5) are fed into the underlay receiver. These symbols, also denoted as Y_l^k (as per (2.3)), which corresponds to each transmitted underlay symbol U^k, are despread by the same spreading code employed at the transmitter, expressed as

$$\hat{U}^k = \frac{1}{L}\Sigma_{l=1}^{L} Y_l^k c_l^* = \frac{1}{L}\Sigma_{l=1}^{L} \left(U_l^k + S^{(k-1)L+l} + W_l^k\right) c_l^*. \tag{3.2}$$

In the above equation, $\hat{U}^k$ represents the despread underlay symbol, Y_l^k corresponds to the l-th spread underlay symbol of the received signal for the k-th underlay symbol, and c_l^*

denotes the complex conjugate of the spreading code. Applying the central limit theorem, the summation terms S and W in (3.2) result in a new Gaussian random variable, denoted as $\mathcal{M}$. The variance of OFDM interference to underlay term $\left(\Sigma_{l=1}^{L} S^{(k-1)L+l} c_l^*\right)$ is $E_s L$, and the variance of AWGN term $\left(\Sigma_{l=1}^{L} W_l^k c_l^*\right)$ is $L\sigma_w^2$, following the distribution

$$\mathcal{M} \sim \mathcal{CN}\left(0, \frac{E_s + \sigma_w^2}{L}\right). \tag{3.3}$$

with real part $m_I \sim \mathcal{N}\left(0, \frac{E_s+\sigma_w^2}{2L}\right)$ and with imaginary part $m_Q \sim \mathcal{N}\left(0, \frac{E_s+\sigma_w^2}{2L}\right)$.

We assume the symbols, $S^i \in \mathcal{S}$ and $U_l^k \in \mathcal{U}$ are equally likely with average symbol energies E_s and E_u, respectively, and the symbol errors occur due to the addition of AWGN pushing the symbols into their adjacent symbol's decision region only. Due to this, the decision boundary between any two symbols is the perpendicular bisector of the shortest distance line joining them, as shown in Fig. 3.1. The $\mathcal{S}$ and $\mathcal{U}$ are sets containing all possible modulation symbols pertaining to a chosen digital modulation scheme. The symbol error probability (Pr_S or SER) for any modulation scheme is defined as the average probability of error over all possible transmitted symbols and is given by

$$Pr_S = \frac{1}{M} \Sigma_{m=1}^{M} P(\hat{S} \neq S_m | S = S_m), \tag{3.4}$$

where $P(S_m)$ is the probability of symbol S_m is sent and $P(\hat{S} \neq S_m | S = S_m)$ is the conditional probability of symbol S_m is not received given that S_m is sent and M is the cardinality of a set $\mathcal{S}$. However, when the underlay is added, different phases of the underlay symbol affect each OFDM's digital modulation symbol differently; thus, the Pr_S becomes

$$\begin{aligned} Pr_S &= \Sigma_{m=1}^{M} P_{(S_m,U)}, \\ P_{(S_m,U)} &= \Sigma_{j=1}^{J} P(U_j) P(\hat{S} \neq S_m | S = S_m, U = U_j), \end{aligned} \tag{3.5}$$

where J is the cardinality of a set $\mathcal{U}$. Assuming grey coding is in use for mapping bits to symbols, making adjacent symbols differ by one bit, the BER is given as

$$BER = \frac{1}{\log_2 M} Pr_S. \tag{3.6}$$

The probability of symbol error is the complement of the probability of correctly detecting the symbol. To determine this probability, we multiply the probabilities of correctly detecting both the in-phase and quadrature components of the symbol. By applying this approach, we derive the BER expressions, considering both OFDM and underlay existing together.

3.2 BER of OFDM

This section examines QPSK, 16-QAM, and 64-QAM as digital modulation for the bits going through OFDM modulation. Dropping the underlay symbol from (3.1) yields in

$$Y = S + W$$

From this equation, we can imply that the performance of OFDM with a particular digital modulation (without underlay) is similar to that of a modulation scheme without OFDM in the AWGN channel.

3.2.1 QPSK modulation Scheme

Fig. 3.1a depicts the constellation of QPSK symbols. Each constellation point S_m ($m \in 1, 2, 3, 4$) has two decision boundaries at a distance of $d_{min}/2$, and the decision region has infinite extent in the other direction. Table 3.1 shows the distances of each symbol to the

Table 3.1: QPSK Symbol Decision Boundaries

$\mathcal{S}$	d_1	d_2	d_3	d_4
$S_1 = \sqrt{\frac{E_s}{2}}(+1 + j1)$	∞	$-\sqrt{\frac{E_s}{2}}$	∞	$-\sqrt{\frac{E_s}{2}}$
$S_2 = \sqrt{\frac{E_s}{2}}(-1 + j1)$	$\sqrt{\frac{E_s}{2}}$	$-\infty$	∞	$-\sqrt{\frac{E_s}{2}}$
$S_3 = \sqrt{\frac{E_s}{2}}(-1 - j1)$	$\sqrt{\frac{E_s}{2}}$	$-\infty$	$\sqrt{\frac{E_s}{2}}$	$-\infty$
$S_4 = \sqrt{\frac{E_s}{2}}(+1 - j1)$	∞	$-\sqrt{\frac{E_s}{2}}$	$\sqrt{\frac{E_s}{2}}$	$-\infty$

decision boundaries. Since all symbols are equally likely and the constellation is symmetric, the symbol error rate is the same for all symbols and is equal to one of the symbol's symbol error rates.

$$P_{SE2} = Pr_S = P(\hat{S} \neq S_m | S = S_m).$$

The term $SE2$ defines the symbol with the two finite decision boundaries. Let's consider the symbol S_1 in the first quadrant of the constellation. The probability of the in-phase component being in error can be expressed as

$$P(S_I + W_I < S_I + d_2) = P(W_I > -d_2) = P\left(W_I > \sqrt{\frac{E_s}{2}}\right).$$

Here, $d_2 = -\sqrt{\frac{E_s}{2}}$. Similarly, the probability of the quadrature component being in error can be expressed as

$$P(S_Q + W_Q < S_Q + d_4) = P\left(W_Q > \sqrt{\frac{E_s}{2}}\right).$$

Then, the probability of correctly detecting the symbol (P^C_{SE2}) is given by the product of both in-phase and quadrature components, not in error. We can write this in terms of Q-function

as

$$\left[1 - P\left(W_I > \sqrt{\frac{E_s}{2}}\right)\right] \times \left[1 - P\left(W_Q > \sqrt{\frac{E_s}{2}}\right)\right],$$
$$\left[1 - Q\left(\sqrt{\frac{E_s}{\sigma_w^2}}\right)\right] \times \left[1 - Q\left(\sqrt{\frac{E_s}{\sigma_w^2}}\right)\right],$$
$$1 - 2Q\left(\sqrt{\frac{E_s}{\sigma_w^2}}\right) + \left(Q\left(\sqrt{\frac{E_s}{\sigma_w^2}}\right)\right)^2.$$

The SER as defined previously, $P_{SE2} = 1 - P_{SE2}^C$, can be expressed as

$$P_{SE2} = Pr_S = 2Q\left(\sqrt{\frac{E_s}{\sigma_w^2}}\right) - \left(Q\left(\sqrt{\frac{E_s}{\sigma_w^2}}\right)\right)^2.$$

From (3.6), we can express the bit error rate (BER) as:

$$BER = Q\left(\sqrt{\frac{E_s}{\sigma_w^2}}\right) - \frac{1}{2}\left(Q\left(\sqrt{\frac{E_s}{\sigma_w^2}}\right)\right)^2.$$

3.2.2 QAM modulation Scheme

Fig. 3.1b shows the QAM constellation diagrams for 16-QAM and 64-QAM. Assuming that the transmitted symbols are equally likely, the symbols in the QAM constellation can be grouped into four sets, with each symbol in a set having the same symbol error rate due to the symmetry of the constellation. We will use the following notation to denote the groups and their corresponding symbol error rates:

- $Group - 1$: The first group has four finite decision boundaries, with a symbol error

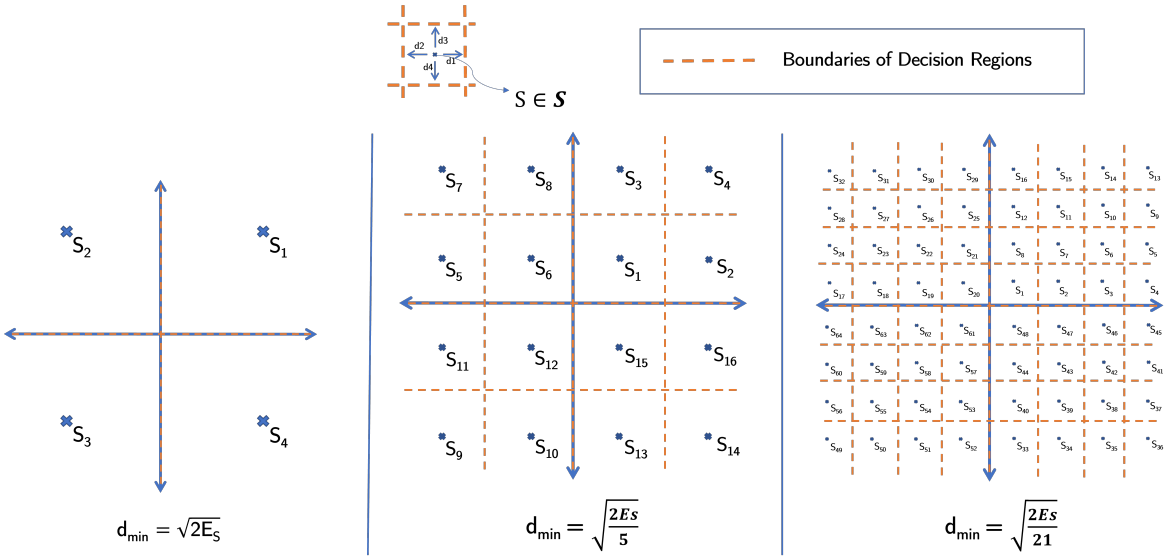

(a) QPSK (b) QAM: 16-QAM (left) and 64-QAM (right)

Figure 3.1: Constellation Diagrams with decision boundaries (orange lines) in a two-dimensional coordinate system. The origin is denoted by S, and d_1, d_2, d_3, and d_4 represent the distances from S to the decision boundaries in the in-phase and quadrature-phase components.

rate of P_{SE4}. See, for example, the symbol S_1 of 16-QAM in Fig. 3.1b.

- *Group* − 2: The second group has three finite decision boundaries and a fourth decision boundary at an infinite extent in the direction of the in-phase component, with a symbol error rate of P'_{SE3}. See, for example, the symbol S_2 of 16-QAM in Fig. 3.1b.

- *Group* − 3: The third group has three finite decision boundaries and a fourth decision boundary at an infinite extent in the direction of the quadrature-phase component, with a symbol error rate of P''_{SE3}. See, for example, the symbol S_3 of 16-QAM in Fig. 3.1b.

- *Group* − 4: The fourth group has two finite decision boundaries and two decision boundaries at an infinite extent in the direction of the in-phase and quadrature-phase components, with a symbol error rate of P_{SE2}. See, for example, the symbol S_4 of

16-QAM in Fig. 3.1b.

Each group has a certain number of symbols belonging to it, depending on the constellation (order of QAM modulation). For 16-QAM, each group has four symbols. For 64-QAM, the first group has 36 symbols, the second and third groups have 12 symbols, and the fourth group has four symbols. Note that the second and third groups have a fourth decision boundary at infinity but in different components. The minimum distance between the symbols in terms of the average energy of symbols E_s is expressed as

$$d_{min} = \sqrt{\frac{6E_s}{M-1}}$$

Table 3.2 shows the distances of each symbol from the first quadrant to their decision boundaries.

Table 3.2: 16QAM Symbol Decision Boundaries in the First Quadrant

$\mathcal{S}$	d_1	d_2	d_3	d_4
$S_1 = \sqrt{\frac{E_s}{10}}(+1+j1)$	$+\sqrt{\frac{E_s}{10}}$	$-\sqrt{\frac{E_s}{10}}$	$+\sqrt{\frac{E_s}{10}}$	$-\sqrt{\frac{E_s}{10}}$
$S_2 = \sqrt{\frac{E_s}{10}}(+3+j1)$	$+\infty$	$-\sqrt{\frac{E_s}{10}}$	$+\sqrt{\frac{E_s}{10}}$	$-\sqrt{\frac{E_s}{10}}$
$S_3 = \sqrt{\frac{E_s}{10}}(+1+j3)$	$\sqrt{\frac{E_s}{10}}$	$-\sqrt{\frac{E_s}{10}}$	$+\infty$	$-\sqrt{\frac{E_s}{10}}$
$S_4 = \sqrt{\frac{E_s}{10}}(+3+j3)$	∞	$-\sqrt{\frac{E_s}{10}}$	∞	$-\sqrt{\frac{E_s}{10}}$

16-QAM

The average SER from (3.4) can be expressed as

$$Pr_S = \frac{1}{4}\left(P_{SE4} + P'_{SE3} + P''_{SE3} + P_{SE2}\right). \tag{3.7}$$

Considering the symbol S_1 for calculating P_{SE4}. The probability of the in-phase component being in error, using the values of d_1 and d_2 from Table 3.2, is given by

$$P(S_I + W_I < S_I + d_2) + P(S_I + W_I > S_I + d_1),$$
$$P\left(W_I < -\sqrt{\frac{E_s}{10}}\right) + P\left(W_I > +\sqrt{\frac{E_s}{10}}\right),$$
$$2P\left(W_I > +\sqrt{\frac{E_s}{10}}\right).$$

Similarly, the probability of the quadrature component being in error is given as

$$2P\left(W_Q > +\sqrt{\frac{E_s}{10}}\right).$$

Then, the probability of correct detection P^C_{SE4} is

$$\left[1 - 2P\left(W_I > +\sqrt{\frac{E_s}{10}}\right)\right] \times \left[1 - 2P\left(W_Q > +\sqrt{\frac{E_s}{10}}\right)\right],$$
$$\left[1 - 2Q\left(\sqrt{\frac{E_s}{5\sigma_w^2}}\right)\right] \times \left[1 - 2Q\left(\sqrt{\frac{E_s}{5\sigma_w^2}}\right)\right],$$
$$1 - 4Q\left(\sqrt{\frac{E_s}{5\sigma_w^2}}\right) + 4\left(Q\left(\sqrt{\frac{E_s}{5\sigma_w^2}}\right)\right)^2.$$

The SER of the symbol S_1 is $P_{SE4} = 1 - P^C_{SE4}$, which is given as

$$P_{SE4} = 4Q\left(\sqrt{\frac{E_s}{5\sigma_w^2}}\right) - 4\left(Q\left(\sqrt{\frac{E_s}{5\sigma_w^2}}\right)\right)^2. \tag{3.8}$$

Now, considering the symbol S_2 for calculating P'_{SE3}. The probability of the in-phase com-

ponent in error, using the values of d_1 and d_2 from Table 3.2, is given by

$$P(S_I + W_I < S_I + d_2) + P(S_I + W_I > S_I + d_1),$$
$$P\left(W_I < -\sqrt{\frac{E_s}{10}}\right) + P\left(W_I > +\infty\right),$$
$$P\left(W_I > +\sqrt{\frac{E_s}{10}}\right).$$

Similarly, the probability of the quadrature component being in error is given as

$$2P\left(W_Q > +\sqrt{\frac{E_s}{10}}\right).$$

Then, the probability of correct detection P^C_{SE3} is given as

$$\left[1 - P\left(W_I > +\sqrt{\frac{E_s}{10}}\right)\right] \times \left[1 - 2P\left(W_Q > +\sqrt{\frac{E_s}{10}}\right)\right],$$
$$\left[1 - Q\left(\sqrt{\frac{E_s}{5\sigma_w^2}}\right)\right] \times \left[1 - 2Q\left(\sqrt{\frac{E_s}{5\sigma_w^2}}\right)\right],$$
$$1 - 3Q\left(\sqrt{\frac{E_s}{5\sigma_w^2}}\right) + 2\left(Q\left(\sqrt{\frac{E_s}{5\sigma_w^2}}\right)\right)^2.$$

The SER of the symbol S_2 is $P^{'}_{SE3} = 1 - P^C_{SE3}$, which is given as

$$P^{'}_{SE3} = 3Q\left(\sqrt{\frac{E_s}{5\sigma_w^2}}\right) - 2\left(Q\left(\sqrt{\frac{E_s}{5\sigma_w^2}}\right)\right)^2. \tag{3.9}$$

Deriving similarly, we get $P^{''}_{SE3}$ is equal to $P^{'}_{SE3}$, due to the symmetry of the constellation. Lastly, considering the symbol S_4 for calculating P_{SE2}. The probability of the in-phase

component being in error, using the values of d_1 and d_2 from Table 3.2, is given by

$$P(S_I + W_I < S_I + d_2) + P(S_I + W_I > S_I + d_1),$$
$$P\left(W_I < -\sqrt{\frac{E_s}{10}}\right) + P\left(W_I > +\infty\right),$$
$$P\left(W_I > +\sqrt{\frac{E_s}{10}}\right).$$

Similarly, the probability of the quadrature component being in error is given as

$$P\left(W_Q > +\sqrt{\frac{E_s}{10}}\right).$$

Then, the probability of correct detection P_{SE2}^C is given as

$$\left[1 - P\left(W_I > +\sqrt{\frac{E_s}{10}}\right)\right] \times \left[1 - P\left(W_Q > +\sqrt{\frac{E_s}{10}}\right)\right],$$
$$\left[1 - Q\left(\sqrt{\frac{E_s}{5\sigma_w^2}}\right)\right] \times \left[1 - Q\left(\sqrt{\frac{E_s}{5\sigma_w^2}}\right)\right],$$
$$1 - 2Q\left(\sqrt{\frac{E_s}{5\sigma_w^2}}\right) + \left(Q\left(\sqrt{\frac{E_s}{5\sigma_w^2}}\right)\right)^2.$$

The SER of the symbol S_4 is $P_{SE2} = 1 - P_{SE2}^C$, which is given as

$$P_{SE2} = 2Q\left(\sqrt{\frac{E_s}{5\sigma_w^2}}\right) - \left(Q\left(\sqrt{\frac{E_s}{5\sigma_w^2}}\right)\right)^2. \tag{3.10}$$

By substituting (3.8), (3.9), and (3.10) into (3.7), we obtain:

$$Pr_S = \frac{1}{4}\left[12Q\left(\sqrt{\frac{E_s}{5\sigma_w^2}}\right) - 9\left(Q\left(\sqrt{\frac{E_s}{5\sigma_w^2}}\right)\right)^2\right],$$

$$BER = \frac{1}{16}\left[12Q\left(\sqrt{\frac{E_s}{5\sigma_w^2}}\right) - 9\left(Q\left(\sqrt{\frac{E_s}{5\sigma_w^2}}\right)\right)^2\right].$$

64-QAM

Compared with 16QAM, the probability of symbol error rate calculation for 64QAM differs (1) in the count of symbols in each constellation group and (2) the distance to the decision boundary. From (3.4), we can express the average SER as

$$Pr_S = \frac{1}{16}\left(9P_{SE4} + 3P'_{SE3} + 3P''_{SE3} + P_{SE2}\right), \tag{3.11}$$

where

$$P_{SE4} = 4Q\left(\sqrt{\frac{E_s}{21\sigma_w^2}}\right) - 4\left(Q\left(\sqrt{\frac{E_s}{21\sigma_w^2}}\right)\right)^2,$$
$$P''_{SE3} = P'_{SE3} = 3Q\left(\sqrt{\frac{E_s}{21\sigma_w^2}}\right) - 2\left(Q\left(\sqrt{\frac{E_s}{21\sigma_w^2}}\right)\right)^2,$$
$$P_{SE2} = 2Q\left(\sqrt{\frac{E_s}{21\sigma_w^2}}\right) - \left(Q\left(\sqrt{\frac{E_s}{21\sigma_w^2}}\right)\right)^2,$$

and

$$Pr_S = \frac{1}{8}\left[29Q\left(\sqrt{\frac{E_s}{21\sigma_w^2}}\right) - 25\left(Q\left(\sqrt{\frac{E_s}{21\sigma_w^2}}\right)\right)^2\right],$$

$$BER = \frac{1}{48}\left[29Q\left(\sqrt{\frac{E_s}{21\sigma_w^2}}\right) - 25\left(Q\left(\sqrt{\frac{E_s}{21\sigma_w^2}}\right)\right)^2\right].$$

3.3 BER of OFDM in the Underlay 5G-OFDM System

In this section, we will derive the BER expression of OFDM with QPSK and 16-QAM modulation schemes and show the BER expressions for M-order QAM modulation schemes added with underlay in the AWGN channel. We will derive BER expressions for the two variants of underlay symbols added to the OFDM signal: BPSK with no phase offset and QPSK with the phase offset of 45°.

3.3.1 OFDM QPSK modulation with underlay BPSK modulation

Underlay symbols as BPSK, $U = \{\sqrt{E_u}, -\sqrt{E_u}\}$

We suppose U = $\sqrt{E_u}$ is transmitted along with the symbol S_1. The probability of the in-phase component of the symbol S_1 is in error is given by

$$P(S_I + \sqrt{E_u} + W_I < S_I + d_2),$$
$$P(W_I > +\sqrt{E_u} - d_2),$$
$$P\left(W_I > -\sqrt{E_u} + \sqrt{\frac{E_s}{2}}\right).$$

Here, $d_2 = -\sqrt{\frac{E_s}{2}}$. Since there is no quadrature component for the underlay, the quadrature component of the symbol S_1 in error is the same as without the underlay added,

$$P\left(W_Q > \sqrt{\frac{E_s}{2}}\right).$$

Now, the probability of correct detection of the symbol can be expressed as

$$\left[1 - P\left(W_I > -\sqrt{E_u} + \sqrt{\frac{E_s}{2}}\right)\right] \times \left[1 - P\left(W_Q > \sqrt{\frac{E_s}{2}}\right)\right].$$

By expressing the probability in terms of Q-function, we can represent the SER given that $S = S_1$ & $U = +\sqrt{E_u}$ as follows

$$P(\hat{S} \neq S_1 | S = S_1, U = +\sqrt{E_u}) = \left[1 - Q\left(-\sqrt{\frac{2E_u}{\sigma_w^2}} + \sqrt{\frac{E_s}{\sigma_w^2}}\right)\right] \times \left[1 - Q\left(\sqrt{\frac{E_s}{\sigma_w^2}}\right)\right].$$

Similarly, for $U = -\sqrt{E_u}$, we have:

$$P(\hat{S} \neq S_1 | S = S_1, U = -\sqrt{E_u}) = \left[1 - Q\left(+\sqrt{\frac{2E_u}{\sigma_w^2}} + \sqrt{\frac{E_s}{\sigma_w^2}}\right)\right] \times \left[1 - Q\left(\sqrt{\frac{E_s}{\sigma_w^2}}\right)\right].$$

Thus, the SER from (3.5) is given as

$$\begin{aligned} Pr_S = &\frac{1}{2}\left(1 - \left[1 - Q\left(-\sqrt{\frac{2E_u}{\sigma_w^2}} + \sqrt{\frac{E_s}{\sigma_w^2}}\right)\right] \times \left[1 - Q\left(\sqrt{\frac{E_s}{\sigma_w^2}}\right)\right]\right) + \\ &\frac{1}{2}\left(1 - \left[1 - Q\left(+\sqrt{\frac{2E_u}{\sigma_w^2}} + \sqrt{\frac{E_s}{\sigma_w^2}}\right)\right] \times \left[1 - Q\left(\sqrt{\frac{E_s}{\sigma_w^2}}\right)\right]\right) \end{aligned}$$

and bit error rate as

$$\begin{aligned} BER = &\frac{1}{4}\left(1 - \left[1 - Q\left(-\sqrt{\frac{2E_u}{\sigma_w^2}} + \sqrt{\frac{E_s}{\sigma_w^2}}\right)\right] \times \left[1 - Q\left(\sqrt{\frac{E_s}{\sigma_w^2}}\right)\right]\right) + \\ &\frac{1}{4}\left(1 - \left[1 - Q\left(+\sqrt{\frac{2E_u}{\sigma_w^2}} + \sqrt{\frac{E_s}{\sigma_w^2}}\right)\right] \times \left[1 - Q\left(\sqrt{\frac{E_s}{\sigma_w^2}}\right)\right]\right) \end{aligned}$$

3.3.2 OFDM QPSK modulation with underlay QPSK modulation

Underlay symbols as QPSK,

$$U = \{+\sqrt{\tfrac{E_u}{2}} + j\sqrt{\tfrac{E_u}{2}}, -\sqrt{\tfrac{E_u}{2}} + j\sqrt{\tfrac{E_u}{2}}, -\sqrt{\tfrac{E_u}{2}} - j\sqrt{\tfrac{E_u}{2}}, +\sqrt{\tfrac{E_u}{2}} - j\sqrt{\tfrac{E_u}{2}}\}$$

Deriving BER in a similar manner to the previous section, we find that

$$\begin{aligned} BER = &\frac{1}{8}\left[1 - \left[1 - Q\left(-\sqrt{\frac{E_u}{\sigma_w^2}} + \sqrt{\frac{E_s}{\sigma_w^2}}\right)\right] \times \left[1 - Q\left(-\sqrt{\frac{E_u}{\sigma_w^2}} + \sqrt{\frac{E_s}{\sigma_w^2}}\right)\right]\right] + \\ &\frac{1}{8}\left[1 - \left[1 - Q\left(+\sqrt{\frac{E_u}{\sigma_w^2}} + \sqrt{\frac{E_s}{\sigma_w^2}}\right)\right] \times \left[1 - Q\left(+\sqrt{\frac{E_u}{\sigma_w^2}} + \sqrt{\frac{E_s}{\sigma_w^2}}\right)\right]\right] + \\ &\frac{1}{8}\left[1 - \left[1 - Q\left(-\sqrt{\frac{E_u}{\sigma_w^2}} + \sqrt{\frac{E_s}{\sigma_w^2}}\right)\right] \times \left[1 - Q\left(+\sqrt{\frac{E_u}{\sigma_w^2}} + \sqrt{\frac{E_s}{\sigma_w^2}}\right)\right]\right] + \\ &\frac{1}{8}\left[1 - \left[1 - Q\left(+\sqrt{\frac{E_u}{\sigma_w^2}} + \sqrt{\frac{E_s}{\sigma_w^2}}\right)\right] \times \left[1 - Q\left(-\sqrt{\frac{E_u}{\sigma_w^2}} + \sqrt{\frac{E_s}{\sigma_w^2}}\right)\right]\right]. \end{aligned}$$

3.3.3 OFDM 16-QAM modulation with underlay BPSK modulation

Underlay symbols as BPSK, $U = \{\sqrt{E_u}, -\sqrt{E_u}\}$

Considering the symbol with four boundaries (e.g., S_1 in the first quadrant) and $U = +\sqrt{E_u}$ is sent. The probability of the in-phase component of the symbol in error and substituting the values of d_1 and d_2 from Table 3.2 is

$$\begin{aligned} &P(S_I + \sqrt{E_u} + W_I < S_I + d_2) + P(S_I + \sqrt{E_u} + W_I > S_I + d_1), \\ &P(W_I > +\sqrt{E_u} - d_2) + P(W_I > -\sqrt{E_u} + d_1), \\ &P\left(W_I > +\sqrt{E_u} + \sqrt{\frac{E_s}{10}}\right) + P\left(W_I > -\sqrt{E_u} + \sqrt{\frac{E_s}{10}}\right). \end{aligned}$$

Since the underlay symbol has no quadrature component, the quadrature component of the symbol S_1 in error is

$$2P\left(W_Q > \sqrt{\frac{E_s}{10}}\right).$$

Then, the probability of correctly detecting the symbol is

$$\left[1 - \left(P\left(W_I > +\sqrt{E_u} + \sqrt{\frac{E_s}{10}}\right) + P\left(W_I > -\sqrt{E_u} + \sqrt{\frac{E_s}{10}}\right)\right)\right] \times \left[1 - 2P\left(W_Q > \sqrt{\frac{E_s}{10}}\right)\right].$$

By expressing the probability in terms of Q-function, we can represent the SER given that $S = S_1$ & $U = +\sqrt{E_u}$ as follows

$$P(\hat{S} \neq S_1 | S = S_1, U = \sqrt{E_u}) = 1 - \left[1 - \left(Q\left(+\sqrt{\frac{2E_u}{\sigma_w^2}} + \sqrt{\frac{E_s}{5\sigma_w^2}}\right) + Q\left(-\sqrt{\frac{2E_u}{\sigma_w^2}} + \sqrt{\frac{E_s}{5\sigma_w^2}}\right)\right)\right] \times \left[1 - 2Q\left(\sqrt{\frac{E_s}{5\sigma_w^2}}\right)\right].$$

Similarly, we have,

$$P(\hat{S} \neq S_1 | S = S_1, U = -\sqrt{E_u}) = 1 - \left[1 - \left(Q\left(+\sqrt{\frac{2E_u}{\sigma_w^2}} + \sqrt{\frac{E_s}{5\sigma_w^2}}\right) + Q\left(-\sqrt{\frac{2E_u}{\sigma_w^2}} + \sqrt{\frac{E_s}{5\sigma_w^2}}\right)\right)\right] \left[1 - 2Q\left(\sqrt{\frac{E_s}{5\sigma_w^2}}\right)\right].$$

The SER of the symbol S_1 is

$$P_{SE4} = 1 - \left[1 - \left(Q\left(+\sqrt{\frac{2E_u}{\sigma_w^2}} + \sqrt{\frac{E_s}{5\sigma_w^2}}\right) + Q\left(-\sqrt{\frac{2E_u}{\sigma_w^2}} + \sqrt{\frac{E_s}{5\sigma_w^2}}\right)\right)\right] \times \left[1 - 2Q\left(\sqrt{\frac{E_s}{5\sigma_w^2}}\right)\right].$$

Now, lets examine S_2 and $U = +\sqrt{E_u}$ is sent. The probability of the in-phase component of the symbol in error and substituting the values of d_1 and d_2 from Table 3.2 is

$$\begin{aligned}
&P(S_I + \sqrt{E_u} + W_I < S_I + d_2) + P(S_I + \sqrt{E_u} + W_I > S_I + d_1),\\
&P(W_I > +\sqrt{E_u} - d_2) + P(W_I > -\sqrt{E_u} + d_1),\\
&P\left(W_I > +\sqrt{E_u} + \sqrt{\frac{E_s}{10}}\right) + P(W_I > -\sqrt{E_u} + \infty),\\
&P\left(W_I > +\sqrt{E_u} + \sqrt{\frac{E_s}{10}}\right).
\end{aligned}$$

Since there is no quadrature component in the underlay, the quadrature component of the symbol S_2 in error is

$$2P\left(W_Q > \sqrt{\frac{E_s}{10}}\right).$$

Then, the probability of correct detection of the symbol S_2 is

$$\left[1 - P\left(W_I > +\sqrt{E_u} + \sqrt{\frac{E_s}{10}}\right)\right] \times \left[1 - 2P\left(W_Q > \sqrt{\frac{E_s}{10}}\right)\right].$$

By expressing the probability in terms of Q-function, we can represent the SER given that $S = S_2$ & $U = +\sqrt{E_u}$ as follows

$$P(\hat{S} \neq S_2 | S = S_2, U = \sqrt{E_u}) = 1 - \left[1 - Q\left(+\sqrt{\frac{2E_u}{\sigma_w^2}} + \sqrt{\frac{E_s}{5\sigma_w^2}}\right)\right] \times \left[1 - 2Q\left(\sqrt{\frac{E_s}{5\sigma_w^2}}\right)\right].$$

Similarly, we get,

$$P(\hat{S} \neq S_2 | S = S_2, U = -\sqrt{E_u}) = 1 - \left[1 - Q\left(-\sqrt{\frac{2E_u}{\sigma_w^2}} + \sqrt{\frac{E_s}{5\sigma_w^2}}\right)\right] \times \left[1 - 2Q\left(\sqrt{\frac{E_s}{5\sigma_w^2}}\right)\right].$$

The SER of the symbols S_2 is

$$P_{SE3}^{'} = 1 - \left[1 - \frac{1}{2}\left(Q\left(+\sqrt{\frac{2E_u}{\sigma_w^2}} + \sqrt{\frac{E_s}{5\sigma_w^2}}\right) + Q\left(-\sqrt{\frac{2E_u}{\sigma_w^2}} + \sqrt{\frac{E_s}{5\sigma_w^2}}\right)\right)\right] \times \left[1 - 2Q\left(\sqrt{\frac{E_s}{5\sigma_w^2}}\right)\right].$$

Next, we consider the symbol S_3 and $U = +\sqrt{E_u}$ is sent. The probability of the in-phase component of the symbol S_3 in error is given by

$$P(S_I + \sqrt{E_u} + W_I < S_I + d_2) + P(S_I + \sqrt{E_u} + W_I > S_I + d_1),$$
$$P(W_I > +\sqrt{E_u} - d_2) + P(W_I > -\sqrt{E_u} + d_1),$$
$$P\left(W_I > +\sqrt{E_u} + \sqrt{\frac{E_s}{10}}\right) + P\left(W_I > -\sqrt{E_u} + \sqrt{\frac{E_s}{10}}\right).$$

Since there is no quadrature component in the underlay, the quadrature component of the

symbol S_3 in error is

$$P\left(W_Q > \sqrt{\frac{E_s}{10}}\right).$$

Then, the probability of correct detection of the symbol is

$$\left[1 - \left(P\left(W_I > \sqrt{E_u} + \sqrt{\frac{E_s}{10}}\right) + P\left(W_I > -\sqrt{E_u} + \sqrt{\frac{E_s}{10}}\right)\right)\right] \times \left[1 - P\left(W_Q > \sqrt{\frac{E_s}{10}}\right)\right].$$

By expressing the probability in terms of Q-function, we can represent the SER given that $S = S_3$ & $U = +\sqrt{E_u}$ as follows

$$P(\hat{S} \neq S_3 | S = S_3, U = +\sqrt{E_u}) = 1 - \left[1 - \left(Q\left(+\sqrt{\frac{2E_u}{\sigma_w^2}} + \sqrt{\frac{E_s}{5\sigma_w^2}}\right) + Q\left(-\sqrt{\frac{2E_u}{\sigma_w^2}} + \sqrt{\frac{E_s}{5\sigma_w^2}}\right)\right)\right] \times \left[1 - Q\left(\sqrt{\frac{E_s}{5\sigma_w^2}}\right)\right].$$

Similarly, we get,

$$P(\hat{S} \neq S_3 | S = S_3, U = -\sqrt{E_u}) = 1 - \left[1 - \left(Q\left(+\sqrt{\frac{2E_u}{\sigma_w^2}} + \sqrt{\frac{E_s}{5\sigma_w^2}}\right) + Q\left(-\sqrt{\frac{2E_u}{\sigma_w^2}} + \sqrt{\frac{E_s}{5\sigma_w^2}}\right)\right)\right] \times \left[1 - Q\left(\sqrt{\frac{E_s}{5\sigma_w^2}}\right)\right].$$

The SER of the symbols S_3 is

$$P''_{SE3} = 1 - \left[1 - \left(Q\left(+\sqrt{\frac{2E_u}{\sigma_w^2}} + \sqrt{\frac{E_s}{5\sigma_w^2}}\right) + Q\left(-\sqrt{\frac{2E_u}{\sigma_w^2}} + \sqrt{\frac{E_s}{5\sigma_w^2}}\right)\right)\right] \times \left[1 - Q\left(\sqrt{\frac{E_s}{5\sigma_w^2}}\right)\right].$$

Lastly, considering the symbol with two boundaries (e.g., S_4 in the first quadrant) and $U = +\sqrt{E_u}$ is sent. The probability of the in-phase component of the symbol in the first quadrant in error is given by

$$P\left(S_I + \sqrt{E_u} + W_I < S_I + d_2\right) + P\left(S_I + \sqrt{E_u} + W_I > S_I + d_1\right),$$
$$P\left(W_I > +\sqrt{E_u} - d_2\right) + P\left(W_I > -\sqrt{E_u} + d_1\right),$$
$$P\left(W_I > +\sqrt{E_u} + \sqrt{\frac{E_s}{10}}\right) + P\left(W_I > -\sqrt{E_u} + \infty\right),$$
$$P\left(W_I > +\sqrt{E_u} + \sqrt{\frac{E_s}{10}}\right).$$

Since there is no quadrature component in the underlay, the quadrature component of the symbol in error is

$$P\left(W_Q > \sqrt{\frac{E_s}{10}}\right).$$

Then, the probability of correct detection of the symbol is

$$\left[1 - P\left(W_I > +\sqrt{E_u} + \sqrt{\frac{E_s}{10}}\right)\right] \times \left[1 - P\left(W_Q > \sqrt{\frac{E_s}{10}}\right)\right].$$

By expressing the probability in terms of Q-function, we can represent the SER given that $S = S_4$ & $U = +\sqrt{E_u}$ as follows:

$$P(\hat{S} \neq S_4 | S = S_4, U = +\sqrt{E_u}) = 1 - \left[1 - Q\left(+\sqrt{\frac{2E_u}{\sigma_w^2}} + \sqrt{\frac{E_s}{5\sigma_w^2}}\right)\right] \times$$
$$\left[1 - Q\left(\sqrt{\frac{E_s}{5\sigma_w^2}}\right)\right].$$

Similarly, we get,

$$P(\hat{S} \neq S_4 | S = S_4, U = -\sqrt{E_u}) = 1 - \left[1 - Q\left(-\sqrt{\frac{2E_u}{\sigma_w^2}} + \sqrt{\frac{E_s}{5\sigma_w^2}}\right)\right] \times \left[1 - Q\left(\sqrt{\frac{E_s}{5\sigma_w^2}}\right)\right].$$

The SER of S_4 is

$$P_{SE2} = 1 - \left[1 - \frac{1}{2}\left(Q\left(+\sqrt{\frac{2E_u}{\sigma_w^2}} + \sqrt{\frac{E_s}{5\sigma_w^2}}\right) + Q\left(-\sqrt{\frac{2E_u}{\sigma_w^2}} + \sqrt{\frac{E_s}{5\sigma_w^2}}\right)\right)\right] \times \left[1 - Q\left(\sqrt{\frac{E_s}{5\sigma_w^2}}\right)\right].$$

From (3.4), the average SER is now expressed as

$$Pr_S = \frac{1}{4}\left(P_{SE4} + P'_{SE3} + P''_{SE3} + P_{SE2}\right). \tag{3.12}$$

The SER for QAM modulation with underlay symbols can be analyzed in a generalized manner. Specifically, the SER of a QAM symbol depends on the type of underlay symbol added, which can be either BPSK or QPSK. We summarize the SER values for each QAM symbol (belonging to the group) with underlay symbols in Tables 3.3 and 3.5, respectively. In each table, the elements represent the conditional probability $P(\hat{S} \neq S_m | S = S_m, U = U_j)$, where S_m denotes the QAM symbol belonging to a group and U_j denotes the underlay symbol added. To calculate the overall SER of the QAM signal with underlay, we can plug in the SER values from the tables into (3.5).

Table 3.3: Symbol Error Rate (SER) for M-QAM Symbols with BPSK Underlay Symbols added, where Q_i for $i \in 1, 2, 3, 4, 5$ denotes the Q-functions in Table 3.4

Underlay symbols	$U_1 = +\sqrt{E_u}$	$U_2 = -\sqrt{E_u}$
Group-1	$1-(1-Q_1)(1-Q_1)$	$1-(1-Q_1)(1-Q_1)$
Group-2	$1-(1-Q_2)(1-Q_3)$	$1-(1-Q_2)(1-Q_4)$
Group-3	$1-(1-Q_1)(1-Q_5)$	$1-(1-Q_1)(1-Q_5)$
Group-4	$1-(1-Q_5)(1-Q_3)$	$1-(1-Q_5)(1-Q_4)$

Table 3.4: Q-Functions for the Symbol Error Rate (SER) of M-QAM Symbols with Underlay BPSK added

Term	Value
Q_1	$Q\left(+\sqrt{\frac{2E_u}{\sigma_w^2}}+\sqrt{\frac{d_{min}^2}{\sigma_w^2}}\right)+Q\left(+\sqrt{\frac{2E_u}{\sigma_w^2}}+\sqrt{\frac{d_{min}^2}{\sigma_w^2}}\right)$
Q_2	$2Q\left(+\sqrt{\frac{d_{min}^2}{\sigma_w^2}}\right)$
Q_3	$Q\left(+\sqrt{\frac{2E_u}{\sigma_w^2}}+\sqrt{\frac{d_{min}^2}{\sigma_w^2}}\right)$
Q_4	$Q\left(-\sqrt{\frac{2E_u}{\sigma_w^2}}+\sqrt{\frac{d_{min}^2}{\sigma_w^2}}\right)$
Q_5	$Q\left(+\sqrt{\frac{d_{min}^2}{\sigma_w^2}}\right)$

3.4 BER of Underlay in the 5G-OFDM Underlay Architecture

Now, we derive the bit error rate expressions of the underlay symbols with BPSK and QPSK modulation schemes.

Table 3.5: Symbol Error Rate (SER) for M-QAM Symbols with QPSK Underlay Symbols added, where Q_i for $i \in 1, 2, 3$ denotes the Q-functions in Table 3.6

Underlay Symbols	$U_1 = \sqrt{\frac{E_u}{2}}(+1 + j1)$	$U_2 = \sqrt{\frac{E_u}{2}}(+1 - j1)$	$U_3 = \sqrt{\frac{E_u}{2}}(-1 - j1)$	$U_4 = \sqrt{\frac{E_u}{2}}(-1 - j1)$
Group-1	$1-(1-Q_1)(1-Q_1)$	$1-(1-Q_1)(1-Q_1)$	$1-(1-Q_1)(1-Q_1)$	$1-(1-Q_1)(1-Q_1)$
Group-2	$1-(1-Q_1)(1-Q_2)$	$1-(1-Q_1)(1-Q_3)$	$1-(1-Q_1)(1-Q_3)$	$1-(1-Q_1)(1-Q_2)$
Group-3	$1-(1-Q_1)(1-Q_3)$	$1-(1-Q_1)(1-Q_2)$	$1-(1-Q_1)(1-Q_2)$	$1-(1-Q_1)(1-Q_3)$
Group-4	$1-(1-Q_2)(1-Q_3)$	$1-(1-Q_2)(1-Q_2)$	$1-(1-Q_3)(1-Q_2)$	$1-(1-Q_3)(1-Q_3)$

Table 3.6: Q-Functions for the Symbol Error Rate (SER) of M-QAM Symbols with Underlay QPSK added

Term	Value
Q_1	$Q\left(+\sqrt{\frac{2E_u}{\sigma_w^2}}+\sqrt{\frac{d_{min}^2}{\sigma_w^2}}\right)+Q\left(+\sqrt{\frac{2E_u}{\sigma_w^2}}+\sqrt{\frac{d_{min}^2}{\sigma_w^2}}\right)$
Q_2	$Q\left(+\sqrt{\frac{2E_u}{\sigma_w^2}}+\sqrt{\frac{d_{min}^2}{\sigma_w^2}}\right)$
Q_3	$Q\left(-\sqrt{\frac{2E_u}{\sigma_w^2}}+\sqrt{\frac{d_{min}^2}{\sigma_w^2}}\right)$

3.4.1 BPSK modulation Scheme

Without interference term, i.e., $\Sigma_{i=1}^{L} c_i x_i$, SER (also BER) of Underlay symbols with equally likely symbols $u \in \{+\sqrt{E_u}, -\sqrt{E_u}\}$, in terms of Q-function is given by

$$Pr_S = BER = Q\left(\sqrt{\frac{2E_u L}{\sigma_w^2}}\right). \tag{3.13}$$

With interference term 3.3, the average SER (also BER) is given by

$$Pr_S = BER = Q\left(\sqrt{\frac{E_u}{\sigma_{m_I}^2}}\right),$$

$$Pr_S = BER = Q\left(\sqrt{\frac{2E_u L}{E_s+\sigma_w^2}}\right)$$

3.4.2 QPSK modulation Scheme

Similarly, we can derive the BER of underlay symbols with QPSK symbols $u \in \{+\sqrt{\frac{Eu}{2}}+j\sqrt{\frac{Eu}{2}}, -\sqrt{\frac{Eu}{2}}-j\sqrt{\frac{Eu}{2}}, +\sqrt{\frac{Eu}{2}}-j\sqrt{\frac{Eu}{2}}, -\sqrt{\frac{Eu}{2}}+j\sqrt{\frac{Eu}{2}}\}$, where the symbol error rate is given by

$$Pr_S = 2Q\left(\sqrt{\frac{E_u L}{E_s+\sigma_w^2}}\right) - \left(Q\left(\sqrt{\frac{E_u L}{E_s+\sigma_w^2}}\right)\right)^2$$

and the bit error rate by

$$BER = Q\left(\sqrt{\frac{E_u L}{E_s + \sigma_w^2}}\right) - \frac{1}{2}\left(Q\left(\sqrt{\frac{E_u L}{E_s + \sigma_w^2}}\right)\right)^2$$

3.5 Simulation Results

We evaluated the performance of OFDM with QPSK, 16-QAM, and 64-QAM modulations with underlay using BPSK and QPSK modulation. We compare BER plots for theoretical expressions and simulated error rates, which show good agreement for each E_s/E_u ratio. The plots are shown in Fig. 3.2. Specifically, for the 16-QAM and 64-QAM modulation schemes, the BER plots started to overlap only after reaching a certain SNR threshold of 8 dB and 12 dB, respectively. At low SNR regions, there is a mismatch between the simulated and derived expressions. This discrepancy arises from the assumption made in derived expressions that symbol errors occur only in adjacent decision regions, with a single-bit error per symbol error. However, in simulations, the presence of high noise levels at these lower SNR values caused symbols to move not only to adjacent symbol decision regions but also to the adjacent next ones, resulting in multiple-bit errors for a single symbol error.

The plot also confirms a lower E_u has the most negligible impact on OFDM performance. That is because the underlay with lower E_u won't displace the OFDM modulation symbols from their actual position on the constellation plot. Adding underlay at a specific E_u significantly degrades the performance of OFDM, particularly for higher-order modulation schemes. From the plot, we can see for a particular $E_u/E_s = 15$ dB, the deviation of the BER curve when underlay is added from without addition is higher in the case of higher-order modulation schemes. This degradation occurs because the addition of underlay symbols

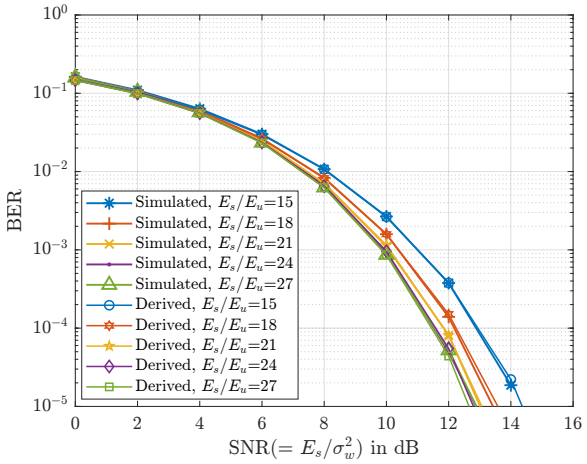

(a) OFDM: QPSK, Underlay: BPSK

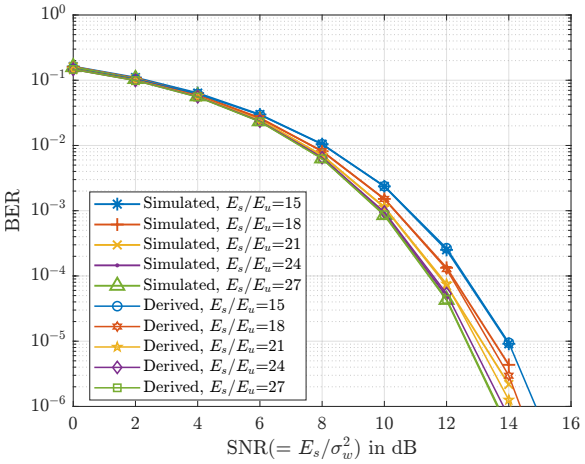

(b) OFDM: QPSK, Underlay: QPSK

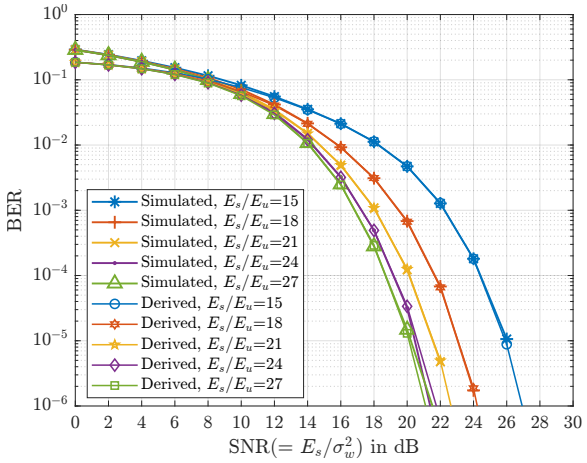

(c) OFDM: 16-QAM, Underlay: BPSK

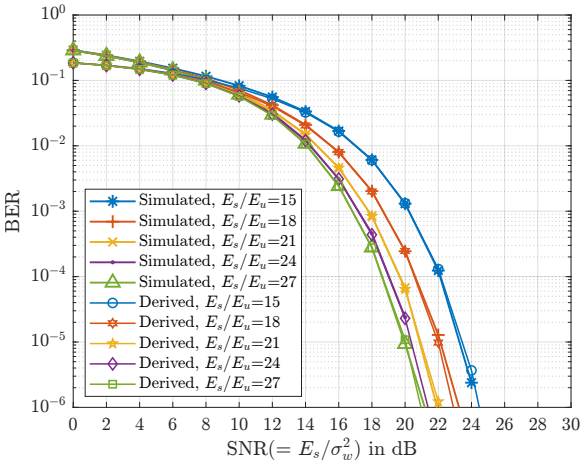

(d) OFDM: 16-QAM, Underlay: QPSK

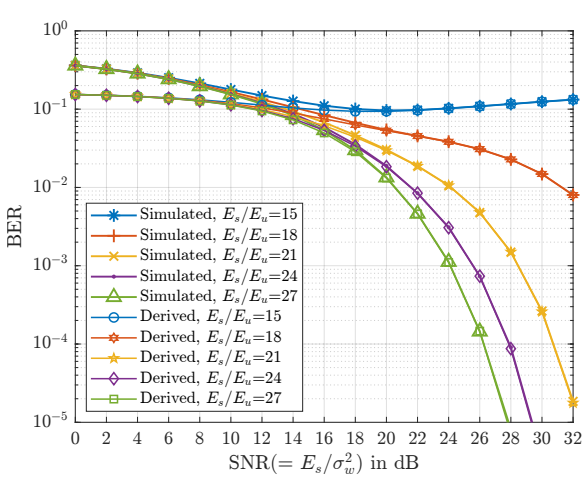

(e) OFDM: 64-QAM, Underlay: BPSK

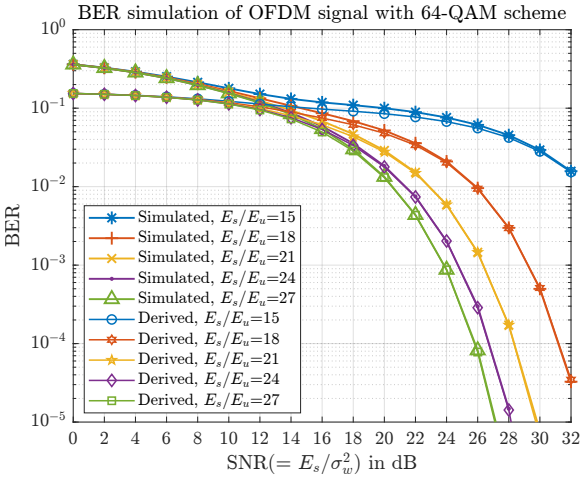

(f) OFDM: 64-QAM, Underlay: QPSK

Figure 3.2: BER comparison of derived theoretical expressions with simulations for OFDM

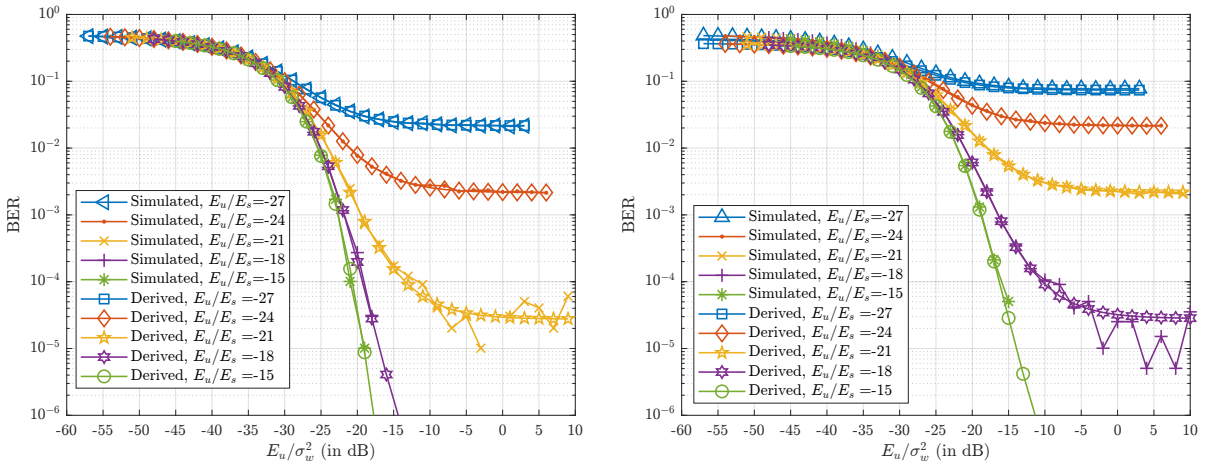

(a) BPSK modulation Scheme (b) QPSK modulation Scheme

Figure 3.3: BER Comparison of derived theoretical expressions with simulations for Underlay

pushes the OFDM modulation symbols toward their decision boundaries, causing deviation from their actual positions on the constellation plot. Since, in higher modulation schemes where symbols are closer together in the constellation plot, and the area of decision region is less, the effect of underlay addition is higher on higher modulation schemes for OFDM. For 64-QAM with BPSK modulation, the BER performance tends to rise as we increase the SNR after a certain threshold (16 dB) for particular $E_u/E_s(= 15$ dB), as shown in Fig. 3.2e. That is because when the underlay itself is strong enough to push the OFDM modulation symbols outside of their decision boundaries, additional noise can actually be helpful by occasionally moving the received signal back inside the correct decision region.

Fig. 3.3 depicts the BER performance of underlay against E_u/σ_w^2 (in dB) for BPSK and QPSK, which shows the derived expression's performance matching with the simulation for each E_u/E_s ratio. A spreading factor of 1024 is chosen. The plot also indicates that the higher the E_u/E_s, the better the performance of underlay. However, this degrades the performance of OFDM. Therefore, a higher spreading factor is required to provide the necessary SINR gain to combat interference from OFDM and noise while still operating at lower E_u.

Fig. 3.4 depicts the BER performance of underlay against E_u/σ_w^2 (in dB) for BPSK with different spreading factors keeping $E_u/E_s = -21$ dB, which shows higher spreading factors provide higher spreading gains providing better performance for underlay. Therefore, to minimally affect the OFDM's performance, a lower E_u is required, and to improve the underlay's performance, a higher spreading factor is required.

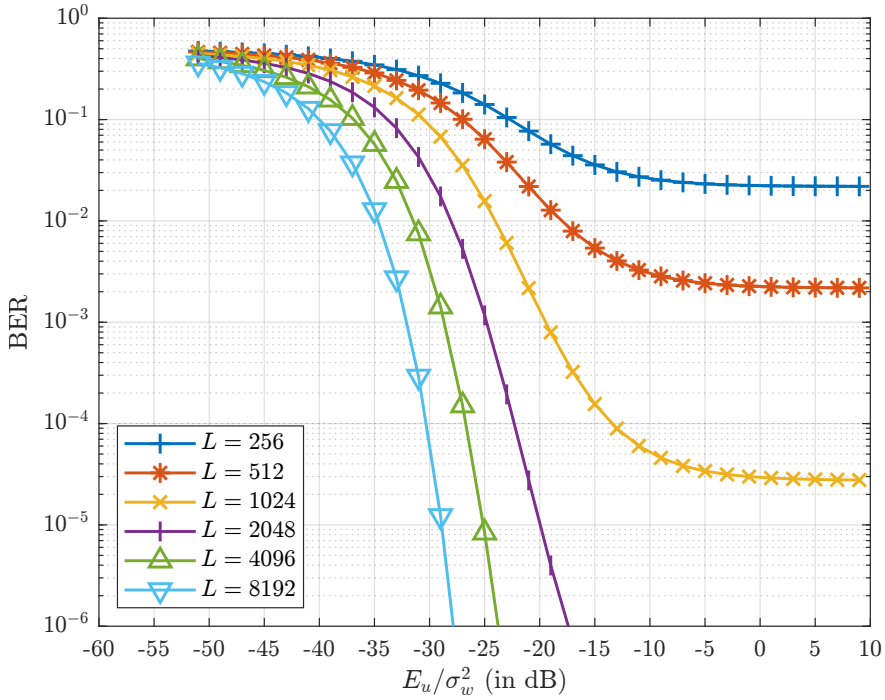

Figure 3.4: BER performance of Underlay BPSK derived theoretical expression with different spreading factors.

3.6 Conclusion

In this chapter, we derived theoretical BER expressions for OFDM in the presence of a frequency domain spread underlay. These equations allow us to analyze the BER of the OFDM and underlay signals as a function of E_s, E_u and σ_w^2. The lower the E_u, the better the performance of OFDM. However, this affects the underlay performance, which is impacted

by E_s, E_u, L, and σ_w^2. Therefore, a higher spreading factor is required to improve the performance of underlay while still operating at low E_u.

Chapter 4

Underlay Impact on 5G Throughput Performance

In this chapter, we will show the impact of underlay on the 5G Physical Downlink Shared Channel (PDSCH) throughput performance against SNR in the presence of a realistic channel model, i.e., clustered delay line (CDL) [27] with the assumption of Single-Input Single-Output (SISO) case. Here, we employ slot-level scheduling for the data transmission for the 5G and Underlay signaling.

4.1 5G PDSCH Throughput Simulator

To analyze the impact of underlay on 5G NR PDSCH throughput, we employed the link-level simulator provided by MATLAB. The PDSCH channel carries downlink data on specific time-frequency resources known as resource elements. In Fig. 4.1, the red-colored portion represents the 5G PDSCH throughput simulator, which encompasses the following key blocks:

- DL-SCH Processing: The DL-SCH serves as a transport channel utilized for transmitting user data, dedicated control information, user-specific higher-layer details, and downlink system information. Input to the DL-SCH consists of transport blocks,

while output comprises codewords directed to the PDSCH block. This process encompasses various operations including CRC attachment, Code Block segmentation, implementation of Low-Density Parity Coding (LDPC), and Rate Matching.

- PDSCH and PDSCH DM-RS signal generation: The PDSCH represents the physical channel responsible for transmitting the DL-SCH coded data. This process encompasses various operations, including Scrambling, Modulation, Layer Mapping, Precoding, and Mapping to Resource Elements. The DM-RS is a reference signal used for the estimation of the radio channel, and its allocation lies with the PDSCH symbol allocation.

- CP-OFDM modulation and demodulation, see Appendix B

- TDL and CDL propagation channel models [27]

- Perfect or practical synchronization and channel estimation: The simulation framework offers a dual set of timing synchronization and channel estimation techniques, encompassing both ideal and real-world scenarios. Within our configuration, we have opted for practical synchronization techniques. This practical approach entails timing synchronization where the correlation is performed on the received waveform with the PDSCH DM-RS to give timing offset estimate and channel estimation, which employs least squares (LS) estimation using DM-RS signal.

- PDSCH Decoding

- DL-SCH Decoding

- HARQ operation with 16 processes

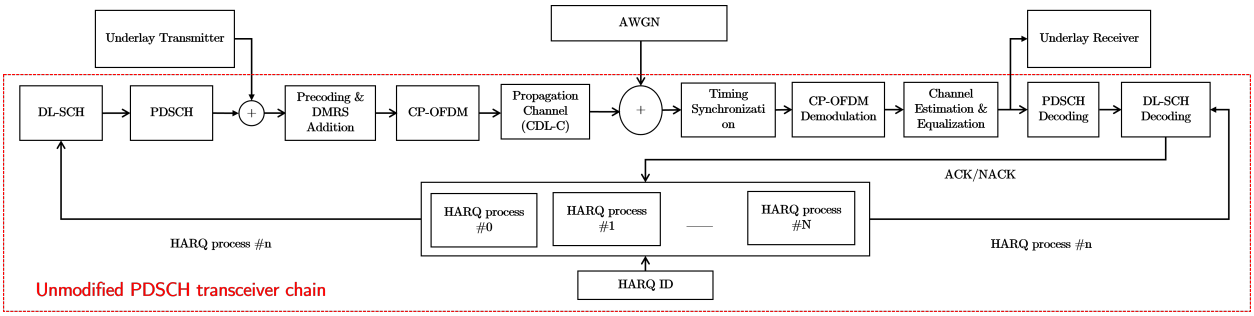

Figure 4.1: 5G PDSCH Transceiver chain with underlay signal addition and extraction.

4.2 Underlay - 5G PDSCH Throughput Simulator

The Underlay - 5G PDSCH Transceiver consists of the PDSCH transceiver with an underlay transmitter and underlay receiver. The generation of the underlay signal in this system is added with the extra functionality of channel coding, scrambling, and layer mapping, shown in Fig. 4.2. The underlay is mapped only onto subcarriers where the PDSCH data is present, not on resource elements used by 5G reference signals. This addition ensures the underlay does not interfere with the reference signals used for channel estimation/equalization and synchronization. The underlay signal is added just before the precoding and demodulation reference signal block, as shown in Fig. 4.1. This is to keep the 5G PDSCH functionality intact, i.e., beamforming at the transmitter and channel estimation and synchronization at the receiver. At the receiver, the equalized received signal, after channel estimation and equalization, is fed into the underlay receiver, which has the reverse operations of the transmitter to recover the transmitted bits.

The error correction coding (channel coding) process greatly increases the resistance to BER in raw data. A 5G standardized error coding scheme is preferred to make the underlay transmission more compatible with the 5G standard. Therefore, we investigated the error coding schemes in the 5G standard shown in Table. 4.1. The underlay transmits short packets at low data rates, like the broadcast and control channels (e.g., BCH and DCI) of

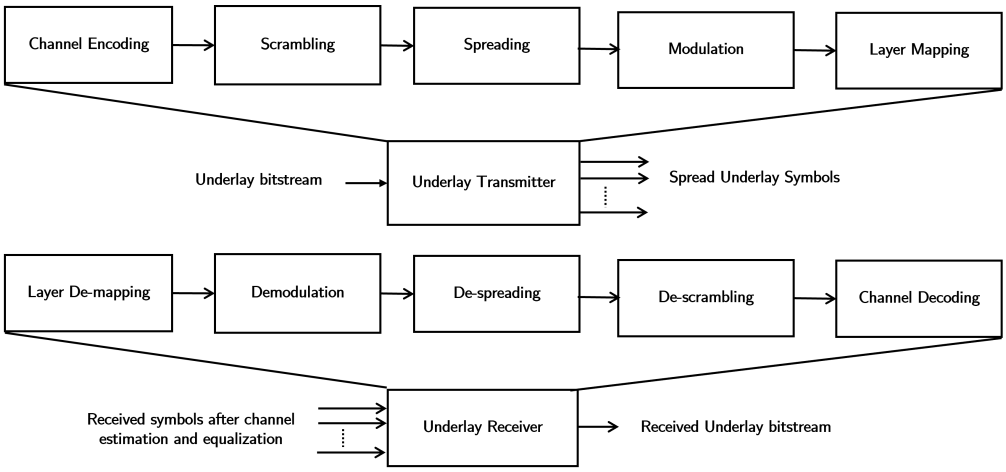

Figure 4.2: Underlay transmitter and receiver in 5G PDSCH transceiver

5G, so polar coding is chosen for the underlay.

Table 4.1: 5G NR Error Correction Coding Methods

Channel		Coding Scheme	Reference
BCH		Polar Coding	38.212 - 7.1.4
DCI		Polar Coding	38.212 - 7.3.3
UCI	12 or more bits	Polar Coding	38.212 - 6.3.1, 6.3.2
	1 bit	Repetition Code	
	2 bits	Simplex Code	
	3 to 11 bits	Reed-Muller Code	
DL-SCH		LDPC	38.212 - 7.2.4
UL-SCH		LDPC	38.212 - 6.2.4

4.3 Simulation Results

To establish a baseline for the PDSCH performance in terms of throughput ratio and throughput, we simulated the previously described 5G PDSCH channel using the parameters in Table 4.2. We measured the PDSCH performance for different modulation schemes and code rates, which are determined by the modulation coding index (IMCS) in Table 5.1.3.1-2 of the 3GPP

Technical Specification (TS) [30]. Four IMCS values are selected to cover all four modulation schemes shown in Table 4.3.

Table 4.2: PDSCH Simulation Parameters

Parameters	Value
No. Subcarriers	612
Subcarrier spacing	30 kHz
No. Layers	1
No. Codewords	1
Channel	CDL-C & AWGN
HARQ	True

We simulated 50 frames, each consisting of 20 transportation blocks, for every IMCS setting, in both the baseline PDSCH performance and underlay signal added to the PDSCH across different SNR values. Fig. 4.3 shows the results, with B indicating the baseline PDSCH performance and B+U representing the underlay signal added to the PDSCH. Fig. 4.3a illustrates the throughput ratio, which is the number of received transportation blocks without errors divided by the total number of transmitted blocks. Lower IMCS settings showed a better throughput ratio at the same SNR value than higher IMCS settings. Fig. 4.3b displays the data rate for different IMCS values. As anticipated, lower IMCS settings outperformed in low SNR conditions, while higher IMCS values were better in high SNR situations. For IMCS = 20, there is a flat line from 15 dB to 20 dB because the simulation allowed the hybrid automatic repeat request (HARQ). In that SNR range, all transportation blocks require exactly one re-transmission, resulting in a throughput ratio of 0.5.

Table 4.3: Simulated IMCS Table

IMCS	Modulation	Target Code Rate
0	QPSK	0.12
5	16QAM	0.37
11	64QAM	0.46
20	256QAM	0.67

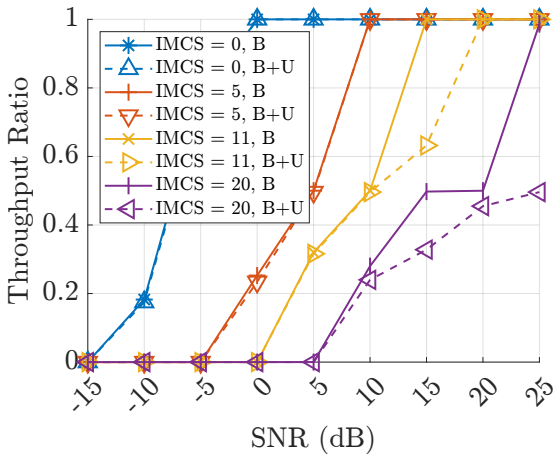

(a) Throughput ratio at SIR of 15 dB

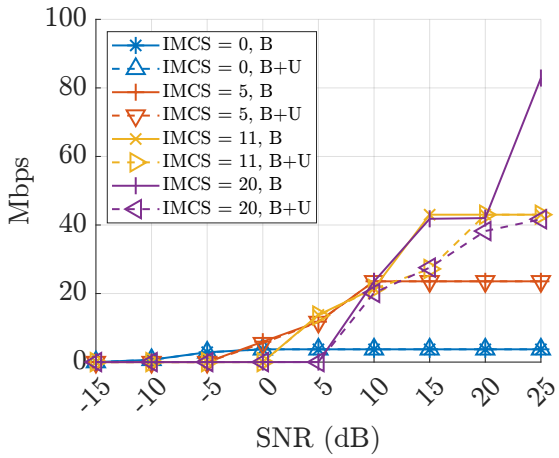

(b) Throughput in Mbps at SIR of 15 dB

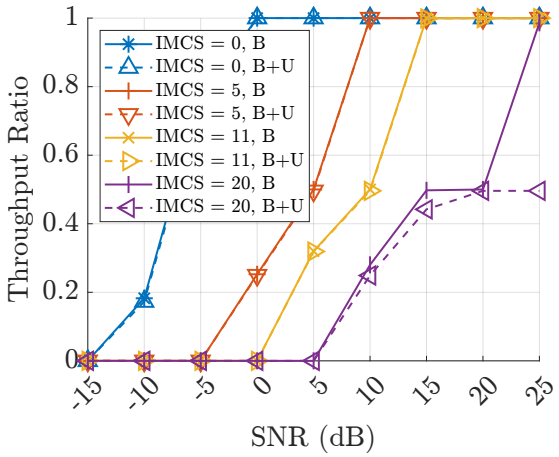

(c) Throughput ratio at SIR of 20 dB

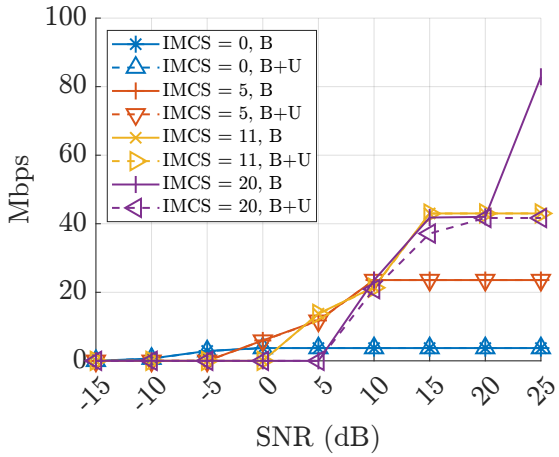

(d) Throughput in Mbps at SIR of 20 dB

Figure 4.3: 5G PDSCH Throughput Performance with Underlay against SNR (in dB) in CDL-C Channel

Next, we add the underlay signal at a level of 15 dB below the 5G PDSCH. This underlay transmission employs a QPSK modulation scheme and transmits a block of 26 bits per PDSCH slot with a Walsh spreading code of length 512. No error correction coding is applied to the underlay for these simulations. As shown in Fig. 4.3a and Fig. 4.3b, the inclusion of the underlay significantly impacts the performance of the PDSCH for higher IMCS values of 11 and 20 at high SNRs, as the PDSCH modulated symbols are close together with 64 QAM and 256 QAM. However, for lower IMCS values of 0 and 5, the impact of the underlay

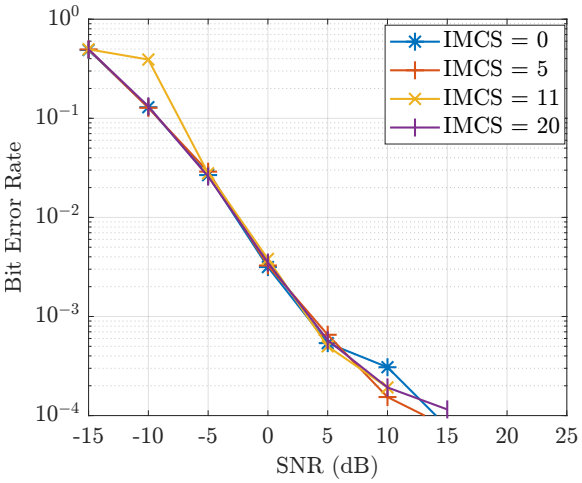

(a) BER Performance in the Presence of PDSCH for Different IMCS at SIR = 15 dB

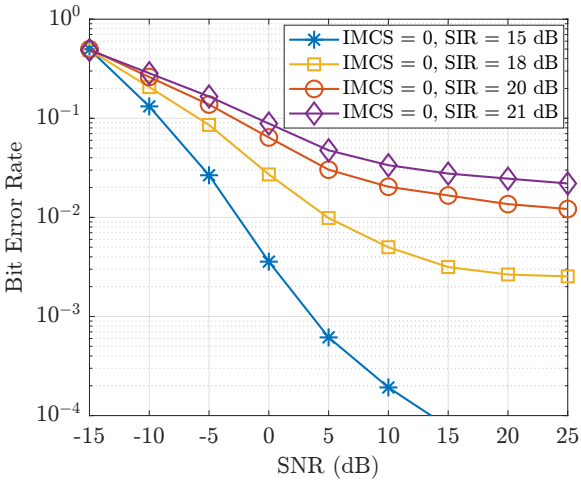

(b) BER Performance in the Presence of PDSCH at IMCS = 0 for Different SIRs

Figure 4.4: Underlay BER performance in the CDL-C channel

is negligible. Then, we investigate the impact of adding the underlay signal at a level of 20 dB below the PDSCH, as shown in Fig. 4.3c and Fig. 4.3d. This configuration leads to improved performance of the PDSCH for higher IMCS values, indicating that a lower power level for the underlay signal is preferable. However, this lower power level impacts the underlay signal's performance shown in Fig. 4.4b, suggesting the need for a higher spreading length leading to an increase in the number of resource elements (RE) occupied by spread underlay symbols. With the higher number of resources (REs) available in 5G due to the larger bandwidth configurations, it becomes easier to utilize higher spreading lengths for underlay. Fig. 4.4a depicts the underlay's performance which is similar when the interfering 5G PDSCH is modulated with different modulation schemes.

Now, we add the support of polar coding to the underlay to study the trade-off between the coding and spreading gain for the underlay signal. Here, we use e to represent the rate-matched coded bits and k to denote the number of message bits. The overall bandwidth expansion factor (spreading) is kept constant by fixing $e/k \times L = 256$. Fig. 4.5 provide insights into the reliability we can achieve from either the coding or the spreading gain.

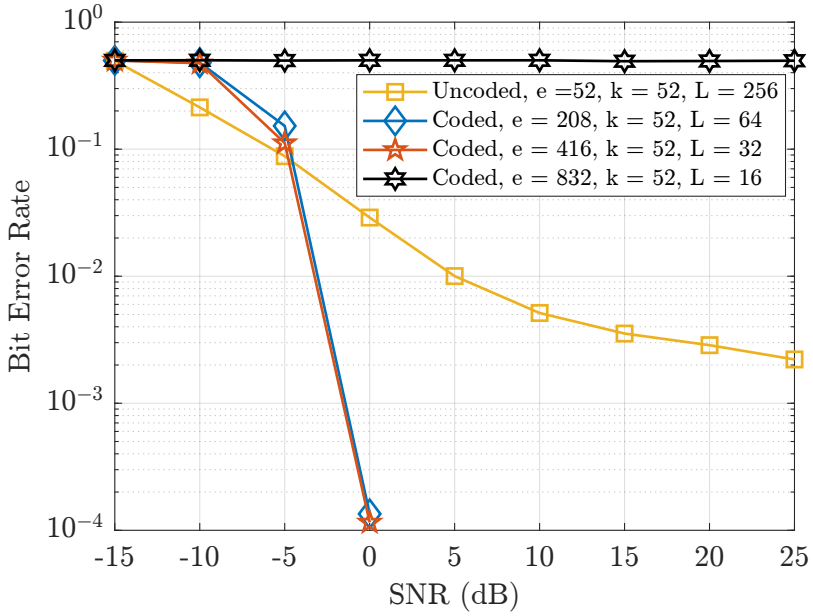

Figure 4.5: Balancing coding and spreading gain for Underlay Signal: A Trade-off Analysis in CDL-C Channel

Specifically, we maintain the same number of message bits ($k = 52$) and vary the rate-matched coded bits and spreading length. The plots reveal that combining coding with spreading resulted in significant improvements in the BER performance. However, when $e = 862$ and $L = 16$, the BER performance is worse than all the other cases, indicating the presence of a minimum spreading length needed to achieve a degree of SINR gain over the interfering 5G signal prior to decoding. We can see from Fig. 4.5 that there are no bit errors above SNR = 0 dB for coded cases with $e = 208$ or $e = 416$; thus, we achieve the full rate, i.e., 104 kbps.

Fig. 4.6 illustrates the block error rate (BLER) performance of both 5G with different IMCS values and Underlay with different spreading lengths against SIR in dB at the SNR value of 20 dB. The plot highlights that for 5G, increasing the SIR allows for higher data rates by selecting higher IMCS values as the BLER of 5G decreases. However, this approach has drawbacks for Underlay. Specifically, when considering Underlay with spreading length

$L = 256$, the BLER remains near 0 until reaching 10 dB. Similarly, for spreading length $L = 512$, the BLER remains near 0 until reaching 14 dB. Beyond these SIR thresholds, the BLER of the Underlay signaling starts to increase. It is worth noting that opting for a higher spreading length in Underlay results in lower data transmission rates but improves reliability for the Underlay.

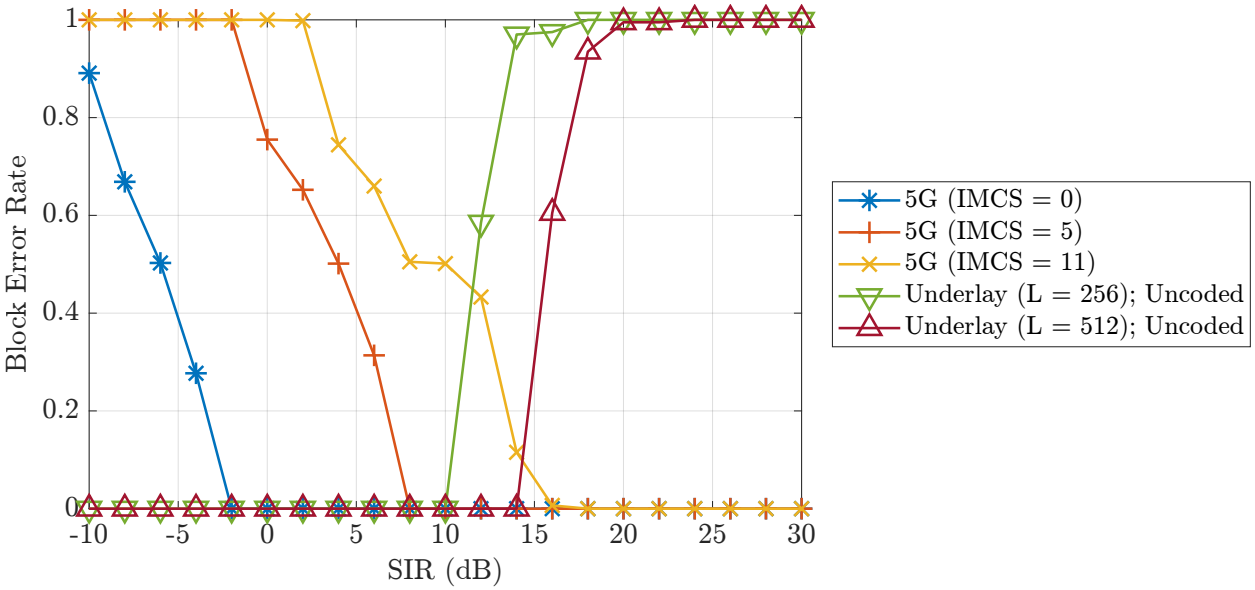

Figure 4.6: Block Error Rates for 5G with different IMCS values and uncoded Underlay using different spreading lengths in CDL-C Channel

4.4 Conclusion

The simulations presented for realistic channel conditions i.e., CDL-C channel, reveal that by selecting the appropriate SIR and associated spreading length with coding, both signals can be successfully decoded. The influence of underlay on lower IMCS values in 5G exhibits minimal impact across all SNRs. It is advisable to employ lower underlay power when higher IMCS values are utilized at high SNRs. Incorporating lower power underlay with both spreading and coding techniques significantly enhances the performance of the underlay.

Chapter 5

Proof of Concept Demonstration: Underlay-5G Co-existence

In this chapter, we describe the demonstration of the proof of concept for the Underlay and 5G NR co-existence. We considered the downlink scenario, where continuous data transmission occurs from the 5G gNodeB base station (BS) to User Equipment (UE). The underlay data is added at the physical layer (PHY) of the 5G gNodeB in a slot-synchronized manner and extracted at the PHY of the UE, shown in Fig. 5.1. Through the underlay, a low-resolution image is transmitted periodically every 1024 system frame numbers (SFN) without disrupting the ongoing 5G transmission. At the UE, the received signal comprises a combination of the 5G signal and the underlay signal. We collect this received signal and retrieve the transmitted image from it. An important point to notice is we confined the underlay processing to the PHY layer of the gNodeB. By carefully managing the underlay signaling process, we successfully demonstrated the proof of concept coexistence of underlay alongside the continuous 5G data transmission.

5.1 Demonstration Description

Our demonstration utilizes the open-source srsRAN software suite, which offers a full-stack solution for 4G and 5G networks, covering the entire spectrum from I/Q to IP. Specifi-

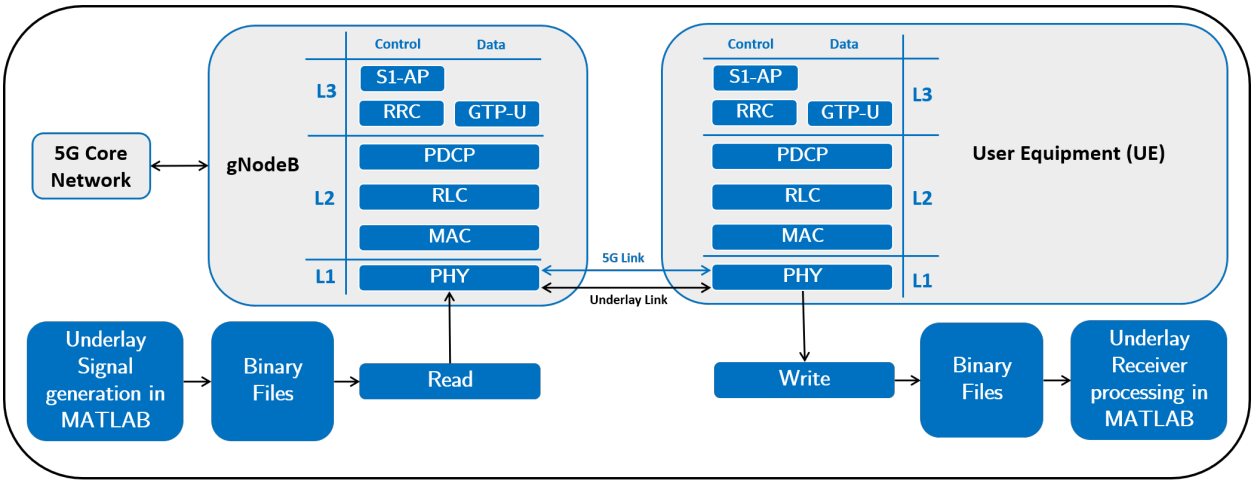

Figure 5.1: 5G Setup: Core Network, gNodeB stack, and UE stack with Underlay processing in MATLAB with its addition and extraction at the PHY layer of gNodeB and UE

cally, we leverage the 5G Standalone (SA) version (23.04) of the srsRAN 4G Project, which comprises three essential components: srsENB, srsUE, and the Core Network. The srsENB module serves as the software-based Base Station (BS) and supports 4G LTE, 5G Non-Standalone (NSA), and 5G SA. Meanwhile, the srsUE module, which fully implements the User Equipment (UE) modem in software, offers compatibility with 4G LTE, 5G NSA, and 5G SA. Within the srsRAN ecosystem, there exists its own core network, known as srsEPC, supporting 4G LTE and 5G NSA base stations. For 5G SA, Open5GS is incorporated, an open-source software implementation of the Evolved Packet Core (EPC) for 4G and the Core Network for 5G.

For the purposes of our demonstration, we employ the 5G SA versions of srsENB (gNodeB), srsUE, and Open5GS. These three integral components seamlessly collaborate to provide end-to-end 5G communication entirely through software solutions. It's worth noting that all srsRAN 4G software operates efficiently on Linux using readily available computing and radio hardware.

Within this context, we examine two types of links between the gNodeB and the UE.

1. zeroMQ link: This networking library emulates radio signals' transmission and reception over the air communication channel with controlled settings, facilitating the simulation of realistic radio scenarios for functionality testing, shown in Fig. 5.2. The controlled channel settings refer to the parameters and configurations that can be adjusted to simulate specific channel conditions for testing and evaluation purposes. The following are few of the parameters tuned for our testing of underlay:

    - **Target SNR:** The target SNR (Signal-to-Noise Ratio) defines the desired ratio between the power of the 5G signal and the power of the AWGN.
    - **Channels:** Different channel types have been included to simulate to study the performance of the srsRAN system. The following channel types are included,
        - **AWGN (Additive White Gaussian Noise):** This channel models the presence of background noise that follows a Gaussian distribution with a constant power spectral density.
        - **ETU (Extended Typical Urban):** This channel models a typical urban environment with additional delays and multipath components.
        - **EVU (Extended Vehicular Urban):** This channel models a vehicular urban environment, considering the effects of moving vehicles and their reflections on the signal.
        - **EPA (Extended Pedestrian A):** This channel models a pedestrian environment with slower fading and additional delay spread.

2. Over the Air (OTA) link: This link employs software-defined radios as the transmitting and receiving devices with antennas. The OTA link provides more practical and authentic testing, shown in Fig. 5.3.

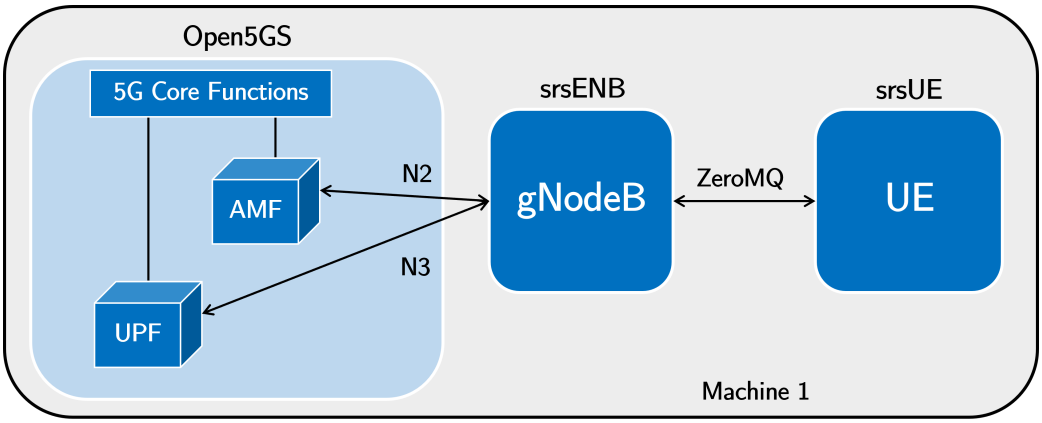

Figure 5.2: 5G SA srsRAN zeroMQ setup with one machine

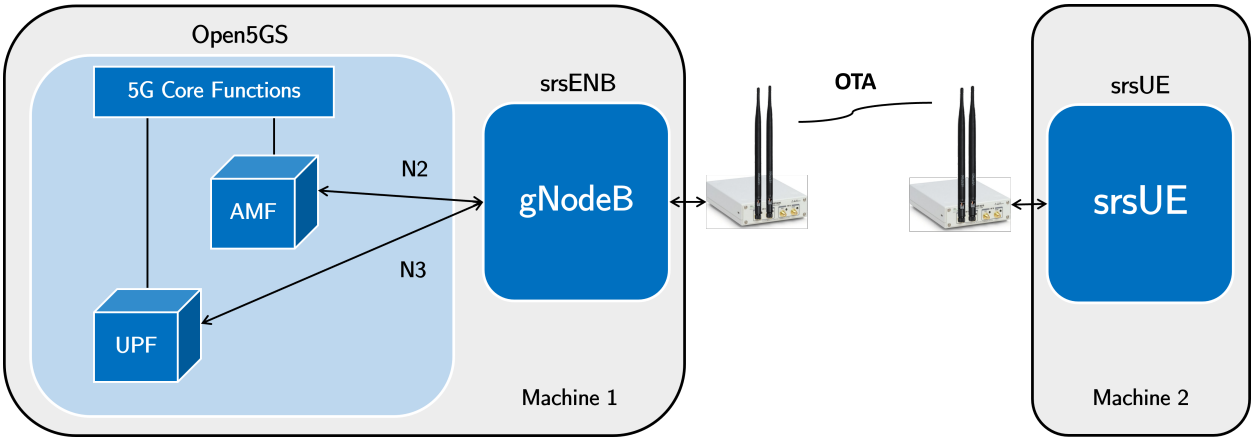

Figure 5.3: 5G SA srsRAN Over-the-Air setup with two machines

The underlay waveform is generated in MATLAB and then passed to the srsRAN gNodeB. On the receive side, the underlay waveform is extracted from srsRAN UE, and receiver processing is performed in MATLAB.

5.1.1 Underlay Processing in MATLAB at the 5G gNodeB

An image of the Virginia Tech logo shown in Fig. 5.4 is sent through underlay within a specific range of slots, i.e., $V, V+1, V+2, ..., V+N$. Here, V is the first slot number where the gNodeB sends the image through the underlay, while $N-1$ is the number of allocated

Figure 5.4: Transmitted image through underlay in 5G srsRAN

slots for image transmission. The image is converted into bits, encoded using polar coding, digitally modulated using the Quadrature Phase Shift Keying (QPSK), and then spread by the underlay spreading code. A spreading code of the desired length spreads each symbol, and the power of the spread underlay symbols is reduced to the desired level. These spread underlay symbols per slot are stored in a binary file, wherein the filename incorporates the associated slot number $(V + i)$. The processing with each block is shown in Fig. 5.5

Configurable parameters for Underlay Signal Generation

The following are configurable parameters that can be used for underlay signal generation

1. Configurable Polar Coding Parameters:
    - Values of E and K (Code Rate=$\frac{K}{E}$):
        - K = Information bits (of image) transmitted per slot
        - E = Rate-matched coded bits transmitted per slot
2. Configurable Spreading Parameters:
    - Spreading code (Walsh, M-sequence, and Zadoff-Chu)
    - Spreading length
    - SIR (Power of 5G signal with respect to Underlay) levels

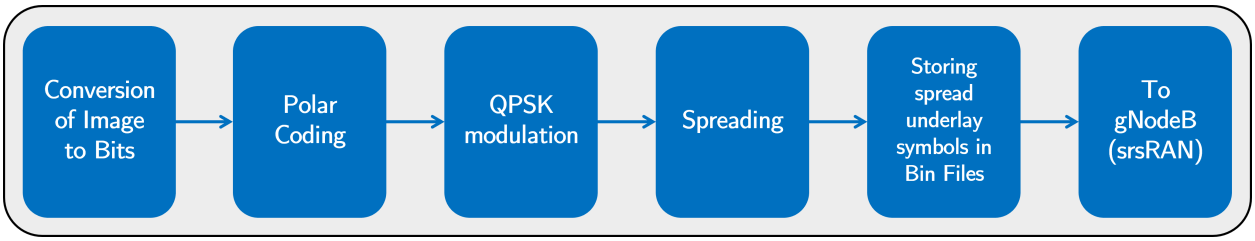

Figure 5.5: Underlay signal generation at the gNodeB machine using MATLAB

5.1.2 Underlay-5G srsRAN transceiver

Once the 5G link is established, the UE connects to gNodeB. With the iPerf tool, the throughput is simulated from the gNodeB to the UE. The gNodeB reads the corresponding spread underlay file for each slot. The spread underlay symbols are then added to the slot of the gNodeB before the IFFT (Inverse Fast Fourier Transform) operation of OFDM (Orthogonal Frequency Division Multiplexing), ensuring their integration into the overall transmission process. The UE receives the transmitted signals and writes the channel estimation and the received samples (after the FFT but prior to equalization) into binary files associated with the running slot number.

5.1.3 Underlay Processing in MATLAB at the User Equipment

The underlay receiver process at the UE reads the associated received symbols file and corresponding channel estimates. Zero-forcing equalization is then performed on received symbols to mitigate the effects of the channel. Subsequently, the despreading operation is carried out on equalized symbols, followed by demodulation and polar decoding to recover transmitted image bits. Finally, the bits are converted back into the image, completing the underlay processing at the user equipment. The processing with each block is shown in Fig. 5.6.

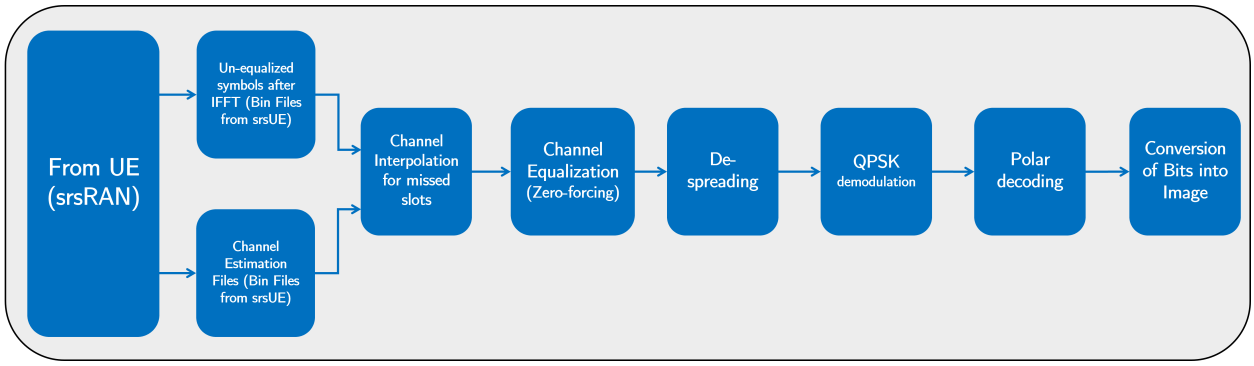

Figure 5.6: Underlay receiver processing at the UE machine using MATLAB

5.2 Experimental Results

The system is configured with a sub-carrier spacing of 15 kHz, Frequency-Division Duplex (FDD) mode, and a 10 MHz bandwidth, operating at the downlink frequency of 1.8 GHz and the uplink frequency of 1.7 GHz.

5.2.1 ZeroMQ link

Fig. 5.7 and Fig. 5.8 illustrate the image received through underlay signaling at the UE. The underlay signaling is added with extra functionality of polar coding for Fig. 5.8. The SNR is maintained at 10 dB, while the signal-to-interference ratio (SIR) is set to 15 dB and 20 dB, respectively. The received image exhibits minimal degradation, indicating the successful transmission of a low-resolution image.

Fig. 5.9 illustrates the throughput performance of 5G downlink versus SNR in rayleigh fading channel with low Doppler frequency in zeroMQ link. The underlay is transmitted continuously at 15 dB below the power of the 5G signal. The MCS values are selected from Table 5.1.3.1-1 of the 3GPP TS 38.214 [30]. The figure indicates that the maximum achievable rate of each MCS value is not reduced, although a slightly higher SNR is required

(a) ZMQ: No channel, SIR = 15 dB

(b) ZMQ: SNR = 10 dB, SIR = 15 dB

(c) ZMQ: SNR = 10 dB, SIR = 20 dB

(d) OTA: Image reception

Figure 5.7: Received image through underlay at UE via zeroMQ (a), (b), (c) and OTA (d) Links in Rayleigh Channel with low Doppler Frequency. The underlay transceiver includes only spreading.

(a) ZMQ: No channel, SIR = 15 dB

(b) ZMQ: SNR = 10 dB, SIR = 15 dB

(c) ZMQ: SNR = 10 dB, SIR = 20 dB

(d) OTA: Image reception

Figure 5.8: Received image through underlay at UE via zeroMQ (b) (c) (d) and OTA (e) link in Rayleigh channel with low Doppler frequency. The underlay transceiver includes spreading and polar coding.

for larger MCS values. For the MCS value of 27, we can see about a 1.5 dB penalty in performance.

5.2.2 OTA link

The OTA setup with two laptops (gNodeB and UE), each connected to B210 USRP with USB 3.0 cable, VERT900 antennas, and OctoClock-G, is shown in Fig. 5.10. The OctoClock-G is connected to both B210 USRPs and provides frequency and timing synchronization facilitating the provision of 10 MHz/1 PPS signals, which helps synchronize transmitting B210 and receiving B210. Fig. 5.8d depicted the image received at the UE through underlay with USRP B210s as radios, with a chosen MCS value of 9 at gNodeB and observed SNR of

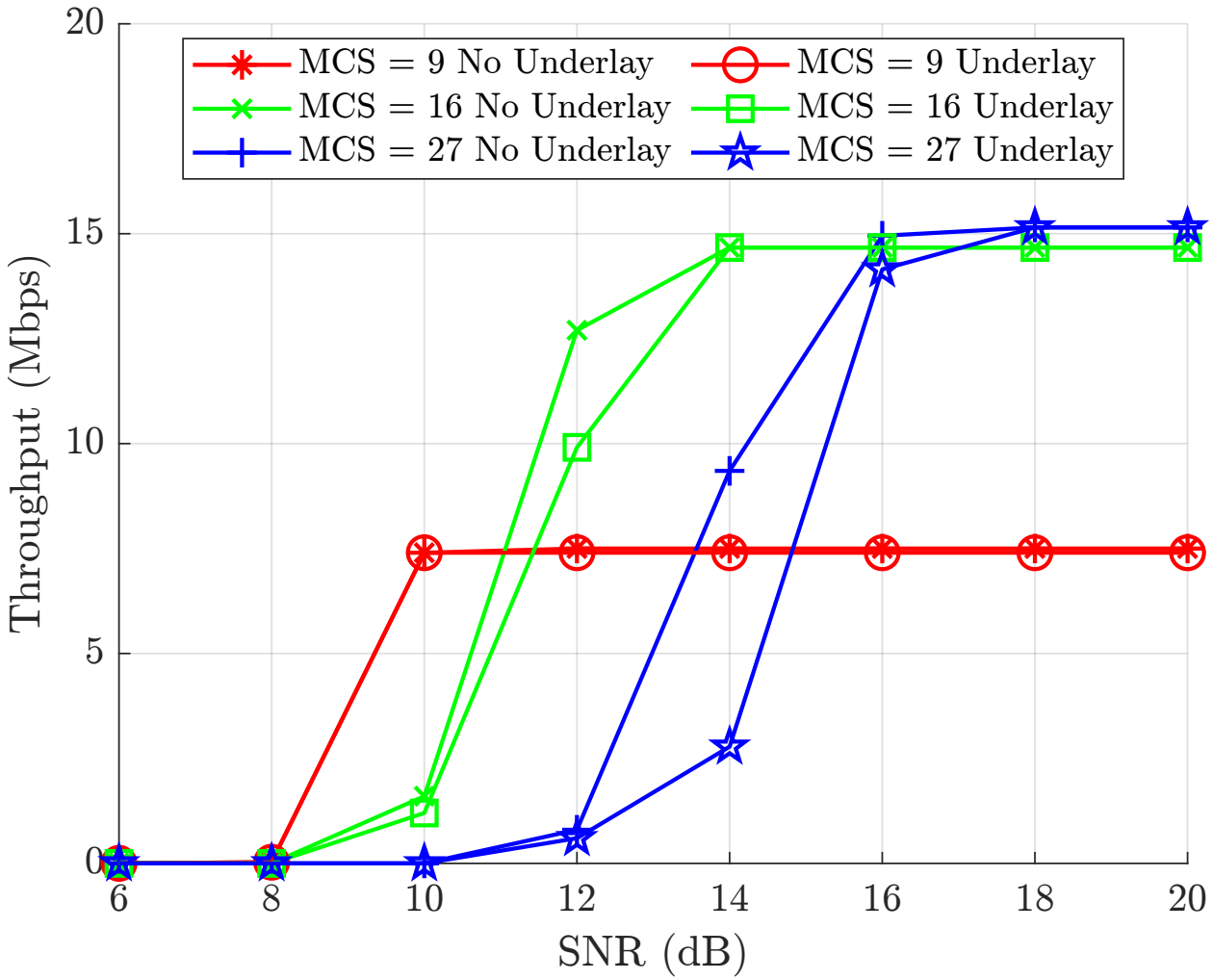

Figure 5.9: Throughput performance of 5G srsRAN downlink with zeroMQ Link

15 dB.

5.3 Conclusion

We successfully accomplished the implementation of the underlay transmission and reception in a real-time 5G setup, and the experimental results convincingly demonstrated that the transmission and reception of an underlay alongside a real-time 5G NR signal had minimal impact. The inclusion and extraction of the underlay were specifically confined to the PHY

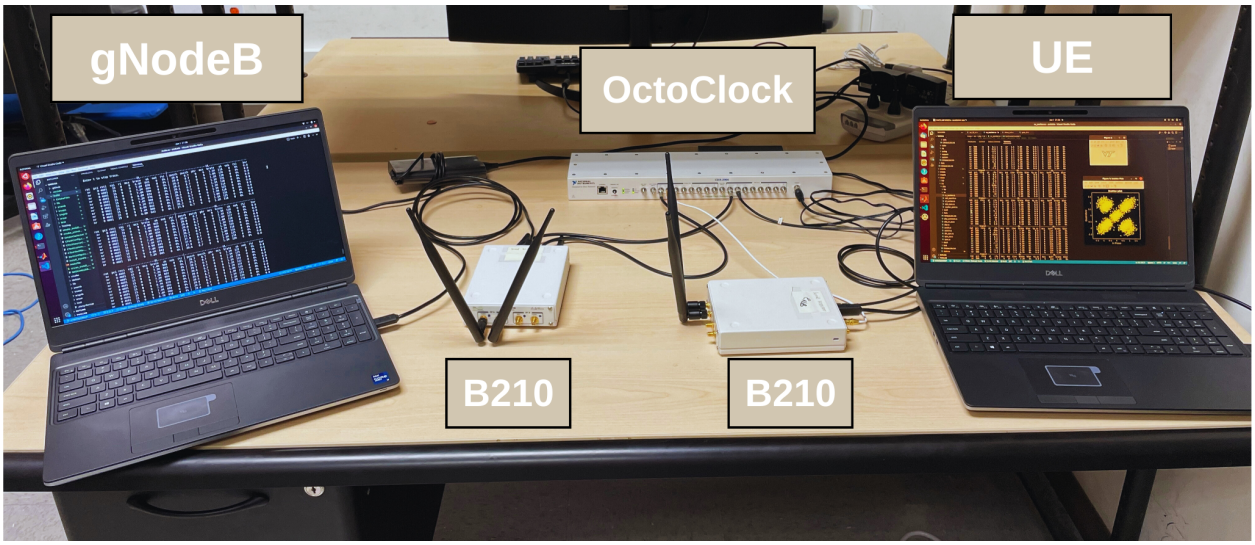

Figure 5.10: 5G SA OTA Setup with B210 Radios and OctoClock-G

layer of the srsRAN system. Consistent with our simulation findings, using lower power for the underlay had negligible effects on the 5G throughput performance. We also conclude that all reasonable complex software changes required for underlay addition and extraction in the srsRAN system are very minimal.

Chapter 6

Underlay Interference Cancellation

As we have seen in previous chapters, the underlying impact on 5G throughput performance is significant for higher-order modulation schemes. The solution was to employ very low underlay power with higher spreading lengths, which reduces the throughput in the underlay channel. The idea in this chapter is to reliably detect the underlay by using sufficient power. Once it is decoded properly, it can be used for cancellation in the 5G chain to improve 5G performance. Therefore, in this chapter, we explore the cancellation of the underlay from the 5G signal before decoding the 5G signal. This assumes that the spreading code and modulation scheme used for the underlay are known at the receiver.

To perform cancellation, the received decoded underlay bits from the underlay receiver undergo the same operations as the underlay transmitter, i.e., spreading and modulation. These generated spread underlay symbols are subtracted from the received equalized underlay-OFDM symbols (see Eq. 2.5). The process of underlay cancellation is illustrated in Fig. 6.1. Subsequently, these received equalized underlay-OFDM symbols are decoded to recover the bits that underwent OFDM modulation.

6.1 Simulation Results

The performance of underlay and OFDM modulation with underlay cancellation was simulated and plotted in Fig. 6.2 and Fig. 6.3 respectively. In this simulation, the digital

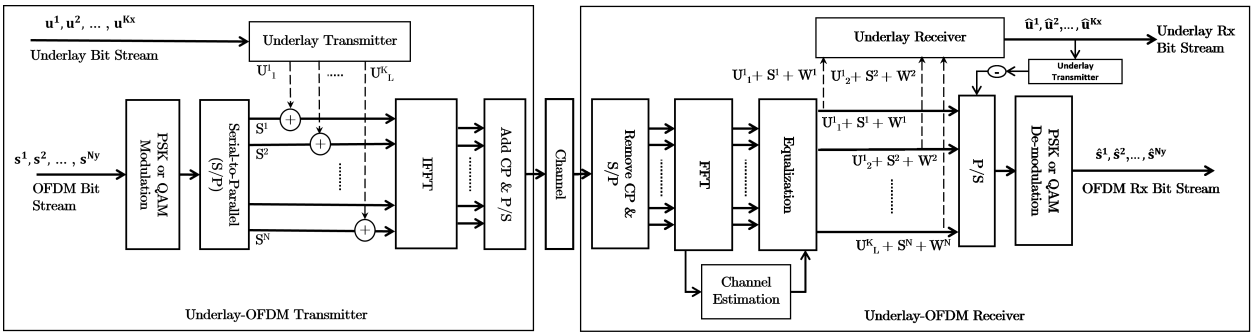

Figure 6.1: Underlay-OFDM transceiver architecture with the Underlay cancellation: The addition of underlay signal from the Underlay transmitter to sub-carriers of the OFDM chain at the transmitter, and equalized received symbols containing underlay feeding into the Underlay receiver at the receiver. The Underlay is subtracted from the OFDM receiver.

modulation schemes used in the 5G standards were employed for the OFDM modulation, while the QPSK modulation scheme was chosen for the underlay. The spreading length for underlay is 512. E_u/E_s ratios typically impact the underlay performance. It is important to note that the performance of the underlay directly affects the performance of OFDM since the underlay is canceled from the received underlay-OFDM signal. The plotted results clearly demonstrate that better performance of the underlay (i.e., $E_s/E_u = 15$ dB) leads to improved performance of OFDM, approaching the performance without underlay.

For QPSK and 16-QAM modulation schemes, the impact of underlay cancellation for various E_s/E_u is almost similar. At lower E_s/E_u ratios (indicating higher power for the underlay), the underlay is decoded with good reliability, thus generating underlay from better reliable decoded underlay bits leads to better cancellation of underlay from the underlay-OFDM signal resulting in better performance of OFDM. On the other hand, at higher E_s/E_u ratios, the underlay is transmitted at lower power, which results in poorer performance. However, due to the power of underlay being lower, the addition and cancellation of underlay have a lesser impact on the modulation symbols of OFDM, causing minimal displacement from their actual positions. In summary, a higher power underlay (lower E_s/E_u ratio) yields better

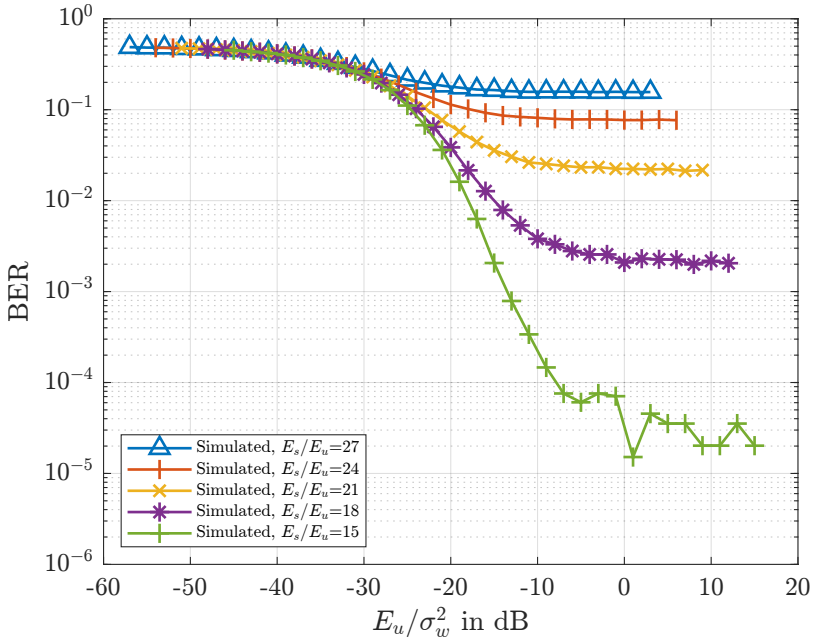

Figure 6.2: Bit Error Rate (BER) of Underlay with QPSK modulation

underlay cancellation performance due to reliable decoding, while a lower power underlay (higher E_s/E_u ratio) results in less impact on the modulation symbols of OFDM due to the cancellation process, despite the underlay's diminished performance.

For 64-QAM and 256-QAM modulation schemes, the impact of underlay cancellation for various E_s/E_u ratios shows different trends. The lower E_s/E_u ratios (i.e., 15 dB), the better the performance of OFDM, resembling the OFDM's performance without underlay. However, for some higher E_s/E_u ratios, the BER of OFDM reaches a floor level after certain SNR. This behavior can be attributed to two main factors. Firstly, the underlay is not properly decoded, and secondly, for higher modulation schemes, the modulation symbols are closely packed together. And the impact of noise being less here, the addition and cancellation of underlay displaces the OFDM modulation symbols from their actual positions largely and pushes them to adjacent symbol's decision regions. And at further higher E_s/E_u ratios, lower power of underlay results in poorer performance and poorer cancellation of underlay;

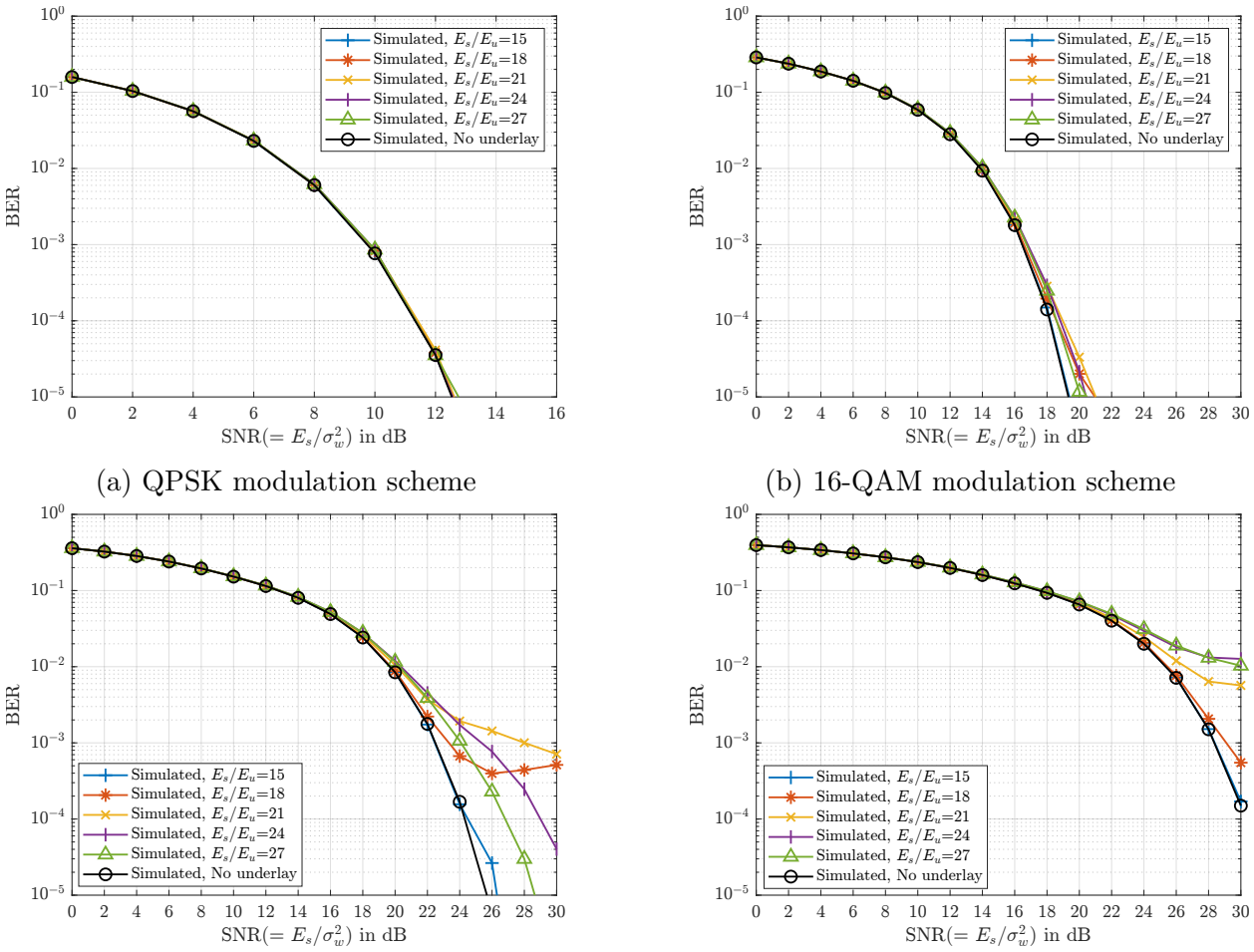

(a) QPSK modulation scheme

(b) 16-QAM modulation scheme

(c) 64-QAM modulation scheme

(d) 256-QAM modulation scheme

Figure 6.3: Bit Error Rate (BER) of OFDM with different modulation schemes and Underlay QPSK addition - Underlay cancellation at OFDM receiver

however, since the power of underlay is lower, the BER of OFDM tends to drop without flooring but does not fall in similar lines of OFDM's performance without underlay. Here, the addition and cancellation of underlay have a lesser impact on the modulation symbols of OFDM, causing less displacement from their actual positions.

Fig. 6.3 illustrates the 5G PDSCH throughput performance with underlay cancellation at the receiver. The simulation parameters for PDSCH align with those outlined in Chapter 4. Similar to previous findings, the underlay's performance directly influences the overall 5G throughput performance as it gets canceled from the received PDSCH symbols embedded with the underlay. The depicted results offer a clear visualization of the relationship between underlay performance and throughput. A more robust underlay performance, characterized by a higher E_s/E_u ratio of 15 dB, translates to improved throughput performance, closely resembling the performance achieved without underlay. And higher E_s/E_u of 20 dB (due to lower underlay power) also has a lesser impact on the throughput performance of 5G, having similar performance without underlay. However, for 256-QAM, the performance slightly degrades due to their symbols being closer together.

6.2 Conclusion

The simulated results conclude that in order to cancel underlay at the receiver, the underlay should be decoded reliably in order to improve the performance of 5G. The results also suggest that lower power underlay has a lesser impact on the performance of 5G. However, the cancellation is less effective due to degraded performance in detecting the underlay prior to cancellation.

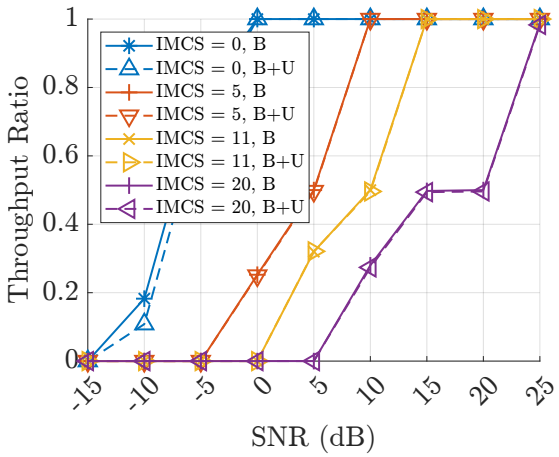

(a) Throughput ratio at $E_s/E_u = 15$ dB

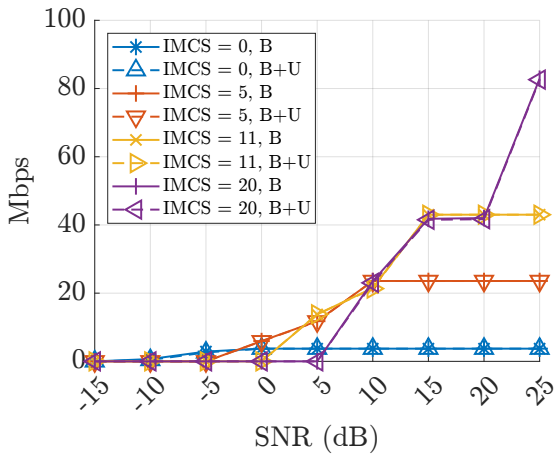

(b) Throughput in Mbps at $E_s/E_u = 15$ dB

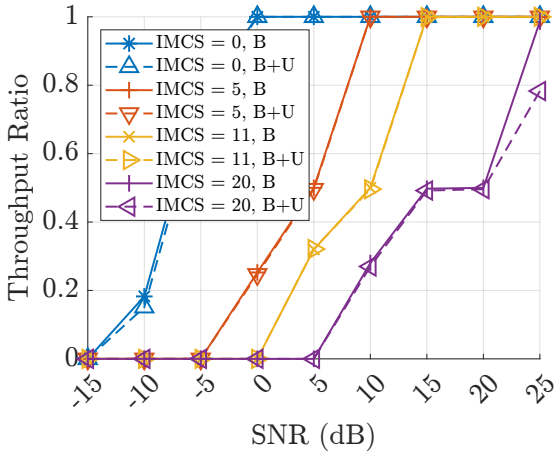

(c) Throughput ratio at $E_s/E_u = 20$ dB

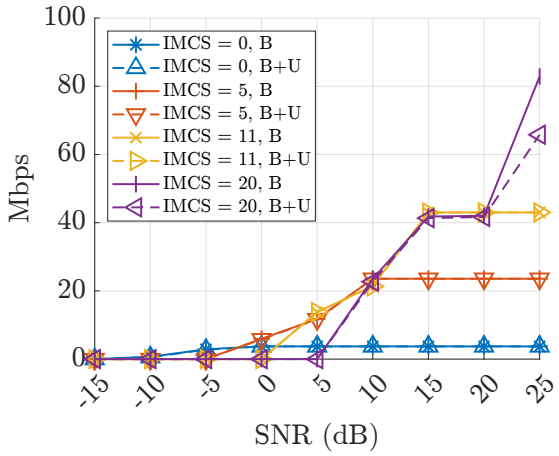

(d) Throughput in Mbps at $E_s/E_u = 20$ dB

Figure 6.4: 5G PDSCH Throughput Performance with Underlay against SNR (in dB) in CDL-C Channel - Underlay cancellation at receiver

Chapter 7

Conclusion

Our comprehensive performance evaluation and theoretical analysis, complemented by extensive simulations and practical demonstrations, strongly support the use of the underlay as an auxiliary channel alongside continuous 5G transmission. We can reliably detect and decode the underlay signal by carefully selecting the appropriate design parameters, such as the signal-to-interference power level (5G power in relation to the underlay), spreading factor, and channel coding, with zero to minimal impact on 5G performance. The performance of 5G is primarily influenced by the signal-to-interference (SIR) power level, whereas the underlay's performance depends on both the signal-to-interference power level and the spreading factor. The analytical bit error rate expressions confirm this. These expressions allow us to analyze the bit error rate of the OFDM and underlay signals as functions of E_s, E_u, and σ_w^2, where E_s is the average energy of modulation symbols undergoing OFDM modulation, and E_u is the average energy of spread underlay symbols. The σ_w^2 is the AWGN noise power. The lower the E_u, the better the performance of OFDM. However, this affects the underlay performance, which is impacted by E_s, E_u, L, and σ_w^2. Therefore, a higher spreading factor is required to improve the performance of the underlay while still operating at low E_u.

Decreasing the underlay power level reduces the impact of the underlay on 5G performance, while the underlay's performance suffers unless compensated by higher spreading and coding gains. There is a trade-off between the gains achieved from spreading and coding, as indicated

by simulation results. Adding channel coding to the underlay enhances its performance. For a fixed bandwidth expansion factor, the best performance of the underlay is achieved when spreading and coding are combined. Moreover, the performance of different spreading codes in the underlay remains equivalent as long as they possess similar spreading lengths. The PAPR analysis shows that if the spreading code chosen is a Walsh code, then the code index should be chosen with minimal periodicity but, overall, not much impact.

Our practical demonstration successfully showcased the simultaneous transmission and reception of an underlay alongside a real-time 5G signal. To achieve this, we utilized the open-source srsRAN software suite, which offers a complete software implementation of the 5G network. The integration and extraction of the underlay were specifically limited to the PHY layer of the srsRAN system. Aligned with our simulation results, we observed that employing lower power for the underlay had a minimal impact on 5G throughput performance. We also observed that the changes required for underlay addition and extraction in the srsRAN system are minimal, which leads to the conclusion that the changes required to add support for underlay in actual 5G systems and UE chipsets are minimal.

Underlay, as an auxiliary channel to the 5G NR signal, offers numerous potential benefits to 5G. The underlay is constructed on the basis of frequency-domain spread spectrum technology, providing it with Low Probability of Intercept (LPI) and Low Probability of Detection (LPD) characteristics. This means that the data transmitted on underlay is more difficult to detect and decode than ever, thereby enhancing the security and making it ideal for sensitive applications. The non-preemptive nature of the underlay ensures that critical information is always transmitted without interruption. Whether it's crucial control data or low-data rate Ultra-Reliable Low Latency Communication (URLLC), the underlay can be configured for ultra-reliability through proper choice of power level, spreading factor, and error correction coding. The underlay's low data rate capabilities make it perfect for secure Internet of Things

(IoT) applications. It's not just about connecting devices, it's also about doing so with the utmost security and resiliency. The underlay isn't just confined to civilian use cases. Its features make it a perfect fit for tactical IoT and military communications. With minimal adjustments, it seamlessly integrates these critical functions onto the 5G network. Importantly, the underlay added on top of OFDM in 5G doesn't affect the Peak-to-Average Power Ratio (PAPR) of the transceiver, ensuring the stability and resiliency of 5G communications.

7.1 Future Directions

The research conducted in this thesis has primarily focused on the design, analysis, and demonstration of the co-existence of underlay-5G signaling. Future work in this field will encompass a deeper understanding of the underlay's characteristics, specifically in terms of LPI and LPD, and how these attributes can be leveraged to enhance the resilience and robustness of 5G networks against adversarial activities such as jamming, sniffing, and spoofing.

Furthermore, our research motivation is driven by practical applications, including secure Internet of Things (IoT) deployments and the achievement of low-data, error-free Ultra-Reliable Low Latency Communications (URLLC). In our ongoing efforts, we aim to implement these applications within our framework and assess the improvements they bring to the table.

Bibliography

[1] A. Goldsmith, S. A. Jafar, I. Maric, and S. Srinivasa, "Breaking Spectrum Gridlock With Cognitive Radios: An Information Theoretic Perspective," *Proc. of the IEEE*, vol. 97, no. 5, pp. 894–914, 2009.

[2] J. Lee, H. Wang, J. G. Andrews, and D. Hong, "Outage Probability of Cognitive Relay Networks with Interference Constraints," *IEEE Trans. Wireless Commun.*, vol. 10, no. 2, pp. 390–395, 2011.

[3] L. Luo, P. Zhang, G. Zhang, and J. Qin, "Outage Performance for Cognitive Relay Networks with Underlay Spectrum Sharing," *IEEE Commun. Lett.*, vol. 15, no. 7, pp. 710–712, 2011.

[4] L. Lv, J. Chen, Q. Ni, Z. Ding, and H. Jiang, "Cognitive Non-Orthogonal Multiple Access with Cooperative Relaying: A New Wireless Frontier for 5G Spectrum Sharing," *IEEE Commun. Mag.*, vol. 56, no. 4, pp. 188–195, 2018.

[5] K. Doppler, M. Rinne, C. Wijting, C. B. Ribeiro, and K. Hugl, "Device-to-device communication as an underlay to LTE-advanced networks," *IEEE Commun. Mag.*, vol. 47, no. 12, pp. 42–49, 2009.

[6] K. Doppler, M. P. Rinne, P. Janis, C. Ribeiro, and K. Hugl, "Device-to-Device Communications; Functional Prospects for LTE-Advanced Networks," in *Proc. IEEE Int. Conf. Commun. Workshops*, 2009, pp. 1–6.

[7] J. Liu, Y. Kawamoto, H. Nishiyama, N. Kato, and N. Kadowaki, "Device-to-device com-

munications achieve efficient load balancing in LTE-advanced networks," *IEEE Wireless Commun.*, vol. 21, no. 2, pp. 57–65, 2014.

[8] Z. Liu, T. Peng, S. Xiang, and W. Wang, "Mode selection for Device-to-Device (D2D) communication under LTE-Advanced networks," in *Proc. IEEE Int. Conf. Commun. (ICC)*, 2012, pp. 5563–5567.

[9] H. Zhang, Y. Liao, and L. Song, "D2D-U: Device-to-Device Communications in Unlicensed Bands for 5G System," *IEEE Trans. Wireless Commun.*, vol. 16, no. 6, pp. 3507–3519, 2017.

[10] L. Wei, R. Q. Hu, Y. Qian, and G. Wu, "Enable device-to-device communications underlaying cellular networks: challenges and research aspects," *IEEE Commun. Mag.*, vol. 52, no. 6, pp. 90–96, 2014.

[11] GSMA, *Future Networks*. [Online]. Available: https://www.gsma.com/futurenetworks/ip_services/understanding-5g/

[12] M. Lichtman, R. P. Jover, M. Labib, R. Rao, V. Marojevic, and J. H. Reed, "LTE/LTE-A jamming, spoofing, and sniffing: threat assessment and mitigation," *IEEE Commun. Mag.*, vol. 54, no. 4, pp. 54–61, 2016.

[13] M. Lichtman, R. Rao, V. Marojevic, J. Reed, and R. P. Jover, "5G NR Jamming, Spoofing, and Sniffing: Threat Assessment and Mitigation," in *Proc. IEEE Int. Conf. Commun. Workshops (ICC Workshops)*, 2018, pp. 1–6.

[14] [Online]. Available: https://www.defense.gov/News/Releases/Release/Article/2960806/dod-establishes-5g-and-future-generation-wireless-cross-functional-team/

[15] 3GPP, "Study on New Radio (NR) access technology," 3rd Generation Partnership Project, Technical Report (TR) 38.912, 04 2022, version 17.0.0.

[16] H. Wang, J. Wang, G. Ding, L. Wang, T. A. Tsiftsis, and P. K. Sharma, "Resource Allocation for Energy Harvesting-Powered D2D Communication Underlaying UAV-Assisted Networks," *IEEE Trans. on Green Commun. and Netw.*, vol. 2, no. 1, pp. 14–24, 2018.

[17] Z. Zhou, M. Dong, K. Ota, G. Wang, and L. T. Yang, "Energy-Efficient Resource Allocation for D2D Communications Underlaying Cloud-RAN-Based LTE-A Networks," *IEEE Internet of Things J.*, vol. 3, no. 3, pp. 428–438, 2016.

[18] M. Hasan, E. Hossain, and D. I. Kim, "Resource Allocation Under Channel Uncertainties for Relay-Aided Device-to-Device Communication Underlaying LTE-A Cellular Networks," *IEEE Trans. Wireless Commun.*, vol. 13, no. 4, pp. 2322–2338, 2014.

[19] M. Belleschi, G. Fodor, and A. Abrardo, "Performance analysis of a distributed resource allocation scheme for D2D communications," in *IEEE GLOBECOM Workshops (GC Wkshps)*, 2011, pp. 358–362.

[20] M. Zulhasnine, C. Huang, and A. Srinivasan, "Efficient resource allocation for device-to-device communication underlaying LTE network," in *IEEE 6th Int. Conf. on Wireless and Mobile Comput., Netw. and Commun.*, 2010, pp. 368–375.

[21] F. Wang, C. Xu, L. Song, and Z. Han, "Energy-Efficient Resource Allocation for Device-to-Device Underlay Communication," *IEEE Trans. Wireless Commun.*, vol. 14, no. 4, pp. 2082–2092, 2015.

[22] C. Xu, L. Song, Z. Han, Q. Zhao, X. Wang, X. Cheng, and B. Jiao, "Efficiency Resource Allocation for Device-to-Device Underlay Communication Systems: A Reverse Iterative Combinatorial Auction Based Approach," *IEEE J. on Selected Areas in Commun.*, vol. 31, no. 9, pp. 348–358, 2013.

[23] G. Fodor, S. Parkvall, S. Sorrentino, P. Wallentin, Q. Lu, and N. Brahmi, "Device-to-Device Communications for National Security and Public Safety," *IEEE Access*, vol. 2, pp. 1510–1520, 2014.

[24] K. Ali, H. X. Nguyen, Q.-T. Vien, P. Shah, and Z. Chu, "Disaster Management Using D2D Communication With Power Transfer and Clustering Techniques," *IEEE Access*, vol. 6, pp. 14 643–14 654, 2018.

[25] H. Moradi and B. Farhang-Boroujeny, "Underlay Scheduling Request for Ultra-Reliable Low-Latency Communications," in *IEEE 2nd 5G World Forum (5GWF)*, 2019, pp. 28–33.

[26] A. Aminjavaheri, A. RezazadehReyhani, R. Khalona, H. Moradi, and B. Farhang-Boroujeny, "Underlay Control Signaling for Ultra-Reliable Low-Latency IoT Communications," in *Proc. IEEE Int. Conf. Commun. Workshops (ICC Workshops)*, 2018, pp. 1–6.

[27] 3GPP, "Study on channel model for frequencies from 0.5 to 100 GHz," 3rd Generation Partnership Project, Technical Specifications (TS) 38.901, 03 2022, version 17.0.0.

[28] 3GPP, "5G; NR; Physical channels and modulation," 3rd Generation Partnership Project, Technical Specifications (TS) 38.214, 01 2023, version 17.4.0.

[29] V. Chakravarthy, X. Li, Z. Wu, M. A. Temple, F. Garber, R. Kannan, and A. Vasilakos, "Novel overlay/underlay cognitive radio waveforms using SD-SMSE framework to enhance spectrum efficiency- part i: theoretical framework and analysis in AWGN channel," *IEEE Trans. Commun.*, vol. 57, no. 12, pp. 3794–3804, 2009.

[30] 3GPP, "Physical layer procedures for data," 3rd Generation Partnership Project, Technical Specifications (TS) 38.214, 09 2022, version 17.3.0.

Appendices

Appendix A

Multiple Access Techniques

Multiple Access techniques describe how multiple users transmit data while sharing the same communication resource, forming the heart of the cellular system. They are characterized into:

- Frequency Division Multiple Access (FDMA): The available bandwidth is divided into non-overlapping sub-channels, allocating each sub-channel to a different user.
- Time Division Multiple Access (TDMA): The available bandwidth is shared by multiple users; however, the users transmit and receive their data in their assigned time slots.
- Code Division Multiple Access (CDMA): The available frequency-time resources are shared by users, each user allocated with a different spreading code which helps to mitigate interference from other users and maintain orthogonality.
- Orthogonal Frequency Division Multiple Access (OFDMA): The available frequency-time resources, which are orthogonal, are allocated to multiple users to transmit and receive data.
- Space Division Multiple Access (SDMA): It is based on creating parallel spatial pipes using advanced MIMO antenna techniques where multiple users use these pipes to transmit and receive data simultaneously.

In each access technique, the idea is to multiplex multiple users' data orthogonally, ensuring

that the user can reliably retrieve its intended data. These access schemes were used in the previous cellular systems, and currently, the 5G system uses OFDMA, which is built on Orthogonal Frequency Division Multiplexing (OFDM).

Non-orthogonal multiple Access (NOMA) is one of the upcoming multiple access techniques proposed recently to serve multiple users using the same wireless resource, i.e., time-slot in TDMA or frequency band in FDMA or space in SDMA and spreading code in CDMA. One of the common ways to realize NOMA is the power domain, where high power is allocated to users with worse channel conditions and low power is allocated to users with good channel conditions.

Appendix B

Orthogonal Frequency Division Multiplexing

Orthogonal Frequency Division Multiplexing (OFDM) is a multi-carrier modulation technique combating the frequency selective fading channel which induces Inter-symbol interference (ISI). Due to the presence of many objects and movement between the transmitter and receiver, the transmitted signal undergoes multiple reflections, scattering and diffraction, and these reflected (multi-path) signals arrive at the receiver with different delays. These multi-path signals combine at the receiver forming a linear time-varying channel impulse response. The coherence bandwidth represents the frequency range within which the channel's frequency response remains statistically the same or exhibits the same fading.

If the channel's coherence bandwidth is larger than the signal bandwidth, each frequency component of the signal experiences the same fading (having the same delay in the time domain), resulting in flat fading. The transmitted signal is not distorted, and power fluctuates at times with its amplitude following the Rayleigh distribution. However, if the channel's coherence bandwidth is smaller than the signal bandwidth, each frequency component of the signal experiences different fading (having a different delay in the time domain), causing ISI, which distorts the transmitted signal. The higher data rate applications with larger bandwidth than the coherence bandwidth tend to experience frequency selective fading, degrading the application's performance. The idea behind the OFDM modulation is to con-

vert the higher data rate signal (single-carrier) experiencing frequency selective fading into a larger number of parallel lower data rate signals (multiple sub-carriers), with each sub-carrier experiencing flat fading. That increases the symbol time making it more robust to ISI. However, due to channel delay effects, ISI still exists, which is combated by introducing guard time, which nullifies ISI and by filling up with an end portion of transmitted OFDM signal in the guard time, which nullifies Inter-Carrier Interference (ICI). Fig. B.1 illustrated

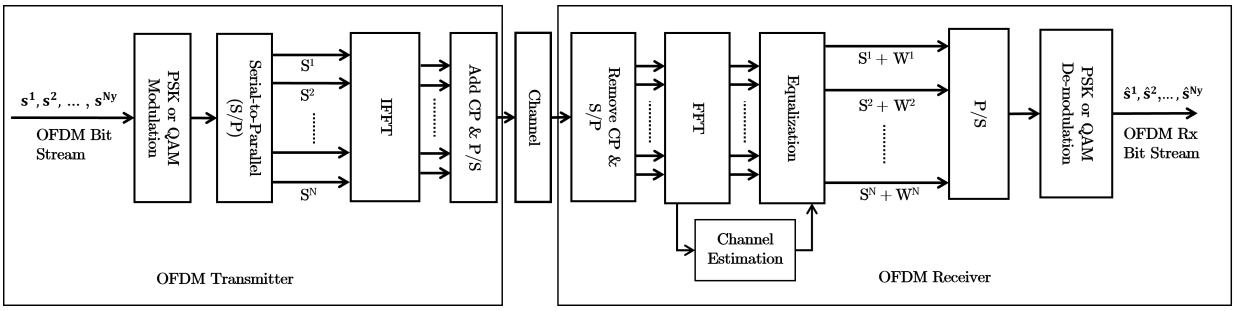

Figure B.1: OFDM transceiver in AWGN channel with $H^i = 1$

the OFDM transceiver chain. At the transmitter, a block of $N \times y$ bits undergo linear digital modulation, serial-to-parallel conversion, Inverse Fast Fourier transform (IFFT), the addition of Cyclic Prefix (CP) and parallel-to-serial conversion. The output of the IFFT block is given by:

$$X^n = \Sigma_{i=1}^{N} S^i e^{j2\pi(i-1)(n-1)/N} \tag{B.1}$$

Here, X^n represents the output of the IFFT block, S^i represents the symbol at the i-th subcarrier, n is the time index, and N is the total number of subcarriers.

The received OFDM signal can be written as:

$$r^n = \sum_{l=0}^{L-1} h^{(n,l)} X^{n-l} + w^n \tag{B.2}$$

In this equation, r^n represents the received signal at time index n, L is the number of multi-

path, $h^{(n,l)}$ denotes the time-varying channel taps for each path, and at each time index, X^n is the transmitted signal, and w^n represents the additive white Gaussian noise. At the receiver, after the FFT process, the received signal can be written as:

$$Y^i = H^i S^i + W^i \tag{B.3}$$

where H^i is the Fourier transform of the channel impulse response $h^{(n,l)}$.

Appendix C

Spread Spectrum

Spread spectrum is a modulation technique that increases the signal's bandwidth (lowering its power spectral density) by a spreading code that is pseudo-random in nature and independent of the signal transmitted. At the transmitter, the signal bandwidth is expanded by a spreading code which is called spreading. At the receiver, the received signal is converted back to its original transmitted signal by correlating with spreading code which is called despreading. Spreading the signal have benefits in terms of resilience to intended or untended interference, the ability to hide the signal in the noise floor, combating the multi-path fading, multiple access and localization.

Spreading codes used in the spread spectrum are categorized into two types:

1. Pseudo-random sequences with good auto-correlation properties. These properties make the signal difficult to find by an interceptor while relatively easy to find by the desired receiver.

    - M-sequences
    - Gold codes
    - Kasami codes

2. Orthogonal codes with good cross-correlation properties. These properties enable multiple access as the primary application (multiplexing multiple data streams on the same

signal)

- Walsh codes

Walsh Spreading

The Walsch-Hadamard codes form the backbone of CDMA systems. These codes are generated from the Hadamard matrix, which is a square matrix of order n given by the recursive formula:

$$H_n = \begin{pmatrix} H_{n-1} & H_{n-1} \\ H_{n-1} & -H_{n-1} \end{pmatrix} \text{ and } H_0 = [1]$$

Each row of the Hadamard matrix, except the first one, corresponds to a Walsh code that has an equal number of plus ones and minus ones. The length of codes is confined to a power of 2. The orthogonality between these codes makes them suitable for multiplexing multiple users in the underlay channel.

M-sequence

M-sequences are generated by a k-length linear feedback shift register and are considered pseudo-random sequences. They have a maximum length of $2^k - 1$. While they exhibit low auto-correlation, their cross-correlation properties are typically poor.

Zadoff-Chu sequence

These sequences, also known as constant amplitude zero auto-correlation (CAZAC) sequences, are complex sequences with a unit magnitude with good auto-correlation and cross-

correlation properties. The sequence is given by:

$$\mathrm{X}(m+1) = \exp\left(-\frac{j\pi rm(m+1)}{N}\right), \text{ for } m = 0, \ldots, N-1.$$

where r is the root of the Zadoff-Chu sequence.